

Interhemispheric Comparisons of Large Nighttime Magnetic Perturbation Events Relevant to GICs

Mark J. Engebretson¹, Kathryn R. Kirkevold¹, Erik S. Steinmetz¹, Viacheslav A. Pilipenko^{1,2},
Mark B. Moldwin³, Brett A. McCuen³, C. R. Clauer⁴, Michael D. Hartinger^{4,5}, Shane Coyle⁴,
Hermann Opgenoorth⁶, Audrey Schillings⁶, Anna N. Willer⁷, Thom R. Edwards⁷, David H.
Boteler⁸, Andy J. Gerrard⁹, Mervyn P. Freeman¹⁰, and Michael C. Rose¹⁰

¹ Augsburg University, Minneapolis, MN

² Institute of Physics of the Earth, Moscow, Russia

³ University of Michigan, Ann Arbor, MI

⁴ Virginia Tech, Blacksburg, VA

⁵ Space Science Institute, Boulder, CO

⁶ Umeå University, Umeå, Sweden

⁷ DTU Space, Kgs. Lyngby, Denmark

⁸ Natural Resources Canada, Ottawa, ON, Canada

⁹ New Jersey Institute of Technology, Newark, NJ

¹⁰ British Antarctic Survey, Cambridge, UK

to be submitted to the Journal of Geophysical Research – Space Physics

date of this version: April 20, 2020

Key Words: geomagnetically-induced currents, magnetic perturbation events, substorms, magnetic storms, magnetic conjugacy, omega bands

Key Points:

Conjugate pre-midnight MPEs were largest in dB_x/dt and were often but not always simultaneous to within 3 min over ~ 100 -700 km in latitude.

Conjugate post-midnight MPEs were associated with omega bands, largest in dB_y/dt , highly localized, and independent in time over ~ 1.5 h.

Perturbation amplitudes and maximum derivatives favored a current generator model over a voltage generator model for near-solstice events.

Abstract

Nearly all studies of impulsive magnetic perturbation events (MPEs) with large magnetic field variability (dB/dt) that can produce dangerous geomagnetically-induced currents (GICs) have used data from the northern hemisphere. Here we present details of four large-amplitude MPE events ($|\Delta B_x| > 900$ nT and $|dB/dt| > 10$ nT/s in at least one component) observed between 2015 and 2018 in conjugate high latitude regions ($65 - 80^\circ$ corrected geomagnetic latitude), using magnetometer data from (1) Pagnirtung and Iqaluit in eastern Arctic Canada and the magnetically conjugate South Pole Station in Antarctica and (2) the Greenland West Coast Chain and two magnetically conjugate chains in Antarctica, AAL-PIP and BAS LPM. From 1 to 3 different isolated MPEs localized in corrected geomagnetic latitude were observed during 3 pre-midnight events; many were simultaneous within 3 min in both hemispheres. Their conjugate latitudinal amplitude profiles, however, matched qualitatively at best. During an extended post-midnight interval, which we associate with an interval of omega bands, multiple highly localized MPEs occurred independently in time at each station in both hemispheres. These nighttime MPEs occurred under a wide range of geomagnetic conditions, but common to each was a negative IMF B_z that exhibited at least a modest increase at or near the time of the event. A comparison of perturbation amplitudes to modeled ionospheric conductivities in conjugate hemispheres clearly favored a current generator model over a voltage generator model for 3 of

the 4 events; neither model provided a good fit for the pre-midnight event that occurred near vernal equinox.

1. Introduction

The study of Earth's space environment has in recent years become increasingly recognized as having significant practical importance as well as academic interest because of the damaging impacts that disturbances in the magnetosphere and ionosphere can impose on technological infrastructure. Extreme geomagnetically-induced currents (GICs) can disrupt the operation of large-scale ground-based electrically conducting systems such as electrical power grids, pipelines, telecommunication cables, and railway systems (Ngwira and Pulkkinen, 2019). Given this practical emphasis, it is not surprising that nearly all studies of the high latitude magnetic and electrical perturbations that can generate (GICs) have been based on data from the northern hemisphere. It is becoming increasingly clear that the chain of physical processes in the near-Earth magnetosphere and ionosphere that can generate GICs is complex (Viljanen, 1997; Henderson et al., 1998; Apatenkov et al., 2004; Ngwira et al., 2015, 2018; Kozyreva et al., 2018; and Dimmock et al., 2019) and that these events may be causally related to active conditions in the magnetotail such as bursty bulk flows and/or dipolarizing flux bundles (Angelopoulos et al., 1992; Sergeev et al., 1999; Kauristie et al., 2000; Zesta et al., 2000, 2006; Lyons et al., 2012; Gabrielse et al., 2014; Liu et al., 2014; and Engebretson et al., 2019b) that are expected to impact high latitude regions in both the northern and southern hemispheres.

Although the technological risk from GICs is greater during magnetic storms, when the auroral oval expands to subauroral latitudes, impulsive magnetic perturbation events (MPEs) with duration ~ 5 to 15 min have also been found to more often occur during non-storm times (Viljanen et al., 2006) and at up to at least 78° magnetic latitude (Engebretson et al., 2019a). A recent case study of three large amplitude MPEs observed using an extensive two-dimensional set of ground magnetometer arrays in Arctic Canada, Western Greenland, and Antarctica (Engebretson et al., 2019b) showed that these events appeared roughly simultaneously at near-magnetically-conjugate locations (at the northern and southern ends of the same magnetic field lines) in each hemisphere. In this study we present multi-station data from a large two-dimensional set of ground-based magnetometers in the northern hemisphere and magnetometers at magnetically conjugate locations in Antarctica, both covering a range in corrected

geomagnetic (CGM) latitude from $\sim 65^\circ$ to over 80° . By detailing the similarities and differences between large MPEs in both hemispheres we provide additional information that may be helpful for understanding the physical mechanisms involved in their generation.

2. Data Set and Event Identification Technique

Vector magnetometer data used in this study were recorded by the MACCS (Engebretson et al., 1995) and CANMOS (Nikitina et al., 2016) arrays in Arctic Canada, the Greenland West Coast chain (<https://www.space.dtu.dk/MagneticGroundStations>), the conjugate AAL-PIP chain in Antarctica (Clauer et al., 2014), the British Antarctic Survey (BAS) Low Power Magnetometer chain (Kadokura et al., 2008), and the fluxgate magnetometer at South Pole Station, Antarctica (Lanzerotti et al., 1990; Engebretson et al., 1997). Data are presented in local magnetic coordinates. In the northern hemisphere (at MACCS, CANMOS and Greenland West Coastal chain stations) and in the southern hemisphere (at AAL-PIP and BAS LPM stations) the sensor axes are oriented as follows: X: magnetic north, Y: magnetic east, and Z: vertically down. The South Pole magnetometer sensors are X: magnetic north, Y: magnetic east, and Z: vertically upward (a left-handed system). The sampling rate of MACCS data is 2 Hz, and for the other stations 1 Hz.

Figure 1 and Table 1 show that South Pole Station in Antarctica is in approximate magnetic conjugacy to MACCS station Pangnirtung and CANMOS station Iqaluit in Canada. Figure 1 also shows that the six AAL-PIP stations in Antarctica, located about 20° farther east in corrected geomagnetic (CGM) longitude, are in close magnetic conjugacy to the middle of the Greenland West Coast chain, and that the BAS LPM chain is conjugate in CGM magnetic latitude to several of the lower latitude Greenland West Coast stations, but approximately midway in CGM longitude between the Canadian and Greenland stations (Table 1).

The semi-automated procedure used to identify and quantify MPEs in these data sets is detailed in Engebretson et al. (2019a), and a summary is presented here. Routinely produced daily magnetograms (24-hour plots of magnetic fields in local geomagnetic coordinates) were displayed on a computer screen. Once a large-amplitude 5-10 minute duration magnetic perturbation was visually identified, the IDL cursor function was used to select times before and after a region of interest containing the MPE. The times and values of extrema in this interval were recorded for each component, and after application of a 10-point smoothing to reduce noise

and eliminate isolated bad data points, the data were numerically differentiated. Plots of the time series of data and derivatives were produced and saved, and the maximum and minimum derivative values were automatically determined and recorded.

3. Event Studies

In this section we present four intervals of large-amplitude MPEs that were observed at both northern and southern high latitudes. In each case we also show OMNI interplanetary magnetic field (IMF) and solar wind data, time-shifted to the nose of the magnetosphere, as well as the SYM/H index and the SuperMAG SML and SMU indices (Newell and Gjerloev, 2011) of magnetic activity. The first three intervals occurred in the pre-midnight sector under conditions ranging from geomagnetically quiet to storm time. The fourth interval occurred in the post-midnight sector during the main and early recovery phases of a more intense magnetic storm.

For all three pre-midnight MPE intervals studied here, the largest $|dB/dt|$ values occurred during a sharp initial pulse which set up the MPE. In contrast, within the post-midnight interval sharp (but less intense) pulses were seen at different times at each site over a span of ~ 1.5 hours. Their multiple rapid variations resembled those of Pi 3 or Ps 6 pulsations (Opengoorth et al., 1983; Solov'yev et al., 1999; Apatenkov et al., 2020) rather than solitary impulses. Figure 2, a full-day magnetogram AAL-PIP PG4 on May 13, 2015, shows good examples of both pre- and post-midnight events. The post-midnight interval, to be discussed in detail in section 3.4 below, extended from 05:30 to 08:00 UT and was characterized by a long-lasting ~ 800 nT negative bay in the Bx (north-south) component and three large ~ 20 minute period pulsations of 200 nT amplitude in the Bx and By (east-west) components. The pre-midnight interval on this day was dominated by a single > 800 nT southward (negative) impulse in the Bx component near 23:00 UT. Large $|dB/dt|$ values occurred during both events. The maximum derivatives during the pre-midnight interval were -14.5 nT/s (dBx/dt), 9.4 nT/s (dBy/dt), and 16.5 nT/s (dBz/dt). During the post-midnight event they were -5.2 nT/s (dBx/dt), 5.2 nT/s (dBy/dt), and -6.1 nT/s (dBz/dt).

3.1 Interval 1: 15 January 2018 00:24 – 00:51 UT YRDAY 18015

Figure 3a shows IMF and solar wind parameters from the OMNI database as well as the SuperMAG SML and SMU indices and the SYM/H index, from 2200 UT January 14, 2018 to

0200 UT January 15, 2018. Figures 3b and 3c show 3-component magnetic field data from AAL-PIP PG3 in Antarctica and Qeqertarsuaq (GDH) in Greenland. These stations were in close magnetic conjugacy, separated by 0.6° in CGM Lat and 1.1° in CGM Lon (Table 1 and Figure 1). The shaded region, from 00:24 to 00:51 UT January 15, spans the large magnetic perturbation observed at both stations. Substorm onsets included in the SuperMAG substorm list for 2018 occurred at 23:32 UT January 14 at 67.8° MLAT and 1.33 h MLT and 00:22 UT January 15 at 66.86° MLAT and 1.77 MLT). The times of these onsets, marked in Figure 3a by red arrows, were ~ 1 hour and ~ 2 minutes, respectively, before the beginning of the MPE interval, and they occurred ~ 4 -5 h MLT distant from the MLTs of the arrays of stations analyzed for this event (Figure 4).

Before the onset of the MPE, the IMF magnitude increased slightly and the IMF Bz component was slightly negative but increasing toward 0. Both the IMF Bx and By components were near -4 nT (not shown), so the IMF had the most typical “garden-hose” orientation. The solar wind velocity (V_{sw}) and dynamic pressure (P_{sw}) were modest and relatively steady. The SML index decreased rapidly from -62 to -324 nT at the time of the first substorm onset, decreased rapidly again from -139 to -883 nT beginning near the time of the second substorm onset, and increased toward -500 nT near the end of the MPE interval. The SYM/H index decreased slightly before MPE onset to -14 nT and also remained near this level during the MPE.

As shown in Figures 3b and 3c, the Bx components at both GDH and PG3 reached their minimum value at 00:35 UT, 13 min after the most recent substorm onset. Perturbations in By and Bz had opposite signs at the two stations, and as was the case for each of the 4 events shown, also showed less similarity in shape than the Bx perturbations. The relative orientations of the Bx and By perturbations most likely reflect the hemispheric difference in the circular Hall current flow around a localized field-aligned current (FAC), counter-clockwise in the northern hemisphere and clockwise in the southern hemisphere. Also shown in these figures are the magnitude of the maximum derivative in each component. Both the perturbations (ΔB) and derivative amplitudes $|dB/dt|$ in each component were slightly larger in the northern hemisphere.

Figure 4 shows Bx (north-south) component data from several stations during this event, organized by increasing local time (left to right) and decreasing magnetic latitude (top to bottom). Panel a) shows data from the near-conjugate South Pole and Pangnirtung station pair, panel b) shows data from AAL-PIP stations PG2, PG3, and PG5 and BAS LPM stations M79

and M78 in Antarctica, and panel c) shows data from West Greenland stations UMQ, GDH, STF, GHB, FHB, and NAQ. The same vertical and horizontal ranges are used in each panel. At each station, the time of maximum $|\Delta B_x|$ perturbations is shown.

There was good agreement in the timing of Bx minima near 00:35 UT between northern and southern hemisphere stations with $|\text{MLAT}| \geq 73.9^\circ$ in both local time sectors: PGG, UMQ, and GDH in Canada and Greenland, and SP, PG2, and PG3 in Antarctica, with amplitudes larger in the northern (winter) hemisphere. Two minima in Bx occurred at three intermediate latitude stations (STF, PG5, and GHB) between 00:20 and 01:00 UT, with no simultaneity between stations, and none showed evidence of the minimum at 00:35 UT that was observed at more poleward stations. One maximum in Bx occurred at the four lowest latitude stations (FHB, M79, NAQ, and M78). The largest derivative was in the X component at 8 stations, in the Z component at 4 stations, and in the Y component at none.

The ΔB_x polarity reversal between 69.3° and 66.6° MLAT suggests the presence of an ionospheric flow shear, with westward flow poleward and eastward equatorward of it. The positive perturbation observed at the lower latitudes may represent the equivalent return current of the westward current in the negative ΔB_x spike observed at higher latitudes. It is possible that the negative spike at 00:21 UT observed at PG5 was caused by a westward traveling surge that moved westward and poleward to appear successively later at more poleward stations: at 00:26 UT at STF, at 00:33 UT at Pagnirtung, and between 00:35 and 00:39 at PG3, PG2, GDH, and UMQ. This would be qualitatively consistent with the progressive appearance of MPEs at more westward and poleward stations found in three recent case studies of MPEs by Engebretson et al. (2019b) using a two-dimensional array of stations in Arctic Canada.

Figure 5a shows the north-south perturbation amplitudes (ΔB_x) and Figure 5b shows the maximum derivative amplitude in any component observed at every available station during this event in the West Greenland Coastal Array (red triangles) and the conjugate AAL-PIP and BAS LPM arrays (black asterisks). Discussion of Figure 5c is deferred until section 4. In the MLAT range from $\sim 70^\circ$ to $\sim 76^\circ$, corresponding to a distance of ~ 700 km in both hemispheres, the amplitudes of both the perturbations and derivatives were larger in the northern hemisphere. However, the latitude profiles for ΔB_x and maximum dB/dt in Greenland did not follow each other closely in the region of largest amplitudes. In both hemispheres the equatorward falloff of amplitude with MLAT was more gradual than its poleward counterpart.

The second column of Table 2 shows the maximum $|dB/dt|$ values for each component for each of the stations shown in Figure 4. At the West Greenland stations and their conjugate arrays the maximum derivatives were larger in the northern hemisphere. However, the MLT dependence was complex: Figure 4a shows that farther west, the ΔB_x value at SPA was smaller than that at PGG, but Table 2 indicates its peak derivative value was larger than that of any other station in the data set. During this interval the largest derivative was in the X component at 8 stations, in the Z component at 4 stations, and in the Y component at none.

3.2 Interval 2: 16 March 2016 00:34-00:57 UT YRDAY 16076

This complex MPE interval, which had significant amplitude over an MLAT range of at least 10° , occurred during the early recovery phase of a weak magnetic storm, as shown in Figure 6a. The SYM/H index decreased modestly from -30 to -50 nT between 22:00 and 24:00 UT on March 15, and showed a slight < 5 nT increase before the interval and a similar small decrease during the interval. The IMF magnitude remained steady near 8 nT for ~ 2 h before and during the highlighted interval and again the IMF B_z component was negative (-4 nT) but increased shortly before and during the interval. Both the IMF B_x and B_y components were near 0 nT (not shown). V_{sw} and P_{sw} were again relatively constant before and during the interval. A substorm onset occurred at 23:51 UT March 15, at 70.98° MLAT and 8.37 h MLT. The time of this onset, shown in Figure 6a, was 40 minutes before the beginning of the MPE interval, and it occurred more than 10 h MLT away from the magnetometer stations shown in Figure 7.

A broad minimum in SML and maximum in SMU were evident during this MPE interval, after which time both indices gradually returned to more quiet levels. The SML index dropped gradually from ~ -284 nT at onset to a minimum of -742 nT at 00:18 UT, and at 00:43 UT exhibited a short ~ -200 nT negative spike, near the time of the large amplitude spikes shown in Figure 6b and c.

Three-component magnetic field data from PG4 and STF (Figures 6b and 6c) show similar B_x waveforms with minima simultaneous to within 1 min, again oppositely directed perturbations in B_y , and complex variations in B_z . In all three components the amplitudes of both the perturbations and derivatives were larger in the southern hemisphere.

This interval also showed latitude-dependent variations in timing that were very similar in both hemispheres (Figure 7). A B_x minimum occurred simultaneously to within 1 min at

00:48 UT at the four most poleward stations in both hemispheres ((SP, PG2, PG3, and GDH, all above 73.9° |MLAT|), but occurred earlier (at 00:42 UT) at the two Canadian stations (PGG, IQA). In the |MLAT| range from 69.8° to 71.9° a Bx minimum occurred nearly simultaneously at 00:37 UT at Antarctic stations PG4, M85 (not shown), PG5, and M84 (not shown), and at STF in Greenland, and Bx minima appeared at SKT and GHB in Greenland 1-3 minutes later. A more temporally extended substorm bay in Bx rather than a single dominant but short-lived negative perturbation was observed at the four lower latitude stations (M81, M79, FHB, and NAQ). Rapid negative excursions in Bx were evident at each of these four stations and at GHB, during the downward slope of the bay between 00:35 and 00:37 UT, but were in each case (except at M79) relatively small. It is possible that the 00:35-00:37 UT disturbance that first appeared at these lower latitude stations expanded poleward and westward to appear later at higher latitude stations, as in interval 1.

Figure 8 shows latitudinal profiles of the ΔB_x perturbation amplitude (panel a) and the maximum derivative amplitude (panel b), as in Figure 5. At all latitudes both quantities were consistently larger in the southern hemisphere, and the latitudinal profiles were similar, with one major exception: the derivative amplitude at M84, located 10° magnetic longitude west of PG5 and other AAL-PIP stations, was substantially larger (25.7 nT/s) than the amplitude at PG5 (16.2 nT/s). Figure 7a shows that the ΔB_x value at SP in Antarctica was also larger than at the Arctic stations PGG and IQA.

The third column of Table 2 shows the maximum $|dB/dt|$ values for each component for each of the stations shown in Figure 7. During this interval the derivatives were consistently larger at all stations in the southern hemisphere than at northern hemisphere stations at comparable latitudes and local times. The largest derivative was in the X component at 11 stations, in the Z component at 2 stations, and in the Y component at one (SPA). Derivative magnitudes were nearly equal in X and Z at 2 stations.

3.3 Interval 3: 8 May 2016 21:02-21:30 UT YRDAY 16129

This MPE interval, which occurred shortly before the second minimum of a double-minimum geomagnetic storm (minimum SYM/H ~ -87 nT, Figure 9a), included an extremely large dB/dt value of 37.7 nT/s at BAS LPM M79, but appeared only within an |MLAT| range of $\sim 5^\circ$, from 64° to 69° . During and before this interval the IMF magnitude was relatively steady

near 8 nT, and the IMF Bz component was increasing from a slightly negative value. The IMF Bx and By components were near +3 and -3 nT, respectively (not shown), so the IMF had an “ortho-garden hose” orientation. Vsw was over 600 km/s and falling slightly during the interval, and Psw was near 3.4 nPa. Multiple substorm onsets occurred at 1809 UT at 66.70° MLAT and 2.75 h MLT; 18:48 UT at 70.6° MLAT and 7.13 h MLT; 19:08 UT at 65.94° MLAT and 6.01 h MLT; 19:48 UT at 65.94° MLAT and 6.69 h MLT; and 20:12 UT at 65.94° MLAT and 7.09 h MLT. The times of these onsets, shown in Figure 9a, were from ~1 - 3 hours before the beginning of the MPE interval, and they occurred ~7 to 12 h MLT away from the magnetometer stations shown in Figure 10.

The SML index decreased from -457 nT at the time of the latest substorm onset 20:12 UT) to -1022 nT at 20:23 UT, and returned to near -500 nT at 20:55 before dropping to -699 nT near the beginning of the MPE interval. The SMU index was relatively steady near 400 nT for nearly 3 hours, from 18:00 to 20:55 UT, before rising to 616 nT at 21:02 UT, the beginning of the MPE interval. The variation of SMU and SML approximately in tandem shortly before and during the interval suggests the occurrence of a magnetospheric convection event or pseudobreakup. Both SML and SMU values gradually returned to more quiet levels during and after the MPE interval.

Figures 9b and 9c show magnetograms from BAS LPM M79 and FHB, respectively, from 20:00 to 22:00 UT on this day. A single Bx minimum at M79 appeared at 21:07 UT, and two Bx minima appeared at FHB at 21:04 and 21:22 UT, respectively. The largest dBx/dt excursion at FHB was substantial (-6.7 nT/s), but was a factor of ~5 smaller than that at M79.

Figure 10 shows Bx component data from the four lowest latitude stations available in each hemisphere from 20:00 to 22:00 UT. Both ΔB_x and the derivatives in each component at the Antarctic stations (Figure 10a) were highly localized in MLAT: as shown in Table 3, the maximum $|dB_x/dt|$ value decreased to less than half its value at M79 within 1° and 1.7° toward higher and lower MLAT (at M81 and M78, respectively). The first MPE observed in Greenland occurred within ~3 minutes of the much larger MPE observed in Antarctica, and conversely there was no evidence of the second Greenland MPE at any of the Antarctic stations. Thus for both MPEs there was an apparent lack of conjugacy. However, as will be discussed in section 5, at least some of this lack of conjugacy might be attributed to longitudinal localization of both MPEs: BAS LPM stations M79 and M81 were located ~9° in magnetic longitude west of the

conjugate point of FHB – at distances of 431 and 429 km, respectively. Figures 11a,b show that magnetometer deflections and derivative amplitudes at stations at $|\text{MLAT}| > 70^\circ$ in both hemispheres were at near background levels.

The fourth column of Table 2 shows the maximum $|\text{dB}/\text{dt}|$ values for each component for the lowest latitude stations shown in Figure 10. During this interval the derivatives were again consistently larger in the southern hemisphere than at northern hemisphere stations at comparable latitudes. The largest derivative was in the X component at all stations shown except FHB, where it was largest in the Z component.

The observations at BAS LPMs M81, M79, and M78, located in nearly a straight line with similar MLON (to within 1.5°) and MLAT (to within 2.7°), can provide additional information about this MPE. The distance from M79 to M81 is 139 km, and from M79 to M78 is 240 km. At the most equatorward station, M78, the minimum in Bx occurred at 2105 UT. At M79 it occurred at 2107 UT, and at M81 it occurred at 2108 UT. This indicates a possible drift of the epicenter of the MPE westward and poleward. This drift is again consistent with that found in the Engebretson et al. (2019b) case studies.

3.4 Interval 4: 13 May 2015 05:30-08:00 UT YRDAY 15133

This extended post-midnight interval occurred during the main phase of a large magnetic storm (minimum SYM/H = -95 nT), as shown in Figure 12a. The IMF magnitude was near 15 nT before the beginning of the interval, and fell slightly to 12 nT at its end, and the IMF Bz component rose unsteadily from a large negative value (-13 nT) at 0500 UT to +4 nT by 07:00 UT. The IMF Bx and By components were near +10 and -7 nT, respectively (not shown), so the IMF again had an “ortho-garden hose” orientation. Vsw fluctuated slightly near 600 km/s during the event, and Psw varied near 7 nPa. Two substorm onsets occurred prior to this event, at 05:04 UT at 60.49° MLAT and 1.87 h MLT and at 05:25 UT at 67.47° MLAT and 21.15 h MLT. The times of these onsets were 26 min and 5 min, respectively, before the beginning of the shaded MPE interval, and they occurred ~1-2 and 6-7 h MLT away from the magnetometer stations shown in Figure 13, respectively.

The SMU index rose gradually beginning near 04:35 UT from ~ 250 nT to a maximum of 507 nT at 05:14 UT, fell to ~300 nT by 05:40 UT, and exhibited only modest variations during the remainder of the MPE interval. The SML index also began a gradual drop near 04:35 UT,

but declined sharply from the time of the second substorm onset, reaching a minimum of -1160 nT at 05:46 UT before gradually returning toward more quiet levels, reaching values near -300 nT near 08:00 UT.

The beginning and end times of this interval (05:30 to 08:00 UT) correspond to the duration of double-minimum negative bays in the Bx component at M81 (Figure 12b) and GHB (Figure 12c). These bays showed a rapid recovery in the Bx component between 06:30 and ~07:00 UT, followed by a slower recovery from 07:00 to 08:00 UT that was still characterized by large fluctuations in all 3 components. There was again little correspondence in the By and Bz components between the two stations.

Figure 13 shows that a large negative bay appeared all 14 stations shown, covering an MLAT range of $>10^\circ$, but was deeper and more extended at lower latitudes and in the southern hemisphere. This bay, and the many rapid perturbations embedded within it, resembles published signatures of omega band structures (e. g., Figure 4 of Opgenoorth et al., 1983). These multiple short-lived perturbations, which have been designated variously as Ps6 and Pi3 magnetic pulsations (Solov'yev et al., 1999), appeared in all 3 components at all stations (not shown), and were often largest in the By component, but were highly localized. At each station, the maximum derivative amplitude in each component is listed. Derivative amplitudes generally increased from higher to lower MLAT, but the largest derivatives appeared at different times at each station, and spanned the time range from 05:50 to 07:40 UT. Only at one neighboring station pair (FHB and GHB, separated by 262 km) at 06:55 UT was one simultaneous large perturbation observed. The blue arrows in each panel show the times of the largest derivatives in the Bx component. Two > 6 nT/s derivatives in Bx appeared at M83 and M81 (Figures 13g and 13h), and two > 8 nT/s derivatives in Bx appeared at NAQ (Figure 13n). At all other stations Bx derivative amplitudes were < 6 nT/s; for these only the largest Bx derivative is shown (2 of equal magnitude at SP and FHB).

Figure 14a shows that similar latitudinal profiles of ΔB_x occurred in both northern and southern hemispheres, with elevated values extending over nearly 15° MLAT and generally larger at lower latitudes, but their amplitude was 20% to 60% larger in the southern (winter) hemisphere. The derivative amplitudes (Figure 14b) were again larger at lower latitudes. They were again somewhat larger in the southern hemisphere, but showed large differences between

two pairs of Antarctic stations at similar MLAT but different MLON: M83 - M84 and PG4 – M85.

The fifth column of Table 2 shows the maximum $|dB/dt|$ values for each component for the lowest latitude stations shown in Figure 13. In contrast to the pre-midnight MPEs, the largest derivative observed at the stations shown in Figure 13 was in the Y component at 6 stations, equal in the Y and Z components at 1 station, in the X component at 5 stations, and in the Z component at 3 stations.

4. Comparison of amplitudes in conjugate hemispheres

In each of the 4 MPE intervals studied, the latitudinal profiles in conjugate hemispheres showed fair to good qualitative agreement (Figures 5, 8, 11, and 14). Conditions were dark at most sites in both hemispheres. During intervals 1, 3, and 4 both perturbation and derivative amplitudes were larger in the winter hemisphere by up to a factor of 3, but during the second (near-equinox) event, Antarctic stations recorded consistently larger amplitudes. Derivative amplitudes (but not perturbation amplitudes) also varied significantly between stations in the southern hemisphere that differed in magnetic longitude by 6° or more (e.g., the M84 - PG5 pair in Figure 8 and the M83 - M84 and PG4 – M85 pairs in Figure 14).

Many studies have suggested that MPEs are driven by localized field-aligned currents (e.g., Viljanen et al., 2001; Viljanen and Tanskanen, 2011; Belakhovsky et al., 2019), and in models of magnetosphere - ionosphere electrodynamic drivers it is physically intuitive to use a circuit analogy and distinguish between generators which deliver a fixed current and those in which the voltage is fixed (Lysak, 1990).

Distinctions between the applicability of these two drivers can be revealed by analyzing the dependence of the ground magnetic response on the ionospheric conductance. If the magnetospheric driving of a FAC behaves as a voltage generator, then one expects the ground magnetic field perturbation to increase as the ionospheric conductance increases. In contrast, if the magnetospheric process behaves as a current generator, one expects the intensity of magnetic field perturbations to remain only weakly sensitive to the ionospheric conductance.

Quantitative relationships between conjugate amplitudes and height-integrated ionospheric conductances for these two generators were examined by Pilipenko et al. (2019) using a simple "plasma box" model of the magnetosphere with asymmetric conjugate

ionospheres driven by an external current located at the magnetospheric equatorial plane. The ranges of validity of current and voltage generators are determined by the ratio between an internal generator resistance and a load resistance. For a FAC generator, the local ionospheric resistance above an observation site plays the role of a load resistance, whereas the magnetospheric Alfvén wave resistance and the resistance of the conjugate ionosphere play the role of an internal source resistance. Oscillatory FACs interact with the ionosphere in a different way depending on relationship between the driver periodicity τ and the Alfvén field line eigenperiod T_A .

For a forced quasi-DC driving ($\tau \gg T_A$),

$$\frac{\Delta B_x^{(N)}}{\Delta B_x^{(S)}} = \frac{\Sigma_H^{(N)}}{\Sigma_H^{(S)}}, \quad (1)$$

and for excitation of resonant field line oscillations ($\tau \sim T_A$),

$$\frac{\Delta B_x^{(N)}}{\Delta B_x^{(S)}} = \frac{\Sigma_H^{(N)}}{\Sigma_H^{(S)}} \frac{\Sigma_P^{(S)}}{\Sigma_P^{(N)}}. \quad (2)$$

The quasi-DC driving of a FAC corresponds to a voltage generator, for which the ground magnetic response is proportional to the ionospheric Hall conductance. The excitation of resonant field line oscillations corresponds to a current generator, for which the ground magnetic response only weakly depends on the ionospheric conductance.

In order to determine the applicability of either of these models, the ratio of conductances at conjugate points can be compared with the ratio of magnetic disturbance amplitudes. Because MPEs are localized in both latitude and longitude, it is best to focus on stations observing the maximal amplitude of the MPE as well as to examine these ratios at more than one station. The bottom panels of Figures 5, 8, 11, and 14 show the ionospheric conductances calculated for each interval at all available West Greenland and conjugate AAL-PIP and BAS-LPM stations. Solid lines and dashed lines in panel c) of these figures denote Pedersen conductances (Σ_P) and Hall conductances (Σ_H), respectively. These were determined using an updated AMIE procedure based on an empirical model parameterized by solar zenith angle and the solar radio flux index, $F10.7$ (Cousins et al. (2015)).

Cousins et al. (2015) also noted that on physical grounds one would expect auroral precipitation to contribute to ionospheric conductances. Panel d) of Figures 5, 8, and 14 shows

the above conductances plus conductances determined using the empirical relationship of Robinson et al (1987) that relates particle flux and energy output to conductance, using the Ovation Prime DMSP-based empirical auroral precipitation model (Newell et al., 2009, 2010, 2014). This augmented model contributed only negligible additional conductances for interval 3 because the modeled auroral zone was located below the MLAT range of the available stations, so Figure 11 does not include this additional panel.

However, Cousins et al. (2015) noted that large uncertainties remain in all current conductance models. They evaluated a number of conductance models and adjustments, including both of those described above, using metrics based on comparing SuperDARN plasma drift data to AMPERE field-aligned current data by means of these conductance models, and found that none of the model combinations they tested generated significantly better agreement. In addition, the localized field-aligned currents that drive MPEs are expected to produce localized increases of unknown size in ionospheric conductances, and no model including such effects yet exists.

During the northern winter event shown in Figure 5, the magnetic perturbations and derivatives were mostly somewhat larger in the northern hemisphere, but in both conductance models both Σ_P and Σ_H were larger in the southern hemisphere. These relations are opposite to those expected for a voltage generator. Southern hemisphere (summer) conductances based on the AMIE model (Figure 5c) increased relatively smoothly with MLAT, while in the augmented model (Figure 5d) the contribution of modeled auroral precipitation is evident for $MLAT < 70^\circ$. Northern hemisphere (winter) conductances based on the AMIE model were nearly constant, and the auroral contribution in the augmented model extended to 73° MLAT. These additions are consistent with the center of the modeled auroral zone being located at or equatorward of 65° MLAT.

Inverse interhemispheric patterns are evident in Figure 14cd during northern summer events: magnetic perturbations and derivatives were mostly larger in the southern hemisphere, and conductances were much larger in the northern hemisphere. Northern hemisphere (winter) conductances based on the AMIE model (Figure 14c) increased relatively smoothly with MLT, while southern hemisphere conductances were nearly constant. The augmented model (Figure 14d) again increased the conductances at lower latitudes, but in this case again more rapidly in the southern hemisphere. The MPE event in interval 3 (Figure 11) was considerably more

localized in latitude, and also occurred in a region with nearly constant conductances that was poleward of the modeled auroral zone. Both intervals 3 and 4 occurred during northern summer and showed the same seasonal interhemispheric patterns. It is also clear in Figures 5, 11, and 14 that peak MPE amplitudes occurred in latitudinal regions of near-constant conductances, based on both models. These relations indicate that for both pre-midnight and post-midnight events during solstice conditions the voltage generator model is not applicable to MPEs.

In order to make a more quantitative comparison between models, we chose 4 station pairs in regions of relatively constant conductances from both interval 1 (between 69° and 76° MLAT) and interval 4 (between 70° and 76° MLAT) and calculated both ΔB_x ratios and the AMIE model conductance ratios defined in equations (1) and (2). The ratios between left and right sides of equation (1) for a voltage generator model were 7.08 ± 3.96 and 0.159 ± 0.032 for intervals 1 and 4, respectively (nearly inverse between winter and summer), while the corresponding ratios of equation (2) for a current generator model were 1.48 ± 0.15 and 1.10 ± 0.17 , both much closer to unity, and thus approximately satisfying the equality. Comparisons for $|dB/dt|$ ratios were similar: the ratios for a voltage generator model were 6.16 ± 3.42 and 0.315 ± 0.172 for intervals 1 and 4, respectively, and the ratios for a current generator model were 1.31 ± 0.15 and 2.19 ± 1.28 . The greater scatter in the $|dB/dt|$ ratios for both models using data from interval 4 is consistent with the greater variability in $|dB/dt|$ values for this interval shown in Figure 14b, which we attributed to longitudinal variations. Given the known uncertainties in the modeled conductances (Cousins et al., 2015), comparison of these ratios indicates the reasonableness of using a current generator model to drive these events.

The conductances for the 16 March 2016 pre-midnight event that occurred close to equinox (Figure 8c,d) showed more complex behavior. The AMIE conductances were below 1 S in both hemispheres below 72° MLAT (Figure 8c), but the southern hemisphere conductances increased toward higher latitudes while the northern hemisphere conductances remained constant. The augmented conductances shown in Figure 8d again showed the influence of an auroral zone for $MLAT < \sim 72^\circ$. As with the other intervals, neither conductance profile matched the large-scale latitudinal profiles of magnetic perturbations or derivatives shown in Figures 8a and 8b; the largest perturbations and derivatives occurred between 66° and 72° MLAT, in ranges of relatively flat conductances in the AMIE model and of both high and low conductances in the augmented model. During this event both perturbations and derivatives were larger in the

southern hemisphere even near 72° MLAT, where the conductances for both models were nearly equal. In addition, the latitudinal profile in the southern hemisphere between 69° and 72° MLAT (blue traces) showed sharp changes in conductances between M84 and PG5 and between PG4 and M85 (Figures 8b,c) that correspond to sharp changes in derivative and perturbation amplitude (Figures 8a,b). Similar sharp changes also appeared in Figure 11c. As noted near the beginning of this section, these changes appear to be linked to differences in station longitude, but the relative polarity of the changes is more consistent with a voltage generator model than a current generator model.

Several factors may complicate the modeling of ionospheric conductances in magnetically conjugate points, especially near equinoxes: a) the differing effects on ground conductivity of coastlines and oceans in the north vs. ice sheets in the south, b) the different distances and azimuths between the geographic and geomagnetic poles in opposite hemispheres (Liou et al., 2018), and c) the fact that Antarctic stations in this study were situated at 13-18° higher geographic latitude than Arctic stations at similar MLAT. However, addressing these factors quantitatively is beyond the scope of this paper.

5. Discussion

This study has presented four examples of nighttime MPEs observed by multiple magnetometers in near-magnetically conjugate regions in both polar regions. We here summarize both the commonalities and differences between these events.

The geomagnetic context of these four MPE intervals was similar only in that the B_z component of the IMF was < 0 before each event, and had at least a modest increase at or near the time of the event. MPEs could occur during both magnetically quiet times and storm times, but little or no change in solar wind pressure or velocity occurred shortly before or during each event, and there was no consistent pattern in IMF B_x or B_y levels or trends. Clear minima in the SML index were evident in each of the MPE intervals presented here, but as was the case for the statistical and event studies of MPEs presented by Engebretson et al. (2019a,b), there was no consistent timing of events relative to the most recent substorm onset(s).

The availability of data from latitudinally-spaced stations covering nearly 15° in MLAT makes it possible to characterize the latitudinal extent of individual MPEs. Pre-midnight MPEs did not extend over large latitude ranges: one, two, or three independent events could appear

across the available latitude range, with the more poleward events occurring some few minutes later. Simultaneous large-amplitude pre-midnight impulses in event 1 occurred over an MLAT range of ~320 km (the distance from STF to GHB, the extent of the central range in Figure 4). In event 2 they occurred over ranges from 436 km (the distance from PG4 to M84, the central range in Figure 7 in which a large negative B_x impulse dominated the signal) to 703 km (the distance from PG4 to M79, the full range of latitudes over which a B_x minimum near 0037 UT was observed).

The amplitude and location data for the MPE event during interval 3 (Figure 11) can be used to estimate its latitudinal and longitudinal scale size. Using a linear slope calculation between pairs of stations gives the half-amplitude falloff distances shown in Table 3. For the two lowest-latitude and relatively closely-spaced BAS-LPM station pairs, these latitudinal distances ranged from 106 to 192 km, and for the two somewhat less closely-spaced West Greenland stations at nearly the same magnetic longitude, 204 km. The longitudinal half-amplitude falloff distances between BAS LPM stations M81 and M79 and the conjugate location to Greenland station FHB were 446 and 262 km, respectively. These latitudinal distances are roughly comparable to but mostly lower than the ~275 km two-dimensional half-amplitude radius calculated for several events in Arctic Canada using the SECs technique by Engebretson et al. (2019a,b), and the longitudinal distances are comparable to or somewhat higher. An MPE event with even larger differences in perturbation amplitude between relatively closely spaced stations than this one is shown in Figures 3 and 4 of Pulkkinen et al. (2015).

During the extended post-midnight interval multiple highly localized MPEs occurred independently in time at each station in both hemispheres, embedded within large amplitude, longer-duration magnetic bays (Figure 13). Only at the FHB-GHB station pair did one event occur simultaneously. MPE derivative amplitudes ≥ 6 nT/s appeared from 65.0° to 71.9° MLAT (NAQ to STF, a distance of 700 km). Based on the latitudinal profiles in Figure 14, showing increasing perturbation and derivative amplitudes toward the lower MLAT end of the range of available stations, we consider it to be likely that these bays and their associated large MPEs may have extended even farther equatorward.

The pre- and post-midnight MPEs also differed in the directions of their largest perturbations. Pre-midnight MPEs were often largest in the B_x component, with some largest in B_z but with B_y largest at only one station (out of 37) in all 3 events. In contrast, post-midnight

MPEs were most often largest in the By component. This difference is consistent with earlier observations reported by Viljanen et al. (2001), who noted the strong southward direction of magnetic field fluctuations for large events in the auroral zone midnight sector, compared to a more East–West alignment in the morning sector.

Many of the nighttime MPEs in intervals 1 and 2 occurred simultaneously to within 1-2 minutes in latitudinal ranges of 300-700 km in conjugate hemispheres. The MPEs in interval 3 exhibited more significant differences between hemispheres, but these may have been caused by the greater longitudinal separation between available conjugate stations during this interval. Although it might be expected that magnetic perturbations in high latitude regions should show some symmetry (or at least some form of direct control of asymmetry by the orientation of the interplanetary magnetic field, season, or ionospheric conductivity), Kim et al. (2013) documented that this is seldom true for dayside magnetic impulse events (the high latitude geomagnetic response to sudden changes in solar wind pressure). They suggested that these asymmetric dayside ground responses might be of local origin rather than magnetospheric origin.

5.1 Connection to omega bands and their physical mechanisms

Because only magnetometer data are utilized in this study, we have no additional information about auroral phenomena that might contribute to the causal chain leading to these events, as was provided for the 3 events presented by Engebretson et al. (2019b). That study included a SECS (spherical elementary current systems) analysis using a large 2-d set of magnetometers across North America and Greenland (Weygand et al., 2011) as well as auroral snapshots from the THEMIS all-sky imager array and GOES 13 dipolarization data. However, we comment briefly on the post-midnight interval and explore why we link it to the occurrence and physics of omega bands.

Opgenoorth et al. (1983) characterized the source of omega bands as a “meandering” ionospheric Hall current, composed of a westward background electrojet and circular Hall current vortices around the locations of localized field-aligned currents, and Opgenoorth et al. (1994) equivalently described them as “large-scale auroral vortex streets.” Omega bands have also been closely associated with long period irregular Pi3 or Ps6 magnetic pulsations with periods of 5 – 15 min (e.g., Kawasaki and Rostoker, 1979; Andre and Baumjohann, 1982; Solov'yev et al., 1999; Henderson et al., 2002, and Wild et al., 2011). Apatenkov et al. (2020)

provided detailed observations of a very large GIC that was associated with an interval of omega bands. They modeled this event using the sum of two basic current systems: a 1D linear current (mimicking the auroral electrojet) and a 2D vortex that passed eastward over the field of view of the ground magnetometers. As a result of pointing out that the magnetic field created by ionospheric and magnetospheric currents may vary due to both temporal changes of current amplitudes and to the motion of the current structures, they suggested that propagating nonexplosive and relatively long-lived structures might be responsible for large rapid magnetic field variations if their propagation speeds were sufficiently large.

The magnetospheric source of these currents may be, as Partamies et al. (2017) and Weygand et al. (2015) have suggested, fast earthward flows in the magnetotail, e.g., bursty bulk flows (BBFs, Angelopoulos et al., 1992) or the more localized dipolarizing flux bundles (DFBs) described by Liu et al. (2014). Palin et al. (2015) found that highly localized FACs and ionospheric currents were associated with BBFs and/or dipolarizing flux bundles observed by THEMIS spacecraft in the near magnetotail, and suggested that these might be the smallest elements of substorms and pseudobreakups. A recent satellite-ground study by Liu et al. (2018) also found that omega bands are related to a flow shear near the inner edge of the plasma sheet, and suggested that an enhanced flow in the magnetosphere drives the omega bands by triggering plasma instabilities. Within a BBF, the flow velocity exhibits peaks of very large amplitude with a characteristic time scale of the order of a minute, which are usually associated with magnetic field dipolarizations and ion temperature increases.

Although mid- or small-scale magnetotail flows are likely the ultimate sources for the field-aligned and ionospheric currents that generate nighttime MPEs, the contrast between the highly localized nature of the MPEs at each station observed during the post-midnight event and the larger-scale synchronicity of MPEs observed during the three pre-midnight events suggests that even smaller-scale magnetosphere-ionosphere coupling processes and resulting plasma instabilities may play a significant role in generating post-midnight MPEs. We note that Sato et al. (2017) similarly concluded their study of omega bands by strongly suggesting that magnetosphere-ionosphere coupling should play an important role in the formation of omega band auroras.

6. Summary and Conclusions

Under both quiet and moderately disturbed geomagnetic conditions large pre-midnight MPEs at high magnetic latitudes exhibited fair to good hemispheric conjugacy in the timing of the equatorward excursion of their N-S component (ΔB_x) and fair conjugacy in their latitudinal profiles and amplitude peaks. During interval 3, which occurred during a highly disturbed interval, there was little similarity in MPE occurrence or amplitude between hemispheres, but the MPE appeared to be highly localized in both latitude and longitude, and available stations in opposite hemispheres were separated in longitude. Although the opposite orientation of the ΔB_y perturbations in conjugate hemispheres was consistent with Hall currents surrounding localized FACs, the shapes of the perturbations in the B_y and B_z components were rarely similar in conjugate hemispheres.

The ΔB_x amplitude was largest in the winter hemisphere during 3 of the 4 intervals presented here, and comparison of conjugate amplitudes and modeled ionospheric conductances suggested that the MPEs were fit much better by a current generator model than by a voltage generator model. However, during near-equinox interval 2 the ΔB_x amplitudes were strongest in the southern hemisphere, and neither a simple current or voltage generator model was consistent with these amplitudes. In addition, a conductance model including auroral precipitation effects may suggest that the MPEs observed in this study occurred at or poleward of the poleward edge of the auroral zone, consistent with the multi-instrument MPE case studies of Engebretson et al. (2019b).

These large nighttime MPEs occurred under a range of solar wind and IMF conditions, but common to all four intervals was a negative IMF B_z that exhibited at least a modest increase at or near the time of the event.

Large dB/dt values occurred both pre- and post-midnight. During the 3 pre-midnight events they were usually isolated and were largest in the X and Z components and smallest in Y at all but one station in one pre-midnight event. During the post-midnight interval they were grouped in quasi-periodic patterns embedded within a large magnetic bay, and the largest values occurred more often in the Y component than in X or Z.

The local time range of the more clearly impulsive events matches that of BBFs and/or dipolarizing flux bundles, while the range of the dawn sector events matches that of omega bands. These results may indicate that two separate and highly localized magnetosphere-

ionosphere coupling mechanisms may be responsible for generating the large, rapid geomagnetic perturbations that generate GICs.

Acknowledgements

This work was supported by National Science Foundation grants AGS-1651263 to Augsburg University, AGS-1654044 to the University of Michigan, OPP-1744828 to Virginia Tech, and OPP-1643700 to the New Jersey Institute of Technology; and Natural Environmental Research Council grant NE/R016038/1 to the British Antarctic Survey. HO and AS thank the National Swedish Space Agency (SNSA) for support.

Solar wind and IMF data are available at the Goddard Space Flight Center Space Physics Data Facility at <https://cdaweb.sci.gsfc.nasa.gov/index.html/>, as are also data from the Greenland West Coast magnetometer chain. MACCS and CANMOS magnetometer data are available in IAGA 2002 ASCII format at <http://space.augsburg.edu/maccs/requestdatafile.jsp> and <http://geomag.nrcan.gc.ca/data-donnee/sd-en.php>, respectively. South Pole Station magnetometer data are available in ASCII format at <https://antarcticgeospace.njit.edu/Data/>. AAL-PIP magnetometer data are available in CDF and IDL save set formats at <http://mist.nianet.org/> and in ASCII format at <https://cdaweb.gsfc.nasa.gov>. BAS LPM magnetometer data are available at <https://data.bas.ac.uk/full-record.php?id=GB/NERC/BAS/AEDC/00263>.

The SML and SMU indices are available at <http://supermag.jhuapl.edu/indices/>, and the SuperMAG substorm database is available at <http://supermag.jhuapl.edu/substorms/>. Jesper Gjerloev is SuperMAG Principal Investigator. These SuperMAG products are derived from magnetometer data from INTERMAGNET, Alan Thomson; USGS, Jeffrey J. Love; CARISMA, PI Ian Mann; CANMOS, Geomagnetism Unit of the Geological Survey of Canada; The S-RAMP Database, PI K. Yumoto and Dr. K. Shiokawa; The SPIDR database; AARI, PI Oleg Troshichev; The MACCS program, PI M. Engebretson; GIMA; MEASURE, UCLA IGPP and Florida Institute of Technology; SAMBA, PI Eftyhia Zesta; 210 Chain, PI K. Yumoto; SAMNET, PI Farideh Honary; IMAGE, PI Liisa Juusola; Finnish Meteorological Institute, PI Liisa Juusola; Sodankylä Geophysical Observatory, PI Tero Raita; UiT the Arctic University of Norway, Tromsø Geophysical Observatory, PI Magnar G. Johnsen; GFZ German Research Centre For Geosciences, PI Jürgen Matzka; Institute of Geophysics, Polish Academy of

Sciences, PI Anne Neska and Jan Reda; Polar Geophysical Institute, PI Alexander Yahnin and Yaroslav Sakharov; Geological Survey of Sweden, PI Gerhard Schwarz; Swedish Institute of Space Physics, PI Masatoshi Yamauchi; AUTUMN, PI Martin Connors; DTU Space, PI Dr. Thom R. Edwards and Anna Willer; PENGUIn; South Pole and McMurdo Magnetometer, PIs Louis J. Lanzerotti and Allan T. Weatherwax; ICESTAR; RAPIDMAG; British Antarctic Survey; McMAC, PI Dr. Peter Chi; BGS, PI Dr. Susan Macmillan; Pushkov Institute of Terrestrial Magnetism, Ionosphere and Radio Wave Propagation (IZMIRAN);; MFGL, PI B. Heilig; Institute of Geophysics, Polish Academy of Sciences, PI Anne Neska and Jan Reda; and University of L'Aquila, PI M. Vellante; BCMT, V. Lesur and A. Chambodut; Data obtained in cooperation with Geoscience Australia, PI Marina Costelloe; AALPIP, co-PIs Bob Clauer and Michael Hartinger; SuperMAG; Data obtained in cooperation with the Australian Bureau of Meteorology, PI Richard Marshall.

References

- André, D., and W. Baumjohann (1982), Joint two-dimensional observations of ground magnetic and ionospheric electric fields associated with auroral currents. 5. Current system associated with eastward drifting omega bands, *Journal of Geophysics*, 50, 194–201, <https://journal.geophysicsjournal.com/JofG/article/view/201>.
- Angelopoulos, V., W. Baumjohann, C. F. Kennel, F. V. Coroniti, M. G. Kivelson, R. Pellat, R. J. Walker, H. Luehr, and G. Paschmann, (1992), Bursty bulk flows in the inner central plasma sheet. *Journal of Geophysical Research*, 97, 4027–4039, doi:10.1029/91JA02701
- Apatenkov, S. V., V. A. Sergeev, R. Pirjola, and A. Viljanen (2004), Evaluation of the geometry of ionospheric current systems related to rapid geomagnetic variations, *Annales Geophysicae*, 22, 63-72, doi:10.5194/angeo-22-63-2004
- Apatenkov, S. V., Pilipenko, V. A., Gordeev, E. I., Viljanen, A., Juusola, L., Belakhovsky, V. B., Sakharov, Ya. A., and Selivanov, V. N. (2020), Auroral omega bands are a significant cause of large geomagnetically induced currents, *Geophysical Research Letters*, 47, e2019GL086677, doi:10.1029/2019GL086677
- Belakhovsky, V., V. Pilipenko, M. Engebretson, Ya. Sakharov, and V. Selivanov (2019), Impulsive disturbances of the geomagnetic field as a cause of induced currents of electric

power lines, *Journal of Space Weather and Space Climate*, 9, A18,
doi:10.1051/swsc/2019015

Clauer, C. R., H. Kim, K. Deshpande, Z. Xu, D. Weimer, S. Musko, G. Crowley, C. Fish, R. Nealy, T. E. Humphreys, J. A. Bhatti, and A. J. Ridley (2014), An autonomous adaptive low-power instrument platform (AAL-PIP) for remote high-latitude geospace data collection, *Geosci. Instrum. Method. Data Syst.*, 3, 211–227, doi:10.5194/gi-3-211-2014

Cousins, E. D. P., T. Matsuo, and A. D. Richmond (2015), Mapping high-latitude ionospheric electrodynamics with SuperDARN and AMPERE, *J. Geophys. Res. Space Physics*, 120, 5854–5870, doi:10.1002/2014JA020463

Dimmock, A. P., L. Rosenqvist, J.-O. Hall, A. Viljanen, E. Yordanova, I. Honkonen, M. André, and E. C. Sjöberg (2019), The GIC and geomagnetic response over Fennoscandia to the 7–8 September 2017 geomagnetic storm, *Space Weather*, 17, 989–1010, <https://doi.org/10.1029/2018SW002132>

Engebretson, M. J., W. J. Hughes, J. L. Alford, E. Zesta, L. J. Cahill, Jr., R. L. Arnoldy, and G. D. Reeves (1995), Magnetometer array for cusp and cleft studies observations of the spatial extent of broadband ULF magnetic pulsations at cusp/cleft latitudes, *Journal of Geophysical Research*, 100, 19371–19386, doi:10.1029/95JA00768

Engebretson, M. J., Araki, T., Arnoldy, R. L., Carpenter, D. L., Doolittle, J. H., Fukunishi, H., et al. (1997), The United States automatic geophysical observatory (AGO) program in Antarctica, in M. Lockwood, M. N. Wild, & H. J. Opgenoorth (Eds.), *the Satellite—Ground Based Coordination Sourcebook*, ESA-SP-1198 (pp. 65–99). ESTEC, Noordwijk, Netherlands: ESA Publications.

Engebretson, M. J., Pilipenko, V. A., Ahmed, L. Y., Posch, J. L., Steinmetz, E. S., Moldwin, M. B., Connors, M. G., Weygand, J. M., Mann, I. R., Boteler, D. H., Russell, C. T., and Vorobev, A. V. (2019a), Nighttime magnetic perturbation events observed in Arctic Canada: 1. Survey and statistical analysis, *Journal of Geophysical Research: Space Physics*, 124, 7442–7458, doi:10.1029/2019JA026794

Engebretson, M. J., E. S. Steinmetz, J. L. Posch, V. A. Pilipenko, M. B. Moldwin, M. G. Connors, D. H. Boteler, I. R. Mann, M. D. Hartinger, J. M. Weygand, L. R. Lyons, Y. Nishimura, H. J. Singer, S. Ohtani, C. T. Russell, A. Fazakerley, and L. M. Kistler (2019b), Nighttime magnetic perturbation events observed in Arctic Canada: 2.

- Multiple-instrument observations, *Journal of Geophysical Research: Space Physics*, 124, 7459–7476, doi:10.1029/2019JA026797
- Gabrielse, C., V. Angelopoulos, A. Runov, and D. L. Turner (2014), Statistical characteristics of particle injections throughout the equatorial magnetotail, *Journal of Geophysical Research: Space Physics*, 119, 2512–2535, doi:10.1002/2013JA019638
- Henderson, M. G., Reeves, G. D., and Murphree, J. S. (1998), Are north-south aligned auroral structures an ionospheric manifestation of bursty bulk flows?, *Geophysical Research Letters*, 25, 3737–3740, doi:10.1029/98GL02692
- Henderson, M. G., Kepko, L., Spence, H. E., Connors, M., Sigwarth, J. B., Frank, L. A., Singer, H., J., and Yumoto, K. (2002), The evolution of north-south aligned auroral forms into auroral torch structures: The generation of omega bands and Ps6 pulsations via flow bursts, in the *Proceedings of the Sixth International Conference on Substorms*, edited by R. M. Winglee, University of Washington, Seattle, WA, ISBN:0971174032 9780971174030
- Kadokura, A., H. Yamagishi, N. Sato, K. Nakano, and M. C. Rose (2008), Unmanned magnetometer network observation in the 44th Japanese Antarctic Research Expedition: Initial results and an event study on auroral substorm evolution, *Polar Science* 2, 223–235, doi:10.1016/j.polar.2008.04.002
- Kauristie, K., Sergeev, V. A., Kubyshkina, M., Pulkkinen, T. I., Angelopoulos, V., Phan, T., Lin, R. P., and Slavin, J. A. (2000), Ionospheric current signatures of transient plasma sheet flows, *Journal of Geophysical Research*, 105, 10,677–10,690, doi:10.1029/1999JA900487
- Kawasaki, K., and Rostoker, G. (1979), Perturbation magnetic fields and current systems associated with eastward drifting auroral structures, *Journal of Geophysical Research*, 84, 1464–1480, doi:10.1029/JA084iA04p01464
- Kim, H., X. Cai, C. R. Clauer, B. S. R. Kunduri, J. Matzka, C. Stolle, and D. R. Weimer (2013), Geomagnetic response to solar wind dynamic pressure impulse events at high-latitude conjugate points, *J. Geophys. Res. Space Physics*, 118, 6055–6071, doi:10.1002/jgra.50555.
- Kozyreva, O. V., V. A. Pilipenko, V. B. Belakhovsky, and Ya. A. Sakharov (2018), Ground geomagnetic field and GIC response to March 17, 2015 storm, *Earth, Planets and Space*,

769 70:157, doi:10.1186/s40623-018-0933-2

770 Lanzerotti, L. J., A. Wolfe, N. Trivedi , C. G. MacLennan, and L. V. Medford (1990), Magnetic
771 impulse events at high latitudes: Magnetopause and boundary layer plasma processes,
772 *Journal of Geophysical Research*, 95, 97-107, doi:10.1029/JA095iA01p00097

773 Liou, K., T. Sotirelis, and E. J. Mitchell (2018), North-south asymmetry in the geographic
774 location of auroral substorms correlated with ionospheric effects, *Scientific Reports*, 8,
775 17230, doi:10.1038/s41598-018-35091-2

776 Liu, J., V. Angelopoulos, X.-Z. Zhou, and A. Runov (2014), Magnetic flux transport by
777 dipolarizing flux bundles, *Journal of Geophysical Research: Space Physics*, 119, 909–
778 926, doi:10.1002/2013JA019395

779 Liu, J., L. R. Lyons, W. E. Archer, B. Gallardo-Lacourt, Y. Nishimura, Y. Zou, C. Gabrielse, and
780 J. M. Weygand (2018), Flow shears at the poleward boundary of omega bands observed
781 during conjunctions of Swarm and THEMIS ASI, *Geophysical Research Letters*, 45,
782 1218–1227, doi:10.1002/2017GL076485

783 Lyons, L. R., Nishimura, Y., Xing, X., Runov, A., Angelopoulos, V., Donovan, E., and Kikuchi,
784 T. (2012), Coupling of dipolarization front flow bursts to substorm expansion phase
785 phenomena within the magnetosphere and ionosphere, *Journal of Geophysical Research*,
786 117, A02212, doi:10.1029/2011JA017265

787 Lysak, R. L. (1990), Electrodynamic coupling of the magnetosphere and ionosphere, *Space*
788 *Science Reviews*, 52, 33–87, doi:10.1007/BF00704239

789 Mravlag, E., Scourfield, M. W. J., Walker, A. D. M., Sutcliffe, P. R., and Nielsen, E. (1991),
790 Simultaneous observations of omega band related phenomena in both hemispheres,
791 *Journal of Atmospheric and Terrestrial Physics*, 53, 309–317, doi:10.1016/
792 0021-9169(91)90114-m

793 Newell, P. T., T. Sotirelis, and S. Wing (2009), Diffuse, monoenergetic, and broadband aurora:
794 The global precipitation budget, *Journal of Geophysical Research*, 114, A09207,
795 doi:10.1029/2009JA014326.

796 Newell, P. T., T. Sotirelis, and S. Wing (2010), Seasonal variations in diffuse, monoenergetic,
797 and broadband aurora, *Journal of Geophysical Research*, 115, A03216,
798 doi:10.1029/2009JA014805.

799 Newell, P. T., and J. W. Gjerloev (2011), Evaluation of SuperMAG auroral electrojet indices as

indicators of substorms and auroral power, *Journal of Geophysical Research*, 116, A12211, doi:10.1029/2011JA016779

Newell, P. T., Liou, K., Zhang, Y., Sotirelis, T., Paxton, L. J., and Mitchell, E. J. (2014), OVATION Prime-2013: Extension of auroral precipitation model to higher disturbance levels, *SpaceWeather*, 12, 368–379, doi:10.1002/2014SW001056

Ngwira, C. M., A. A. Pulkkinen, E. Bernabeu, J. Eichner, A. Viljanen, and G. Crowley (2015), Characteristics of extreme geoelectric fields and their possible causes: Localized peak enhancements, *Geophysical Research Letters*, 42, 6916–6921, doi:10.1002/2015GL065061

Ngwira C. M., D. G. Sibeck, M. D. V. Silveira, M. Georgiou, J. M. Weygand, Y. Nishimura, and D. Hampton (2018), A study of intense local dB/dt variations during two geomagnetic Storms, *Space Weather*, 16, 676–693, doi:10.1029/2018SW001911.

Ngwira, C. M., and A. A. Pulkkinen (2019), An introduction to geomagnetically induced currents (2019), in *Geomagnetically Induced Currents from the Sun to the Power Grid*, Geophysical Monograph Series, 244, edited by J. L. Gannon, A. Swidinsky, and Z. Xu, American Geophysical Union, Washington, D.C., 3-14, doi:10.1002/9781119434412.ch1

Nikitina, L., Trichtchenko, L., and Boteler, D. H. (2016), Assessment of extreme values in geomagnetic and geoelectric field variations for Canada. *Space Weather*, 14, 481–494, doi:10.1002/2016SW001386

Opgenoorth, H. J., Oksman, J., Kaila, K. U., Nielsen, E., and Baumjohann, W. (1983), Characteristics of eastward drifting omega bands in the morning sector of the auroral oval, *Journal of Geophysical Research*, 88, 9171–9185, doi:10.1029/JA088iA11p09171

Opgenoorth, H. J., M. A. L. Persson, T. I. Pulkkinen, and R. J. Pellinen (1994), Recovery phase of magnetospheric substorms and its association with morning-sector aurora, *Journal of Geophysical Research*, 99, 4115–4129, doi:10.1029/93JA01502

Palin, L., C. Jacquey, H. Opgenoorth, M. Connors, V. Sergeev, J.-A. Sauvaud, R. Nakamura, G. D. Reeves, H. J. Singer, V. Angelopoulos, and L. Turc (2015), Three-dimensional current systems and ionospheric effects associated with small dipolarization fronts, *J. Geophys. Res. Space Physics*, 120, 3739–3757, doi:10.1002/2015JA021040

Partamies, N., Weygand, J. M., and Juusola, L. (2017), Statistical study of auroral omega bands, *Annales Geophysicae*, 35, 1069–1083, doi:10.5194/angeo-35-1069-2017

- Pilipenko, V. A., Fedorov, E. N., Hartinger, M. D., and Engebretson, M. J. (2019), Electromagnetic fields of magnetospheric ULF disturbances in the ionosphere: Current/voltage Dichotomy, *Journal of Geophysical Research: Space Physics*, 124, 109–121, doi:10.1029/2018JA026030
- Pulkkinen, A., E. Bernabeu, J. Eichner, A. Viljanen, and C. Ngwira (2015), Regional-scale high-latitude extreme geoelectric fields pertaining to geomagnetically induced currents, *Earth, Planets, and Space*, 67, 93, doi:10.1186/s40623-015-0255-6
- Robinson, R. M., R. R. Vondrak, K. Miller, T. Dabbs, and D. Hardy (1987), On calculating ionospheric conductances from the flux and energy of precipitating electrons, *Journal of Geophysical Research*, 92, 2565–2569, doi:10.1029/JA092iA03p02565
- Sato, N., Yukimatu, A. S., Tanaka, Y., and Hori, T. (2017), Morphologies of omega band auroras, *Earth, Planets and Space*, 69, 103,
- Sergeev, V. A., Liou, K., Meng, C.-I., Newell, P. T., Brittnacher, M., Parks, G., and Reeves, G. D. (1999), Development of auroral streamers in association with localized impulsive injections to the inner magnetotail, *Geophysical Research Letters*, 26, 417–420, doi:10.1029/1998GL900311
- Solovyev, S. I., Baishev, D. G., Barkova, E. S., Engebretson, M. J., Posch, J. L., Hughes, W. J., Yumoto, K., and Pilipenko, V. A. (1999), Structure of disturbances in the dayside and nightside ionosphere during periods of negative interplanetary magnetic field Bz, *Journal of Geophysical Research*, 104, 28,019–28,039, doi:10.1029/1999JA900286
- Viljanen A. (1997), The relation between geomagnetic variations and their time derivatives and implications for estimation of induction risks, *Geophysical Research Letters*, 24, 631–634, doi:10.1029/97GL00538
- Viljanen, A., Nevanlinna, H., Pajunpää, K., and Pulkkinen, A. (2001), Time derivative of the horizontal geomagnetic field as an activity indicator, *Annales Geophysicae*, 19(9), 1107–1118, doi:10.5194/angeo-19-1107-2001
- Viljanen, A., E. I. Tanskanen, and A. Pulkkinen (2006), Relation between substorm characteristics and rapid temporal variations of the ground magnetic field, *Annales Geophysicae*, 24, 725–733, doi:10.5194/angeo-24-725-2006.

- Viljanen, A., and Tanskanen, E. (2011), Climatology of rapid geomagnetic variations at high latitudes over two solar cycles, *Annales Geophysicae*, 29, 1783–1792, doi:10.5194/angeo-29-1783-2011
- Weygand, J. M., O. Amm, A. Viljanen, V. Angelopoulos, D. Murr, M. J. Engebretson et al. (2011), Application and validation of the spherical elementary currents systems technique for deriving ionospheric equivalent currents with the North American and Greenland ground magnetometer arrays, *Journal of Geophysical Research*, 116, A03305, doi:10.1029/2010JA016177
- Weygand, J. M., Kivelson, M. G., Frey, H. U., Rodriguez, J. V., Angelopoulos, V., Redmon, R., and Amm, O. (2015), An interpretation of spacecraft and ground based observations of multiple omega band events, *Journal of Atmospheric and Solar-Terrestrial Physics*, 133, 185–204, doi:10.1016/j.jastp.2015.08.014
- Wild, J. A., Woodfield, E. E., Donovan, E., Fear, R. C., Grocott, A., Lester, M., Fazakerley, A. N., Lucek, E., Khotyaintsev, Y., Andre, M., Kadokura, A., Hosokawa, K., Carlson, C., McFadden, J. P., Glassmeier, K. H., Angelopoulos, V., and Björnsson, G. (2011), Midnight sector observations of auroral omega bands, *Journal of Geophysical Research*, 116, A00130, doi:10.1029/2010JA015874
- Zesta, E., Lyons, L., and Donovan, E. (2000), The auroral signature of Earthward flow bursts observed in the magnetotail, *Geophysical Research Letters*, 27, 3241–3244, doi:10.1029/2000GL000027
- Zesta, E., Lyons, L., Wang, C.-P., Donovan, E., Frey, H., and Nagai, T. (2006), Auroral poleward boundary intensifications (PBIs): Their two-dimensional structure and associated dynamics in the plasma sheet, *Journal of Geophysical Research*, 111, A05201, doi:10.1029/2004JA010640

893

894

895

Table 1. Magnetometer Stations Used in This Study

Northern Hemisphere					Southern Hemisphere				
Array	Geogr Lat	Geogr Lon	CGM Lat	CGM Lon	Array	Geogr Lat	Geogr Lon	CGM Lat	CGM Lon
MACCS									
Pangnirtung	66.1°	294.2°	73.2°	19.8°	South Pole	-90.00 °	--	-74.5°	18.7°
CANMOS									
Iqaluit	63.8°	291.5°	71.4°	15.2°	AAL-PIP				
Greenland Coastal Chain					PG0	-83.67°	88.68°	-78.7°	38.2°
THL	77.47°	290.77°	84.0°	26.4°	PG1	-84.50°	77.20°	-77.3°	37.3°
TAB	76.54°	291.18°	83.2°	25.0°	PG2	-84.42°	57.95°	-75.7°	39.1°
SVS	76.02°	294.90°	82.3°	30.4°	PG3	-84.81°	37.63°	-73.9°	36.7°
KUV	74.57°	302.82°	80.0°	39.4°	PG4	-83.34°	12.25°	-71.2°	36.4°
UPN	72.78°	303.85°	78.2°	38.1°	PG5	-81.96°	5.71°	-69.9°	37.2°
UMQ	70.68°	307.87°	75.7°	40.8°	British Antarctic Survey Low Power Magnetometer Chain				
GDH	69.25°	306.47°	74.5°	37.8°	M85-002	-85.36°	2.06°	-71.8°	30.1°
ATU	67.93°	306.43°	73.2°	36.8°	M84-336	-84.36°	-23.85°	-69.8°	25.9°
STF	67.02°	309.28°	71.9°	39.5°	M83-348	-82.90°	-12.25°	-69.2°	30.6°
SKT	65.42°	307.10°	70.7°	36.1°	M81-338	-80.89°	-22.25°	-67.0°	29.2°
GHB	64.17°	308.27°	69.2°	36.8°	M79-336	-79.68°	-24.12°	-66.0°	29.3°
FHB	62.00°	310.32°	66.6°	38.1°	M78-337	-77.52°	-23.42°	-64.3°	30.7°
NAQ	61.16°	314.56°	65.0°	42.3°					

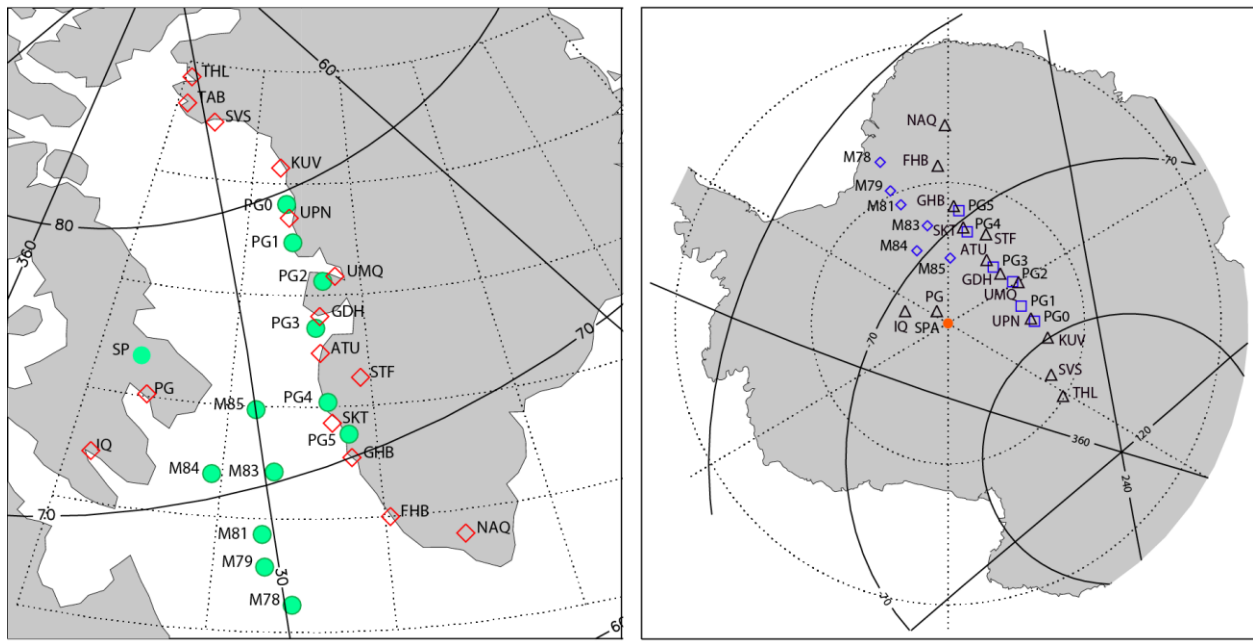
Note: Corrected geomagnetic (CGM) coordinates were calculated for epoch 2016 (using http://sdnet.thayer.dartmouth.edu/aacgm/aacgm_calc.php#AACGM).

Table 2. The maximum |dB/dt| values for each component for each of the stations shown during each of the intervals presented here.

Station	15 Jan 2018	16 Mar 2018	8 May 2016	13 May 2015
SPA	-15.1, -, -	7.5,-12.1, 4.9		-3.3, -, -
PGG	-9.1, 5.7, 4.3	-6.3, 3.3, 4.4		3.2, 2.5, 1.9
IQA		2.0, 1.7, 2.0		-3.8, 3.4, 4.9
PG2	4.9, 2.6, -3.1	4.2, -3.3, 3.8		-3.6, 4.3, 2.7
PG3	- 8.1, 6.4, -9.8	8.6, 4.2, 4.8		5.4, -3.4, -5.7
PG4		-13.2,-11.4, 13.6		5.2, 5.2, -6.1
PG5	-8.0, 5.5, 7.8	-16.2, 13.3,-12.0		
M85				3.2, 1.9, 1.9
M84		-25.7, 12.7, 5.2		
M83				7.7, 6.7, 4.2
M81		15.6, 8.6, 9.6	-12.9, -3.2, -4.0	-7.7,-10.7,-6.1
M79	3.4, -2.3, 1.2	15.8, 6.3, 3.4	37.7, 13.7, 19.5	
M78	4.5, 3.8, -3.3		14.4, 9.1, 10.3	
UMQ	-8.8, 3.8, 4.9			2.1, 1.5, 1.6
GDH	-10.0,-10.6,-12.7	3.0, 2.2, -4.5		-2.8, 1.6, 2.0
STF	-12.8, -7.0, -8.9	-7.2, -5.6, -7.1		3.1, 6.0, -3.7
SKT		- 6.4,- 4.7, 9.8		2.9, 6.3, 6.3
GHB	-4.5, 5.0, -8.3	-8.1, -5.9, -	-2.4, 1.6, -	3.4, 7.0, -5.9
FHB	3.2, 3.5, -4.6	6.6, -3.0, 5.8	-6.7, 6.5, -9.6	-4.7, 7.0, -8.1
NAQ	4.3, 2.1, -2.2	-3.8, -3.0, -3.3	-7.5, -6.5, -6.4	-9.2, 10.5, -5.3

Table 3. Half-amplitude latitudinal and longitudinal falloff distances between adjacent station pairs for the MPE occurring near 2105 UT on 8 May 2016 in Antarctica and Greenland, respectively.

BAS LPM	Greenland	BAS LPM – Greenland Conjugate
M81 – M79 106 km	GHB – FHB 204 km	M81 – FHB 446 km
M81 – M79 192 km		M79 – FHB 262 km



970

971

972

973 Figure 1. Maps showing the location of ground magnetometer stations used for this study. a)
 974 Map of Arctic Canada and Greenland, showing stations in the northern hemisphere (diamonds)
 975 and the conjugate mapped locations of southern hemisphere stations (green circles). b) Map of
 976 Antarctica, showing stations in the southern hemisphere (diamonds, squares, and red circle) and
 977 the conjugate mapped locations of northern hemisphere stations (triangles). Solid lines show
 978 corrected geomagnetic coordinates.

979

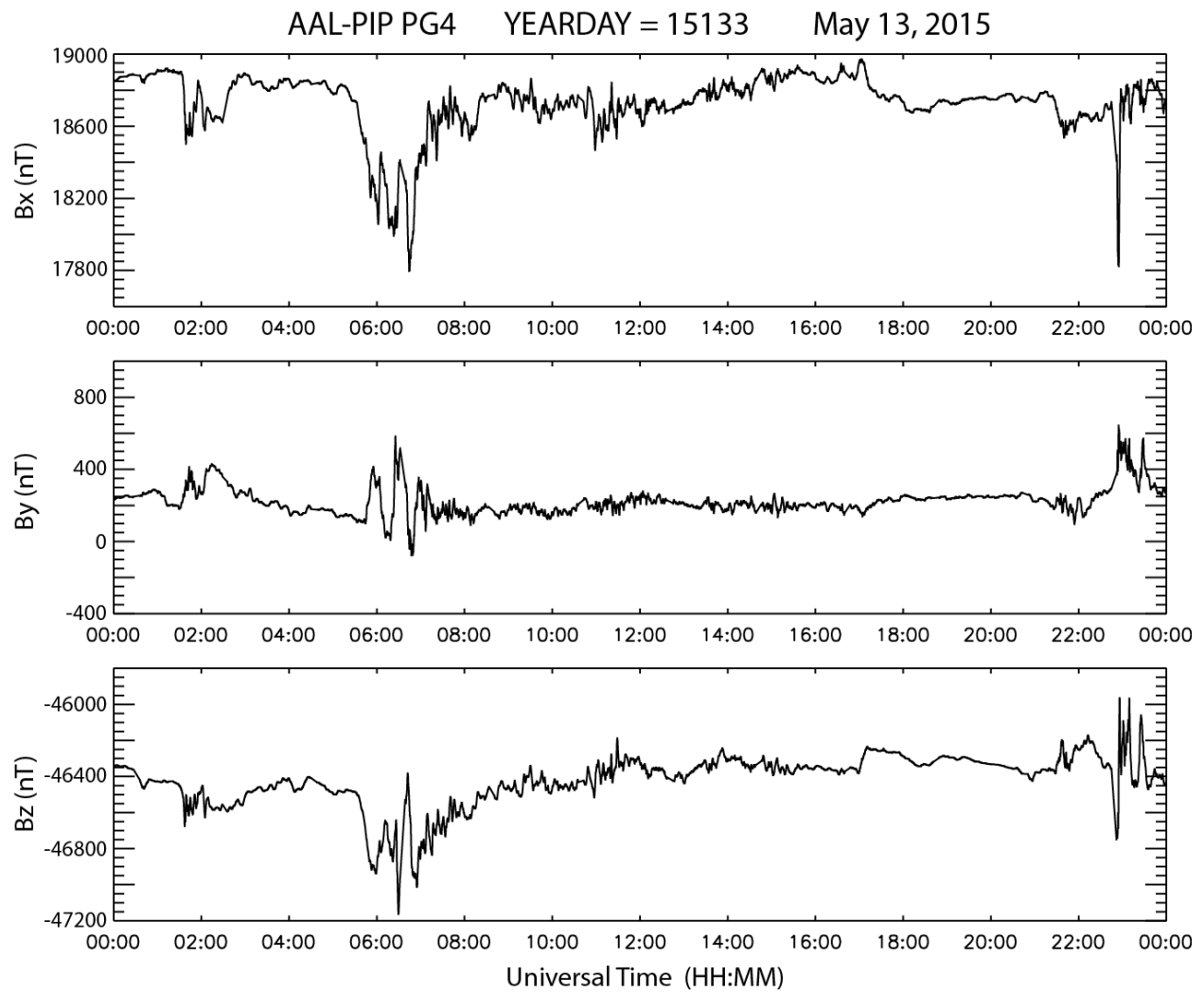


Figure 2. Daily magnetogram from AAL-PIP PG4 on May 13, 2015 with uniform vertical scale increments. The data are shown in local magnetic coordinates: B_x is northward, B_y eastward, and B_z vertically downward.

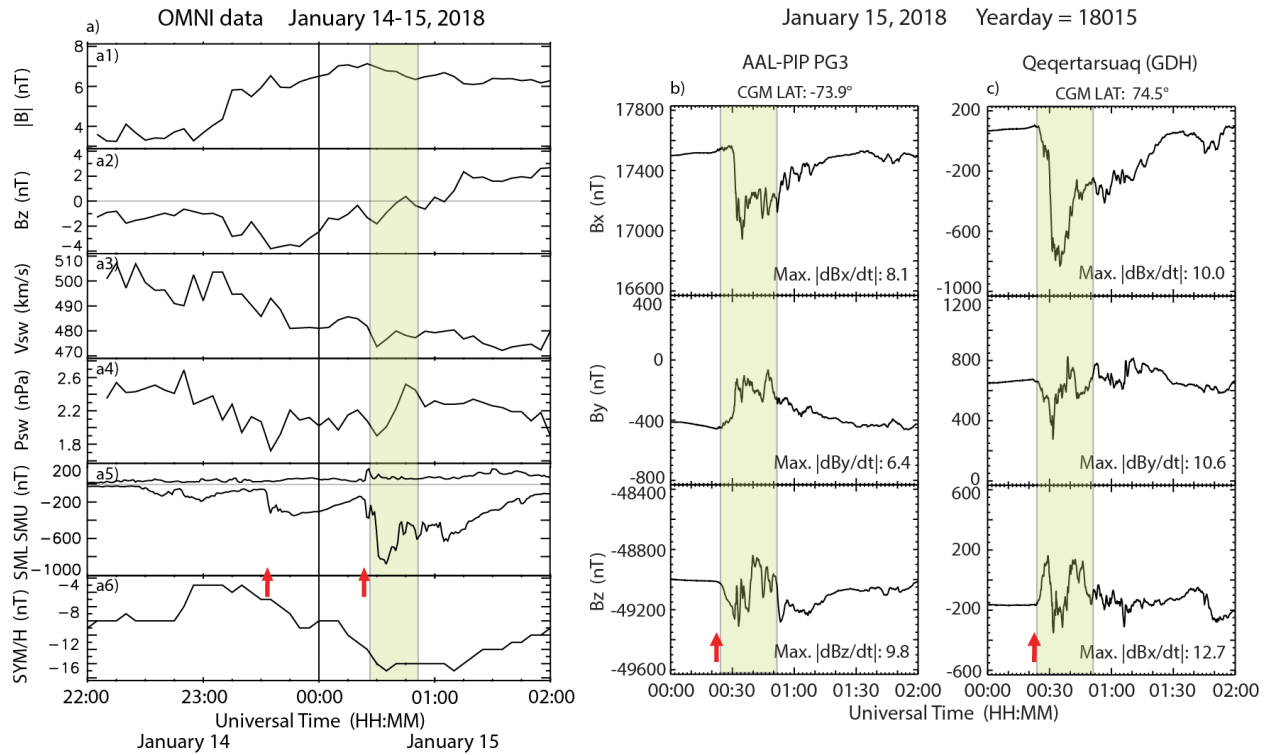


Figure 3. Panel a shows OMNI data that provide the interplanetary and magnetospheric context for the MPE event on January 15, 2018. Panels a1 and a2 show the magnitude $|B|$ and north-south component B_z of the interplanetary magnetic field (IMF), respectively. Panel a3 shows the solar wind flow speed, V_{sw} , and panel a4 shows the solar wind dynamic pressure, N_{sw} . Panel a5 shows the SuperMAG SML and SMU indices, and panel a6 shows the SYM/H index. Panels b and c show two-hour excerpts of magnetograms from AAL-PIP PG3, Antarctica, and Qeqertarsuaq (GDH), Greenland, respectively. The shaded region in each panel, from 0024 to 0052 UT, highlights the large magnetic perturbation observed at both stations, and the red arrows indicates the time of the closest prior substorm onsets.

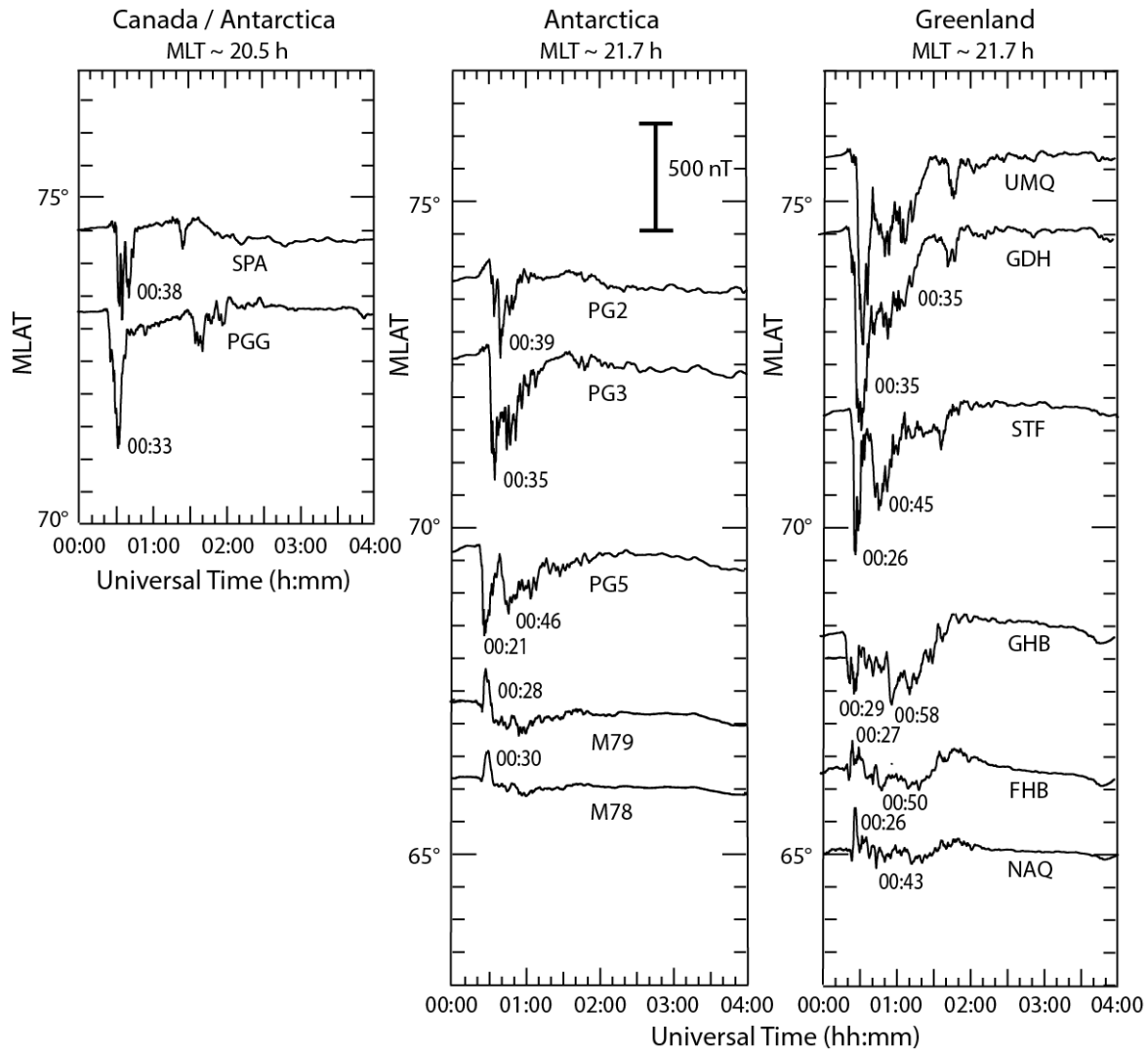


Figure 4. Four-hour excerpts of Bx component (north-south) magnetograms for January 15, 2018 from a) SPA and PGG, b) PG2, PG3, PG5, M79, and M78, and c) UMQ, GDH, STF, GHB, FHB, and NAQ), arranged vertically in order of magnetic latitude and horizontally in order of magnetic local time / magnetic longitude. At each station, the time of maximum $|\Delta B_x|$ perturbations is shown.

January 15, 2018 18015 ~ 00:35 UT

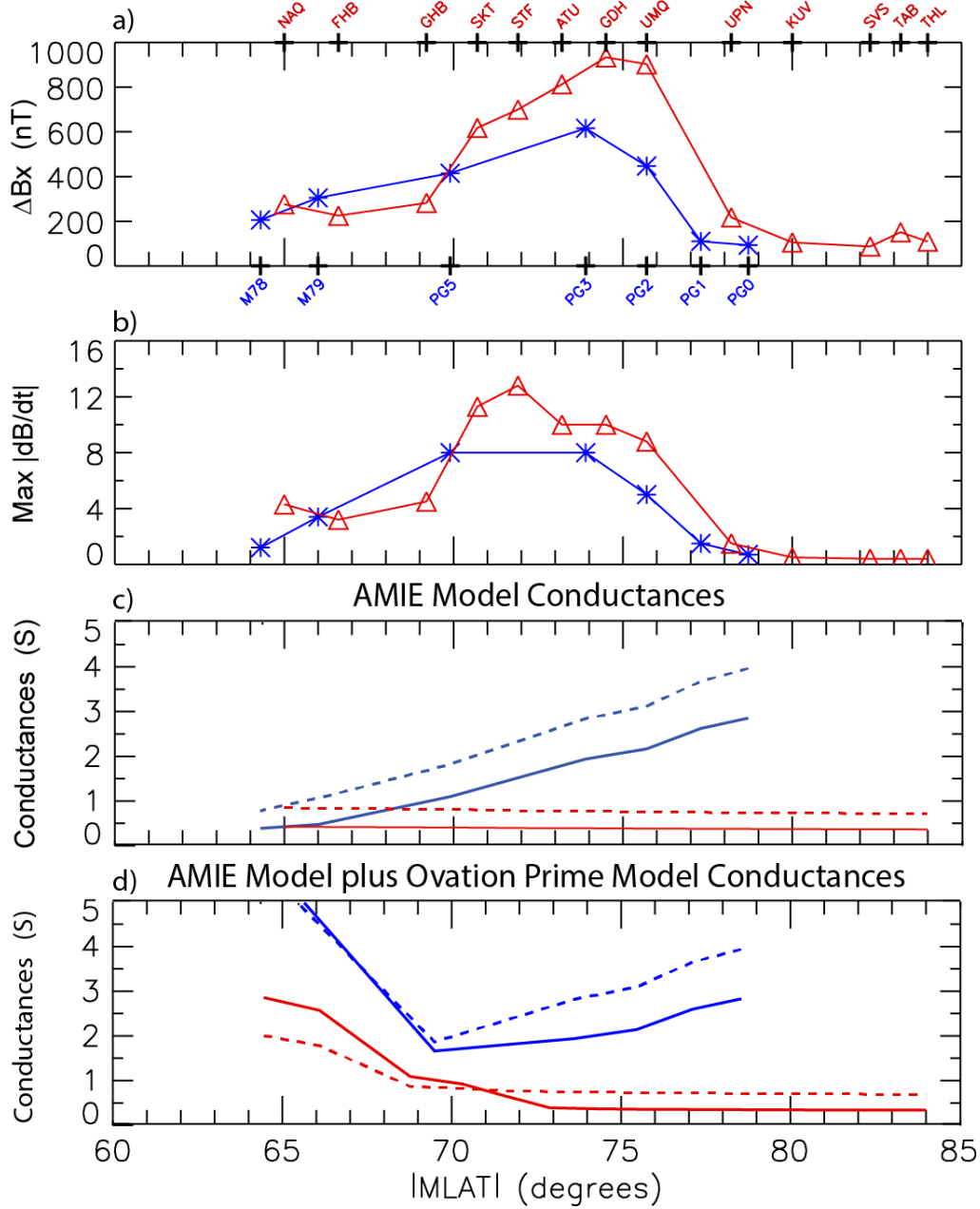


Figure 5. Plots of the perturbation amplitude ΔB_x (panel a), the maximum derivative in any component (panel b), and two models of the ionospheric Pedersen and Hall conductances (panels c and d), as a function of magnetic latitude, observed at every available station in the West Greenland Coastal Array (red) and the AAL-PIP and BAS LPM arrays (blue) for the MPE at ~0035 UT January 15, 2018. Solid lines denote Pedersen conductances (Σ_P) and dashed lines Hall conductances (Σ_H).

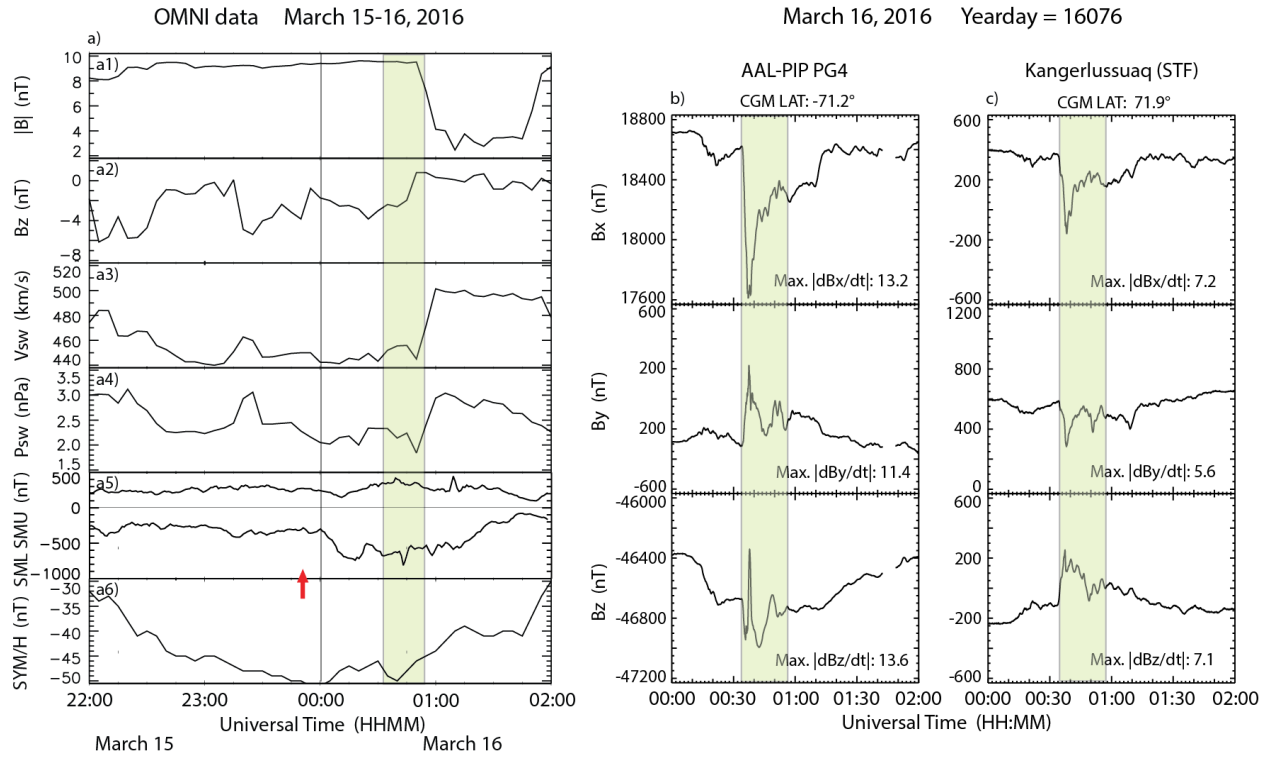


Figure 6. Panel a shows OMNI data for the MPE event on March 16, 2016, as in Figure 3. Panels b and c show two-hour excerpts of magnetograms from AAL-PIP PG4, Antarctica, and Kangerlussuaq (STF), Greenland, respectively. The shaded region in each panel, from 0034 to 0057 UT, highlights the large magnetic perturbation observed at both stations, and the red arrow indicates the time of the closest prior substorm onset.

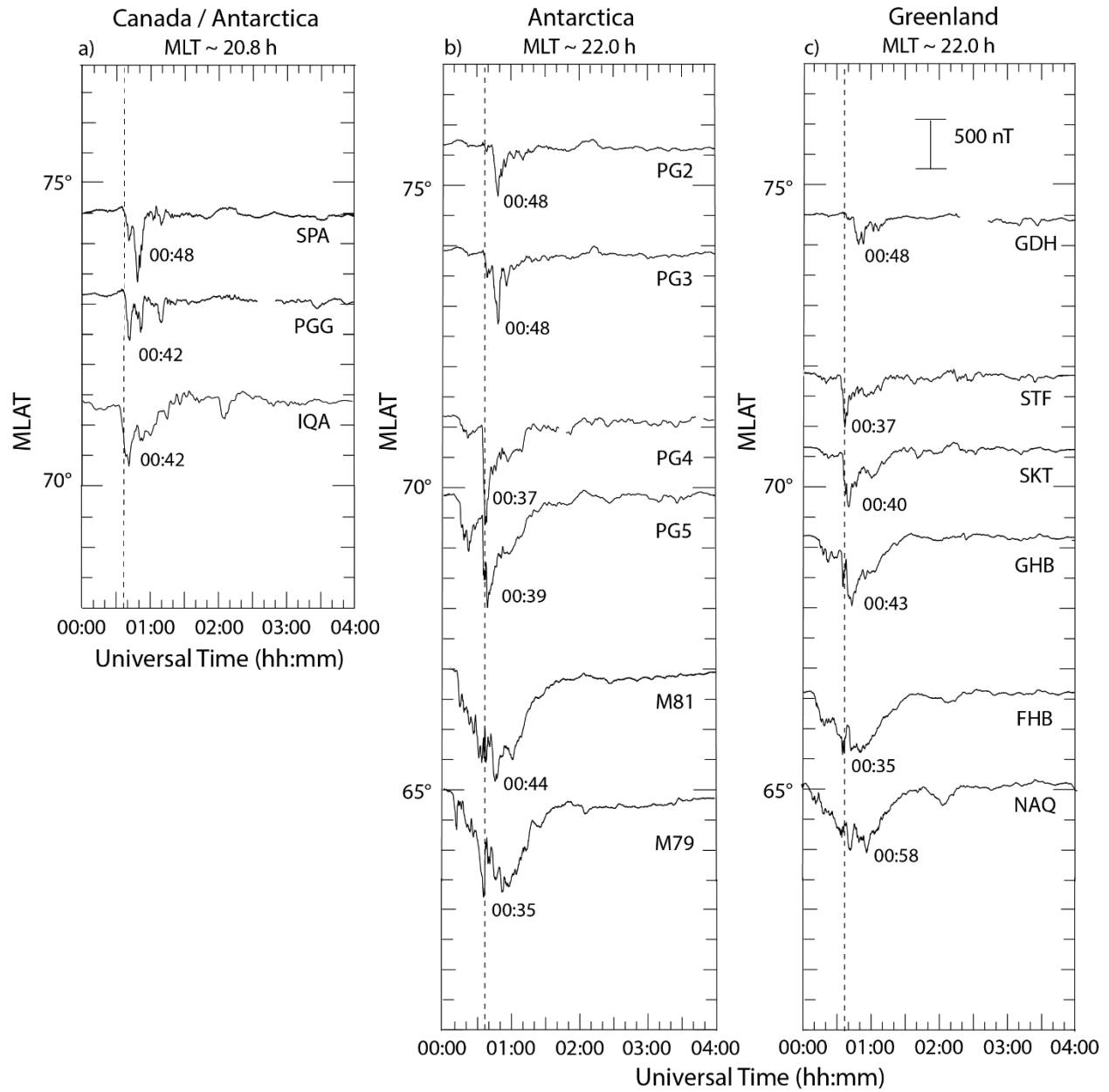


Figure 7. Four-hour excerpts of Bx component (north-south) magnetograms for March 16, 2016, as in Figure 4. a) SPA, PGG, and IQA, b) PG2, PG3, PG4, PG5, M81, and M79, and c) GDH, STF, SKT, GHB, FHB, and NAQ. At each station, the time of maximum $|\Delta B_x|$ perturbations is shown. The vertical dashed lines mark 00:37 UT, the time of minima in the Bx component at PG4, M84 (not shown), and STF.

March 16, 2016 16076 00:38 and 00:48 UT

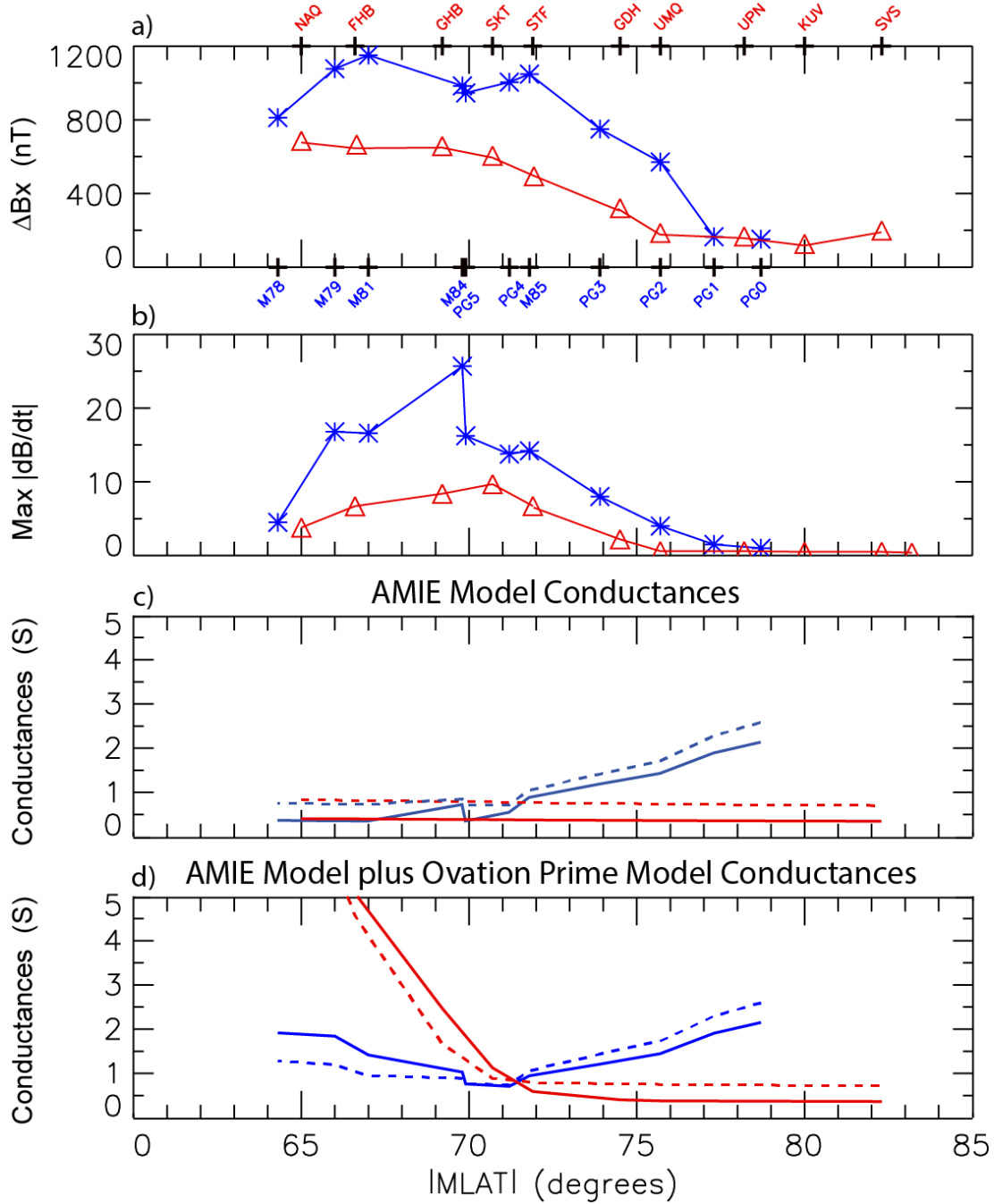


Figure 8. Plots of the perturbation amplitude ΔB_x (panel a), the maximum derivative in any component (panel b), and two models of the ionospheric Pedersen and Hall conductances (panels c and d), as a function of magnetic latitude as in Figure 5, for the MPEs near ~0040 UT March 16, 2016. Solid lines denote Pedersen conductances (Σ_P) and dashed lines Hall conductances (Σ_H).

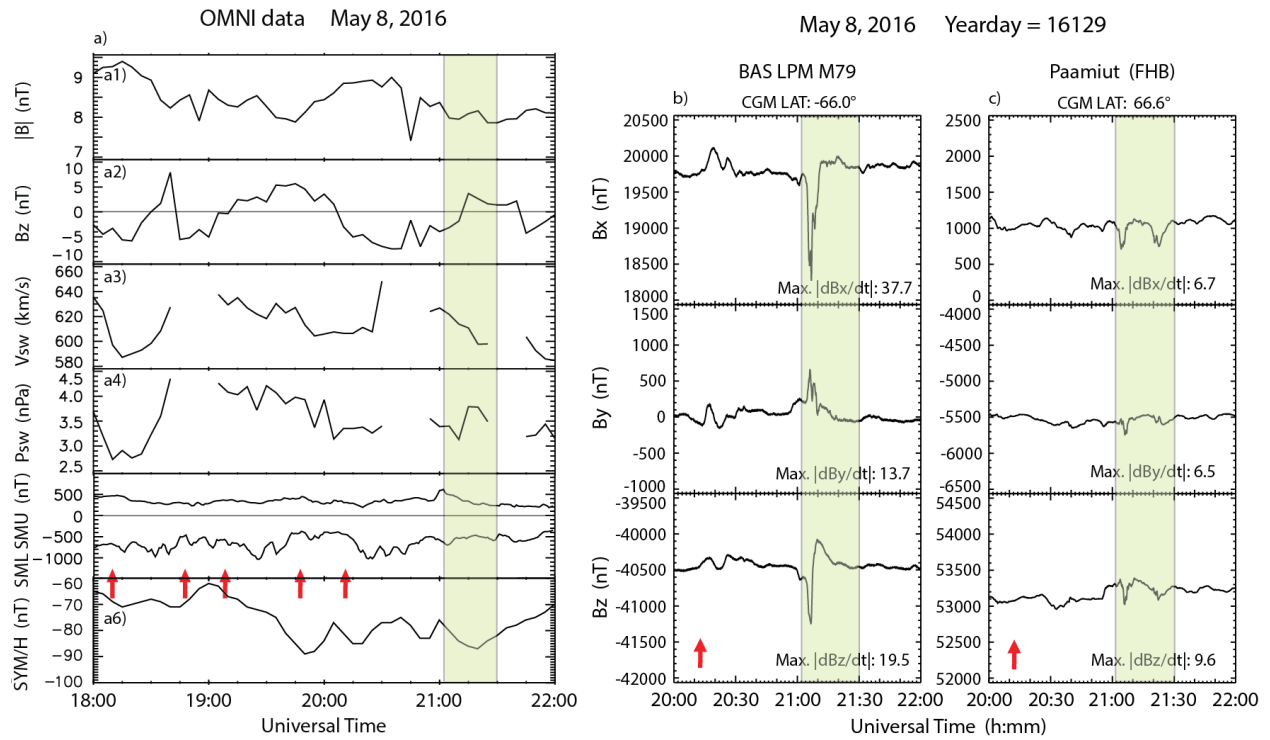


Figure 9. Panel a shows OMNI data for the MPE event on May 8, 2016, as in Figure 3. Panels b and c show two-hour excerpts of magnetograms from BAS LPM M79, Antarctica, and Paamiut (FHB), Greenland, respectively. The shaded region in each panel, from 2102 to 2130 UT, highlights the large magnetic perturbations observed at both stations, and the red arrows indicate the times of the closest prior substorm onsets.

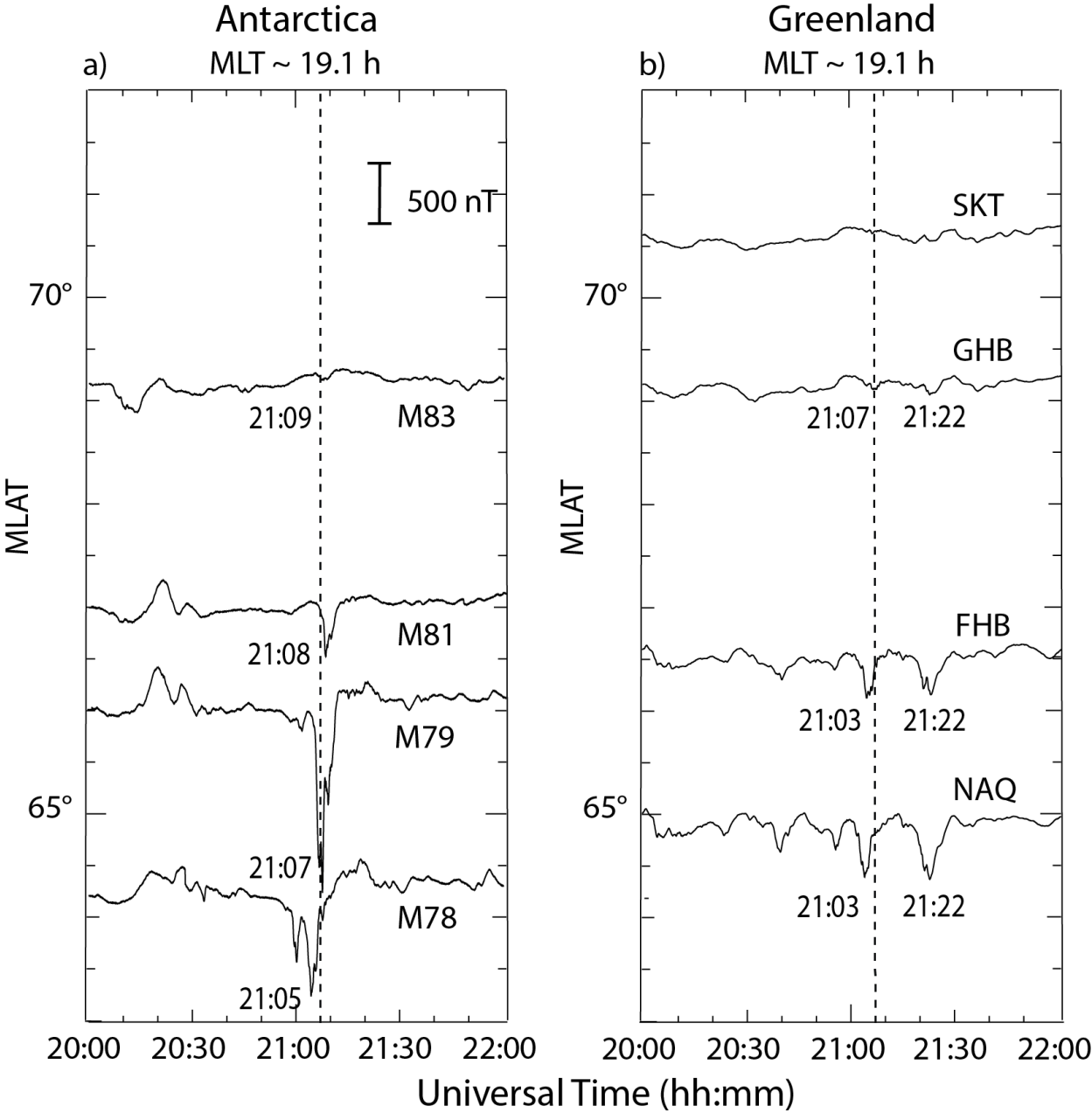


Figure 10. Two-hour excerpts of Bx component (north-south) magnetograms for May 8, 2016, as in Figure 4. a) M83, M81, M79, and M78, and b) SKT, GHB, FHB, and NAQ. At each station, the time of maximum $|\Delta B_x|$ perturbations is shown. The vertical dashed lines mark 21:07 UT, the time of minima in the Bx component at GHB and M79.

May 8, 2016 16129 ~21:08 UT

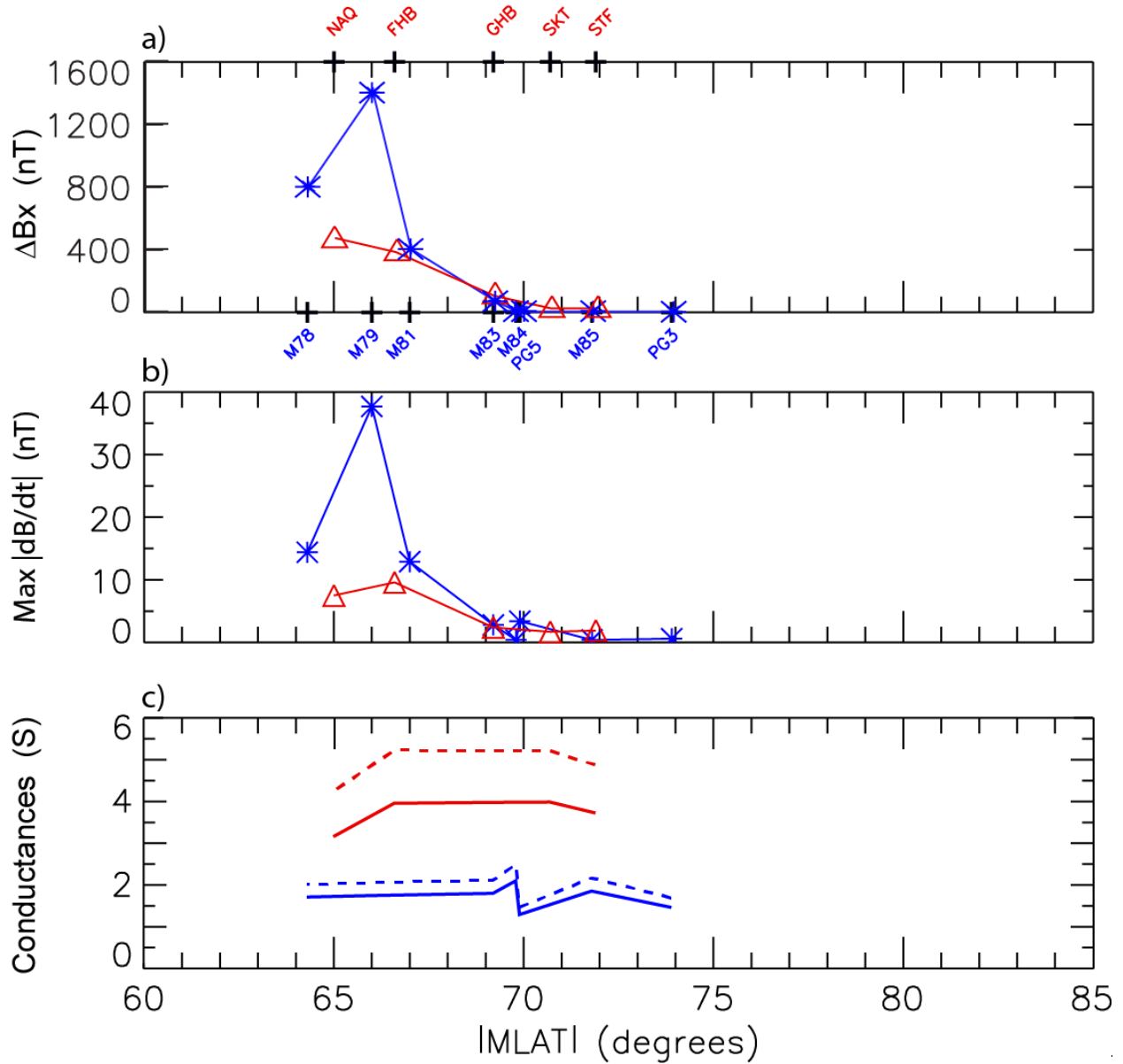
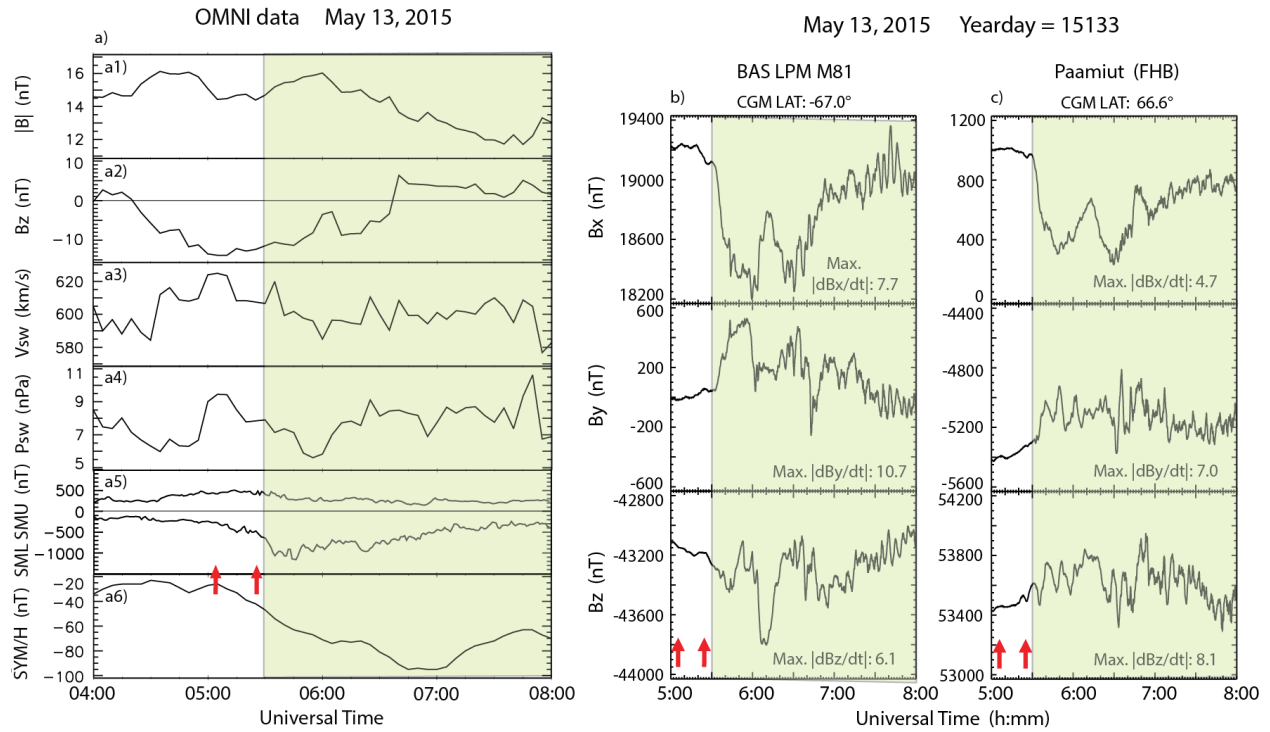


Figure 11. Plots of the perturbation amplitude ΔB_x (panel a), the maximum derivative in any component (panel b), and a model of the ionospheric Pedersen and Hall conductances (panel c), as a function of magnetic latitude as in Figure 5, for the MPE at ~2108 UT May 8, 2016. Solid lines denote Pedersen conductances (Σ_P) and dashed lines Hall conductances (Σ_H).

1063 C



1064
1065
1066
1067
1068
1069
1070
1071

Figure 12. Panel a shows OMNI data for the MPE event on May 3, 2015, as in Figure 3. Panels b and c show three-hour excerpts of magnetograms from BAS LPM M81, Antarctica, and Paamiut (FHB), Greenland, respectively. The shaded region in each panel, from 0530 to 0800 UT, highlights the large magnetic perturbations observed at both stations, and the red arrows indicate the times of the closest prior substorm onsets.

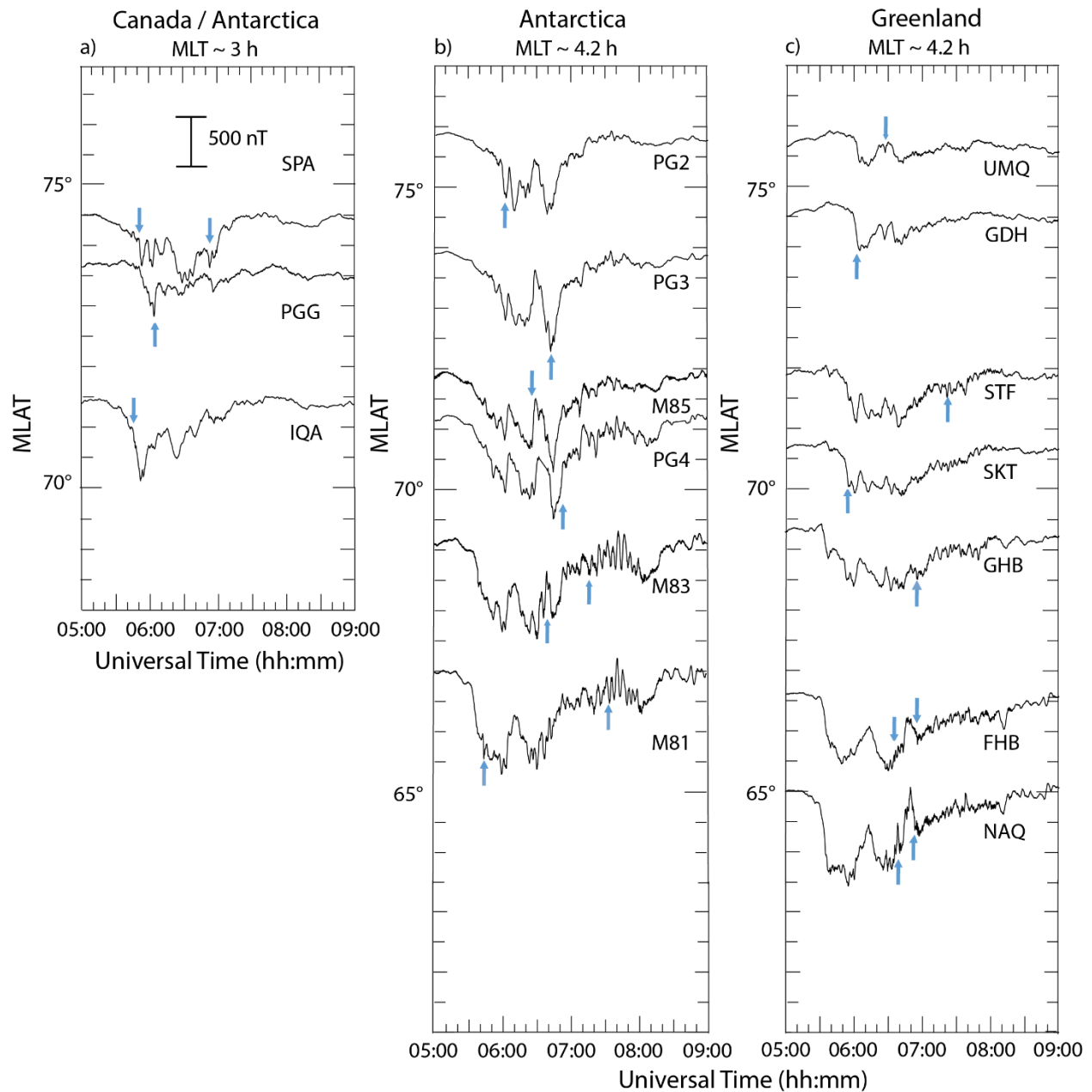


Figure 13. Four-hour excerpts of Bx component (north-south) magnetograms for May 13, 2015, as in Figure 4. a) SPA, PGG, and IQA, b) PG2, M85, PG4, M83, and M81, and c) UMQ, STF, SKT, GHB, FHB, and NAQ. Blue arrows indicate the strongest MPEs at each station.

May 13, 2015 15133 05:30 - 08:00 UT

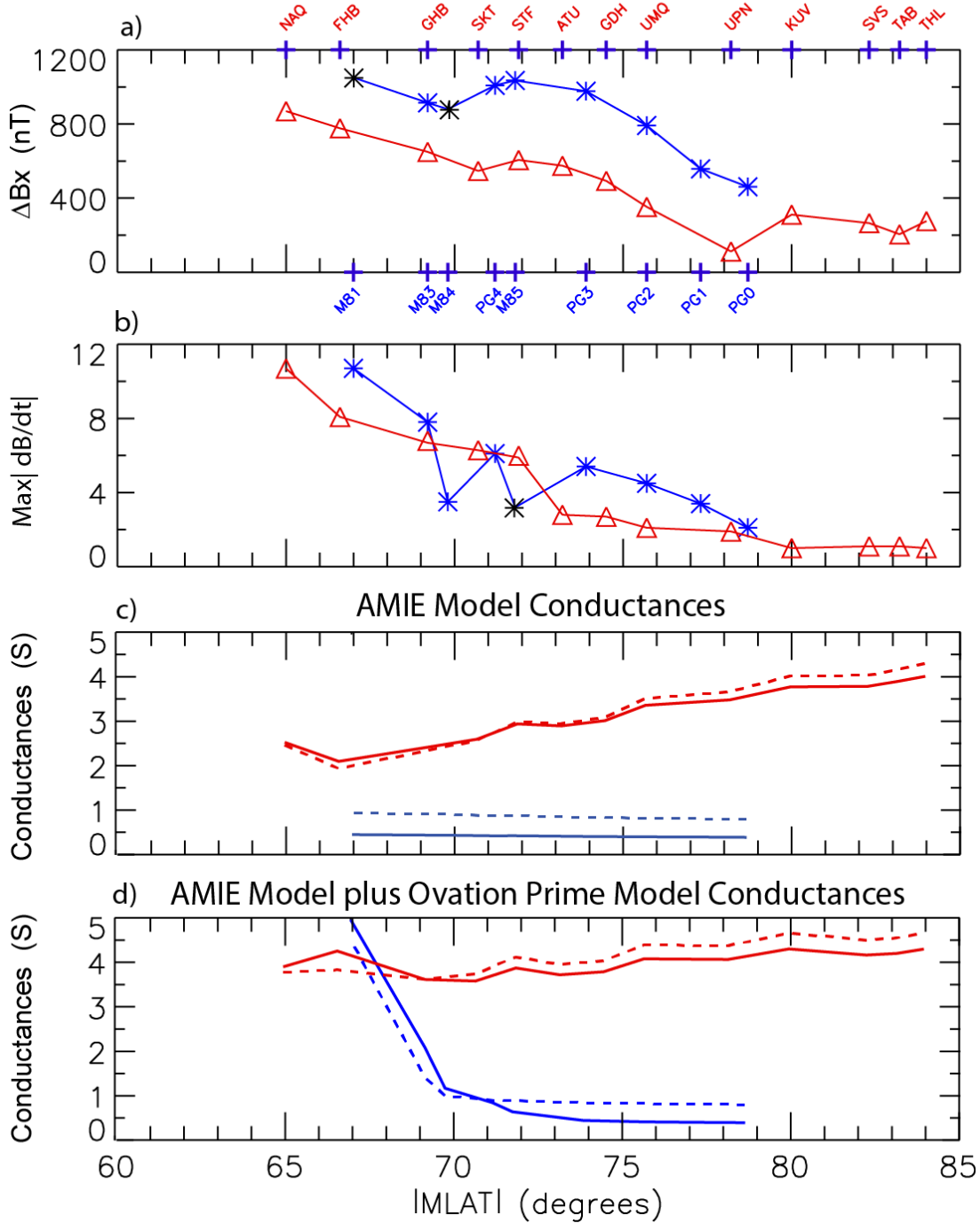


Figure 14. Plots of the perturbation amplitude ΔB_x (panel a), the maximum derivative in any component (panel b), and two models of the ionospheric Pedersen and Hall conductances (panels c and d), as a function of magnetic latitude as in Figure 5, for the MPEs from 0530 to 0800 UT May 13, 2015. Solid lines denote Pedersen conductances (Σ_P) and dashed lines Hall conductances (Σ_H).

Figure 1.

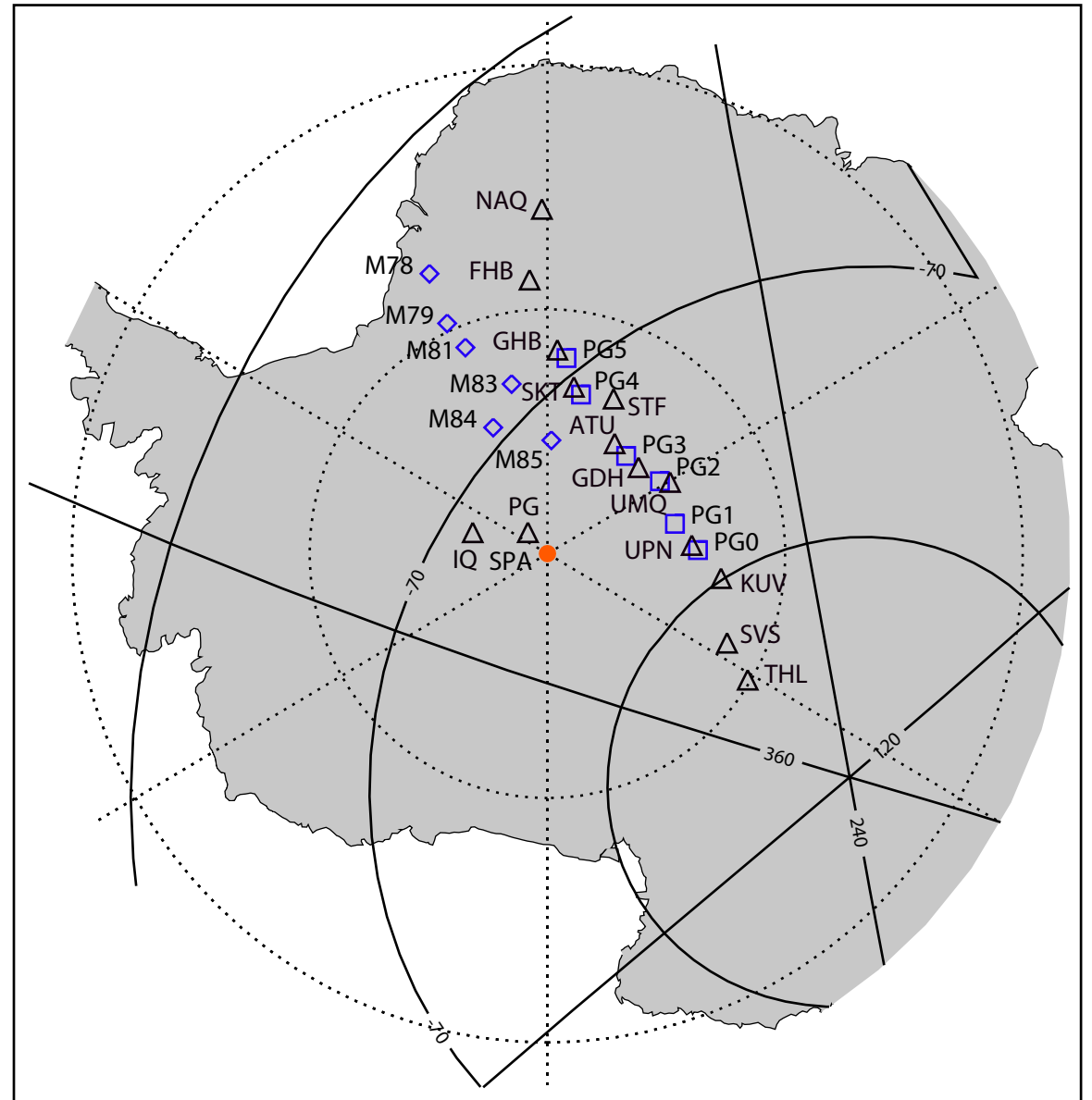
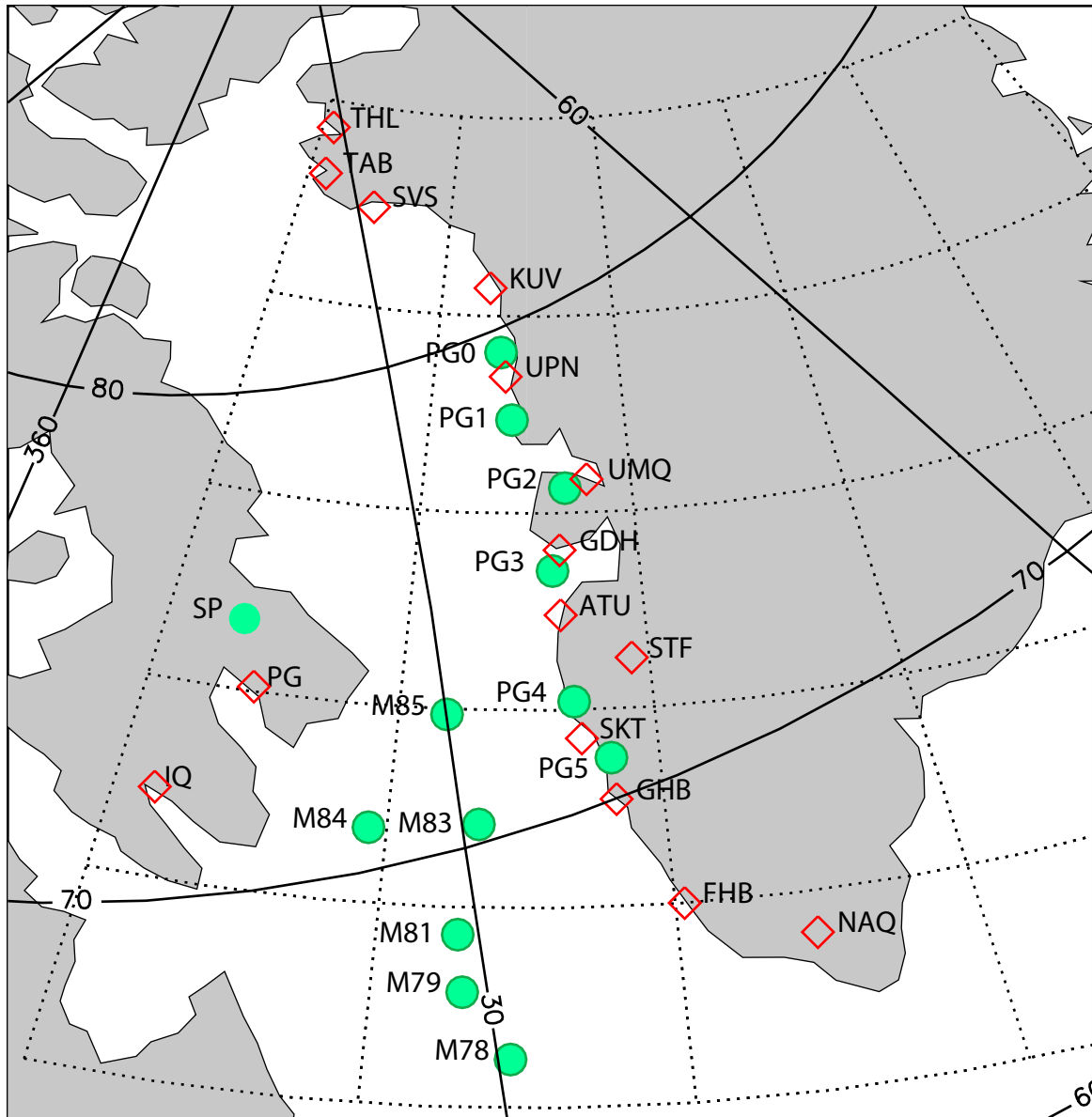


Figure 2.

AAL-PIP PG4

YEARDAY = 15133

May 13, 2015

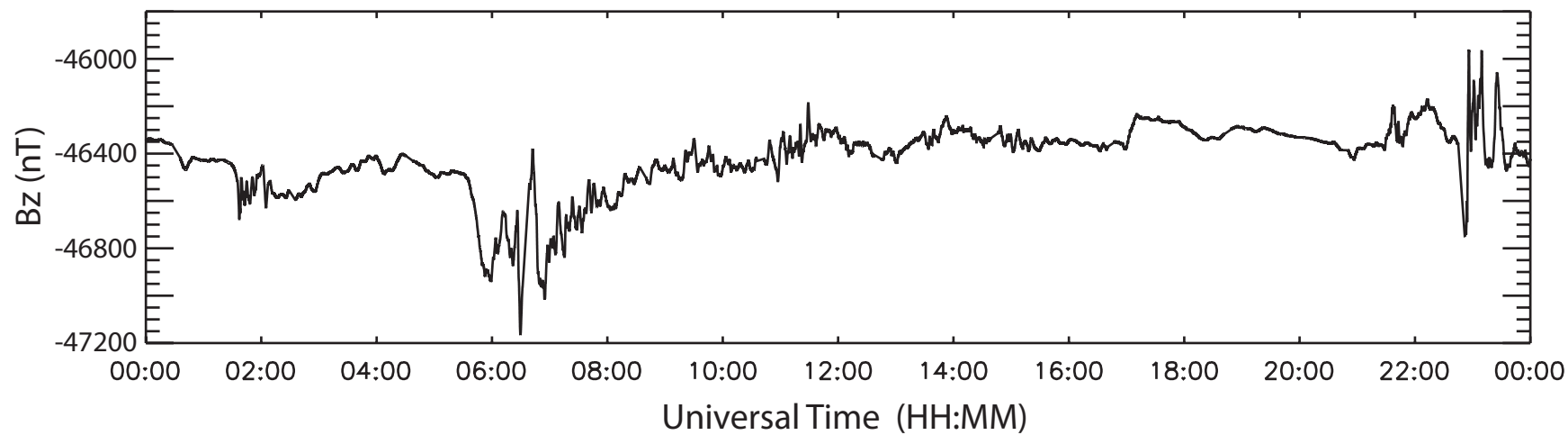
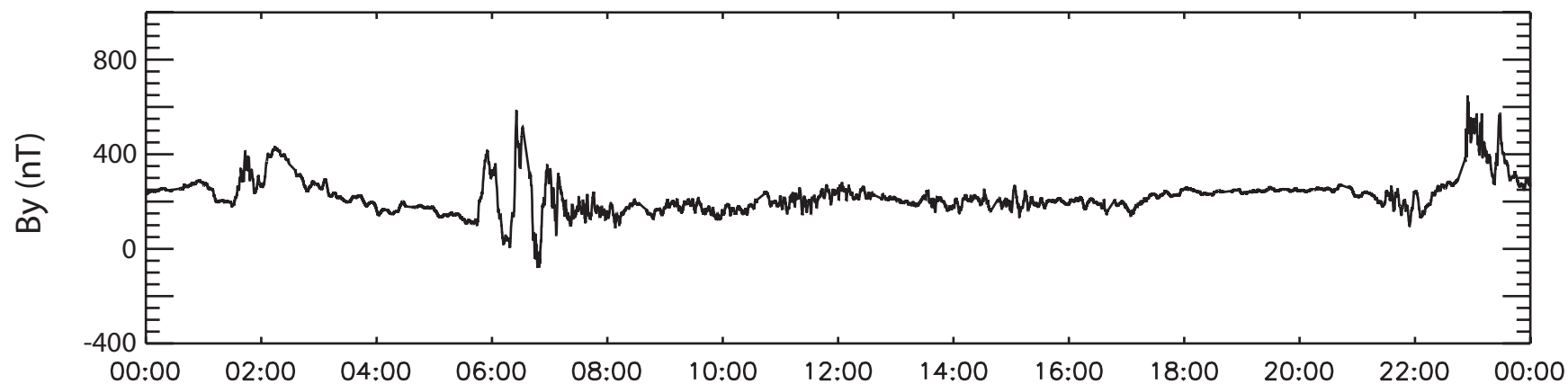
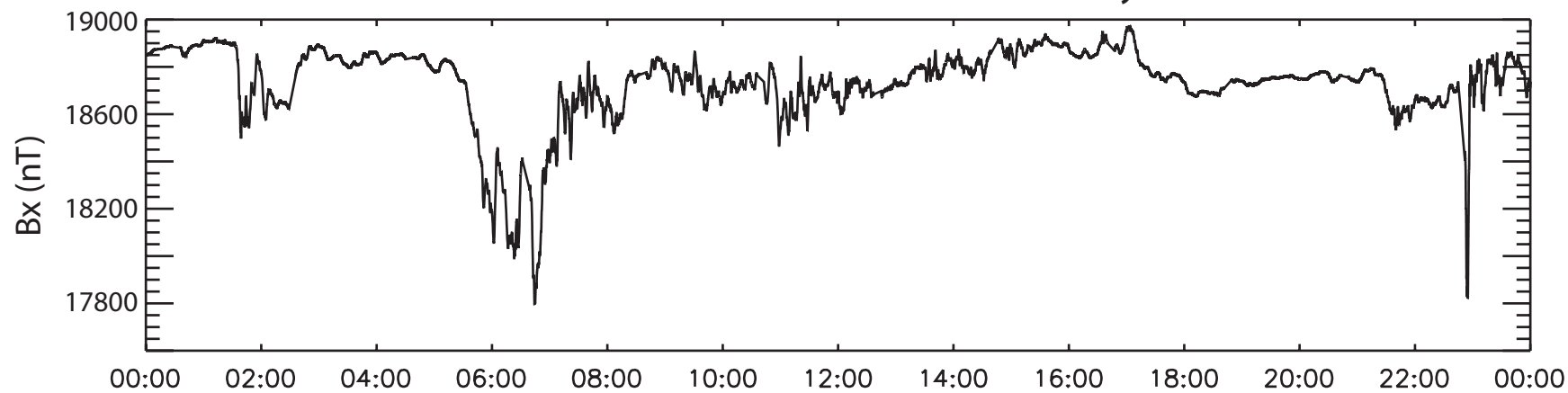
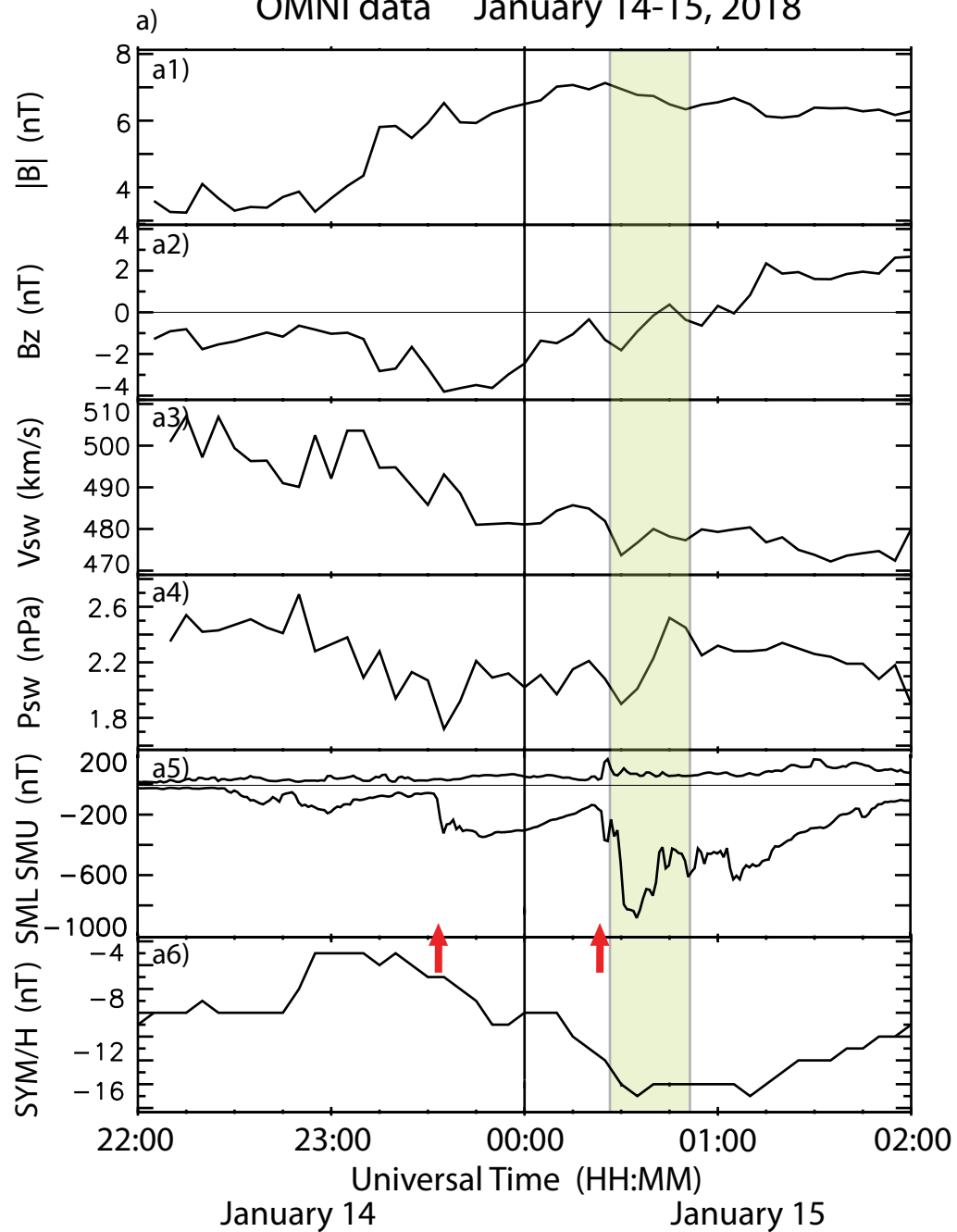


Figure 3.

OMNI data January 14-15, 2018



January 15, 2018 Yearday = 18015

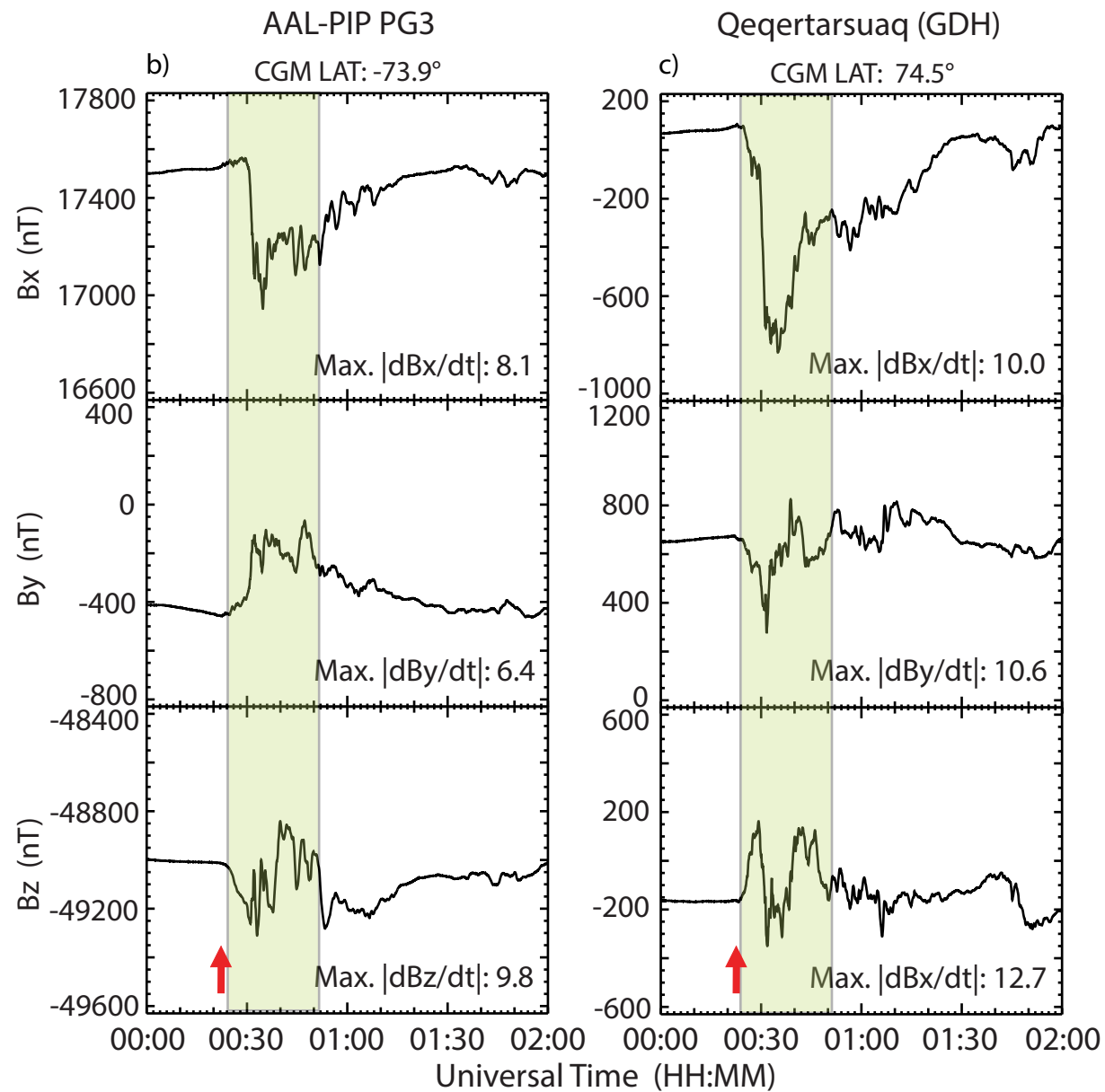
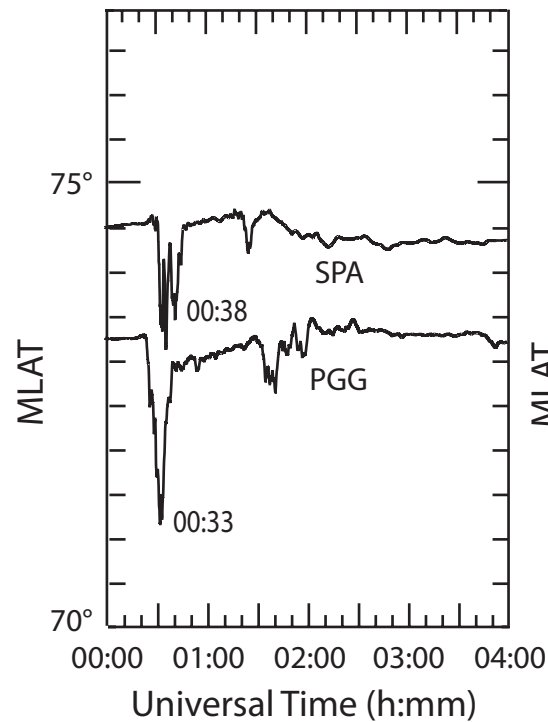


Figure 4.

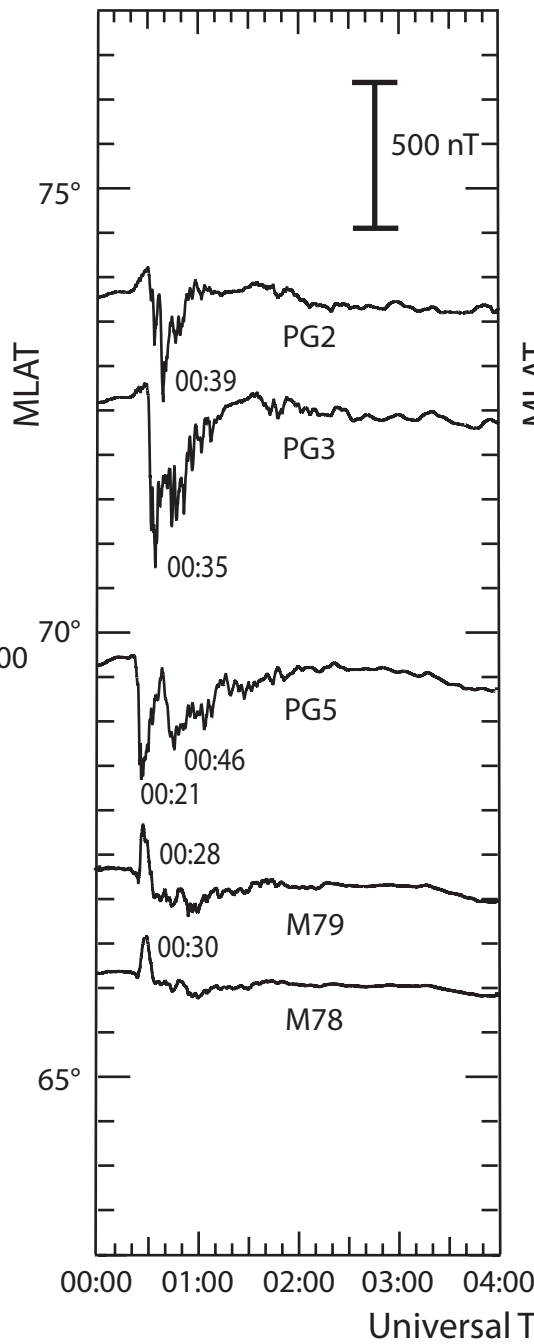
Canada / Antarctica

MLT ~ 20.5 h



Antarctica

MLT ~ 21.7 h



Greenland

MLT ~ 21.7 h

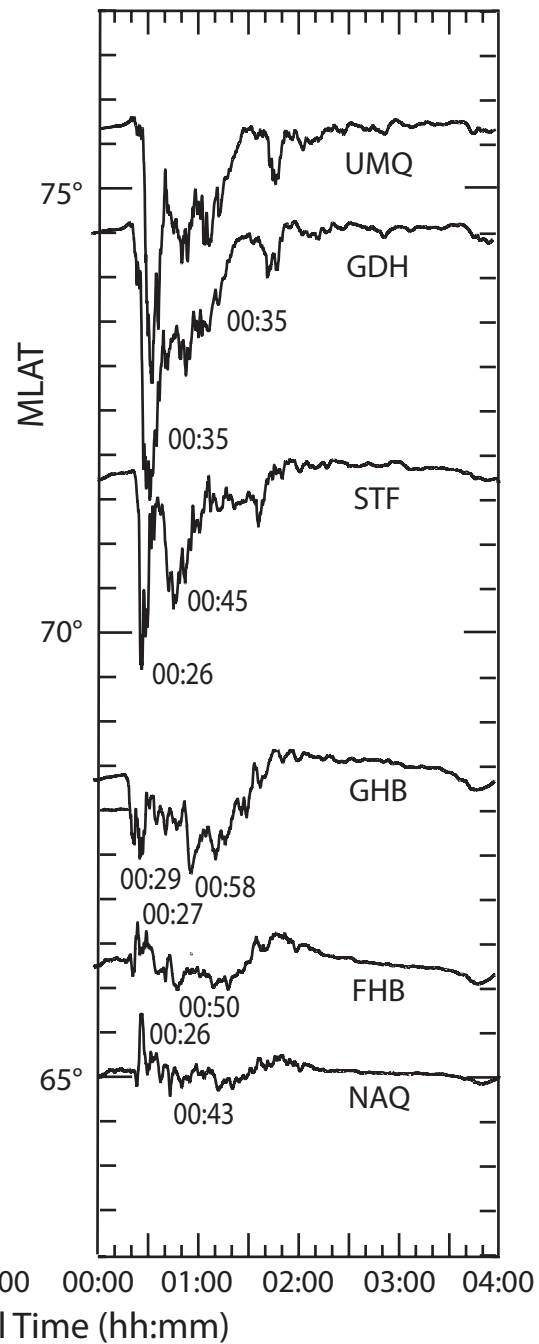


Figure 5.

January 15, 2018 18015 ~ 00:35 UT

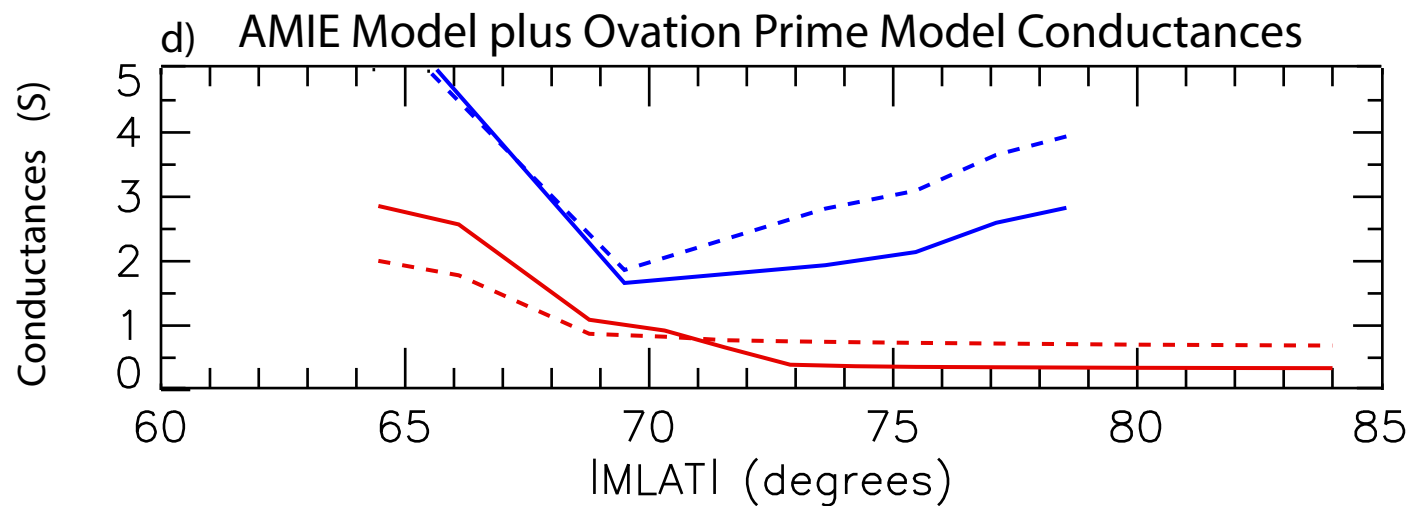
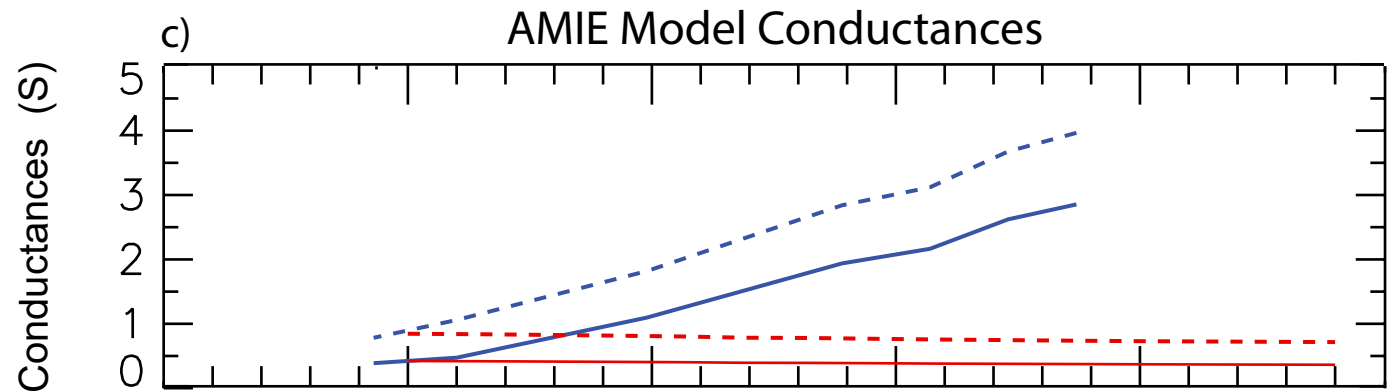
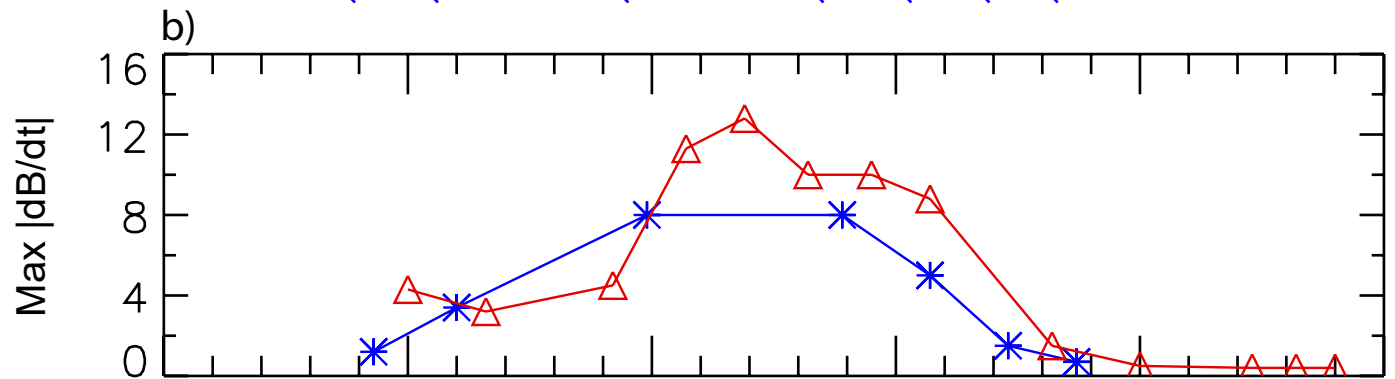
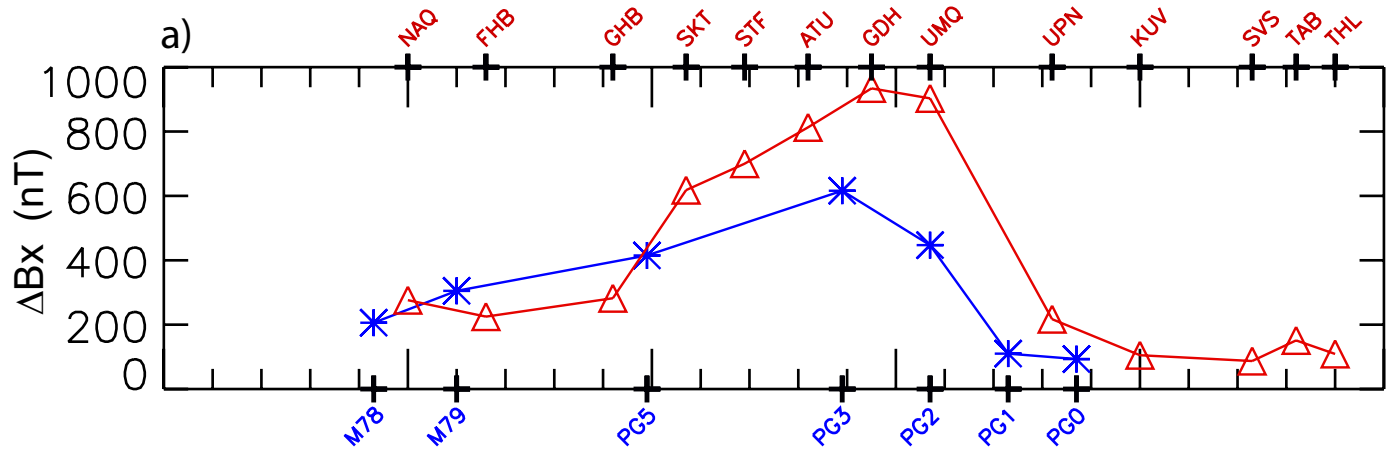
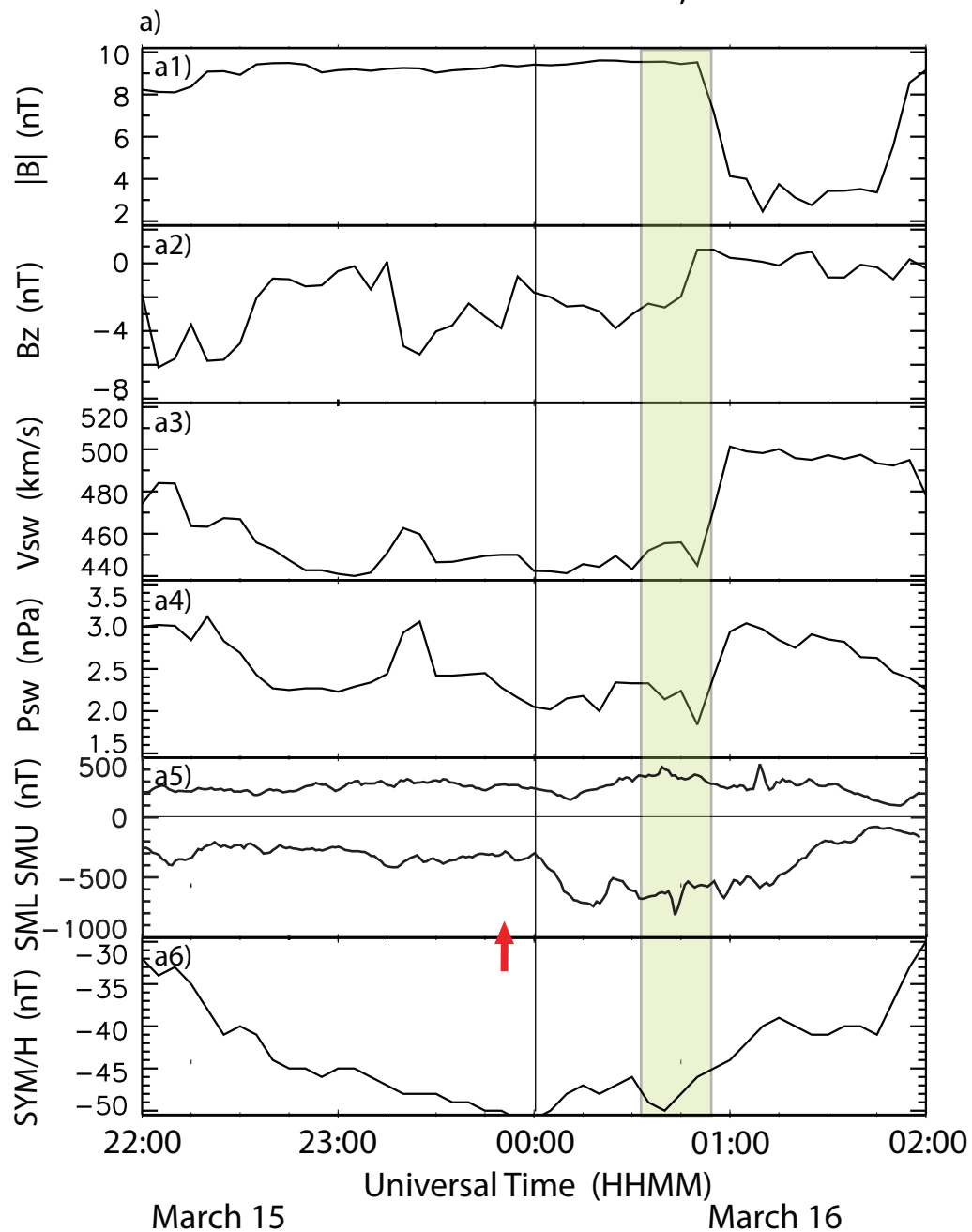


Figure 6.

OMNI data March 15-16, 2016



March 16, 2016 Yearday = 16076

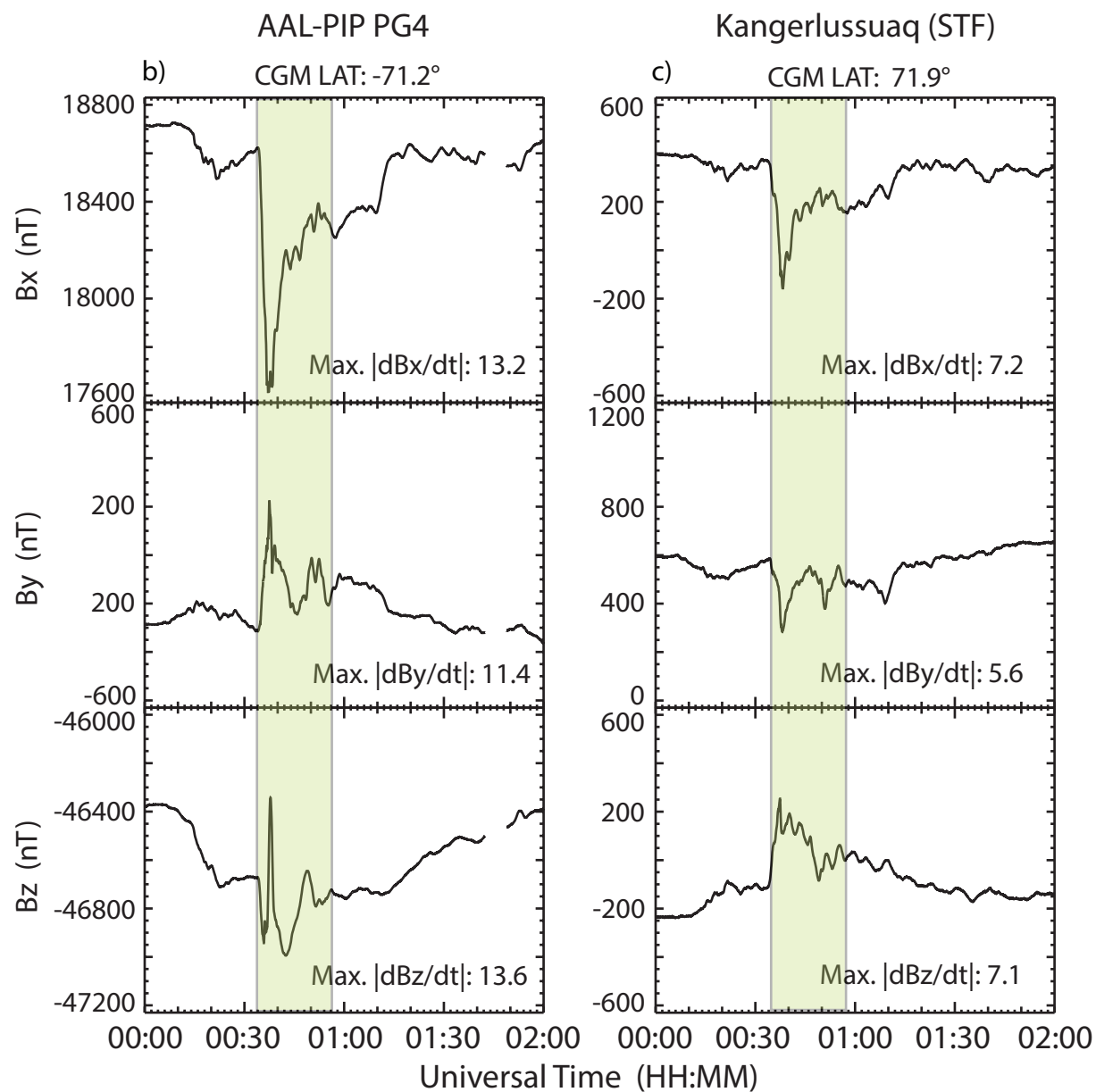
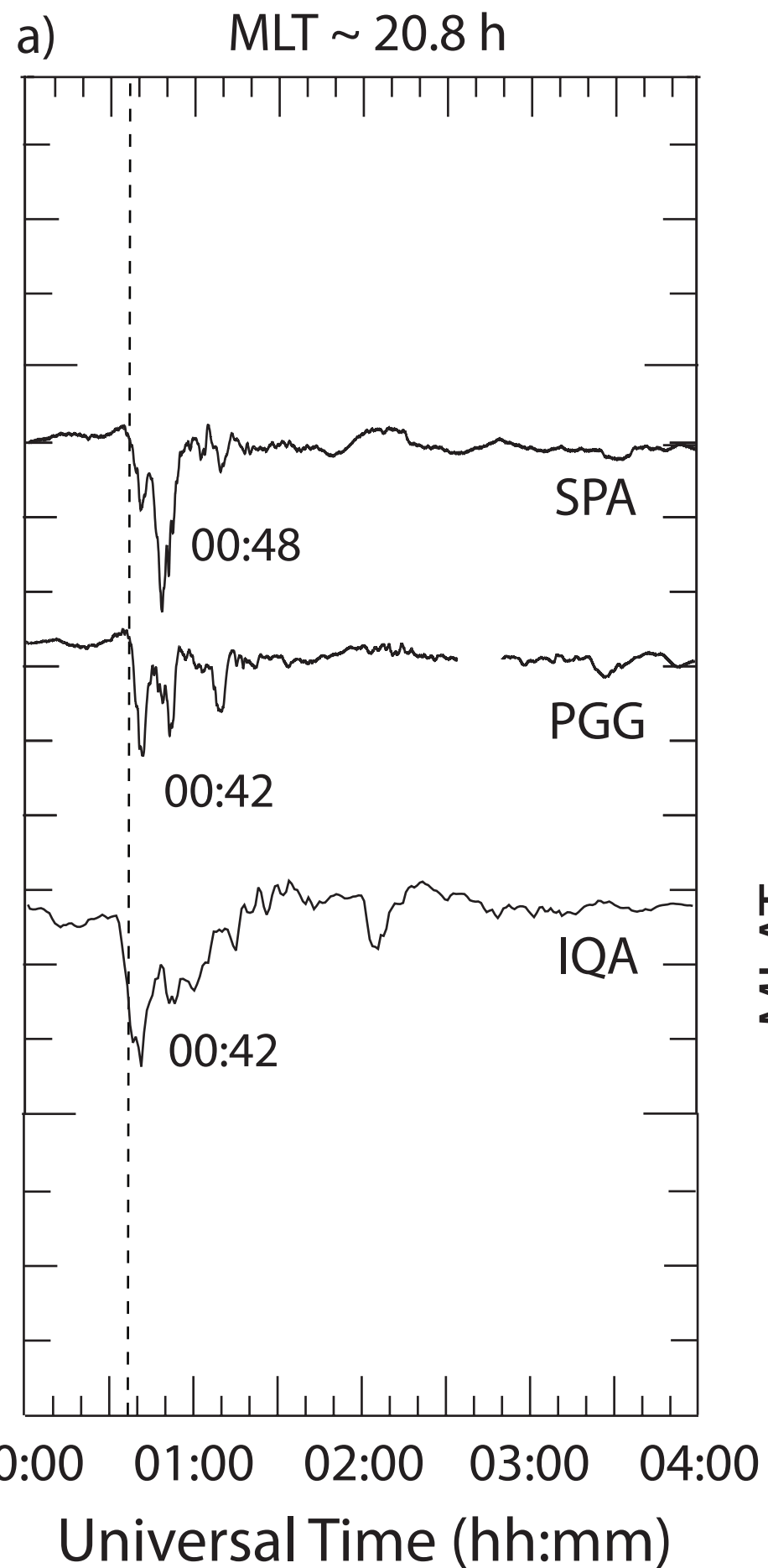
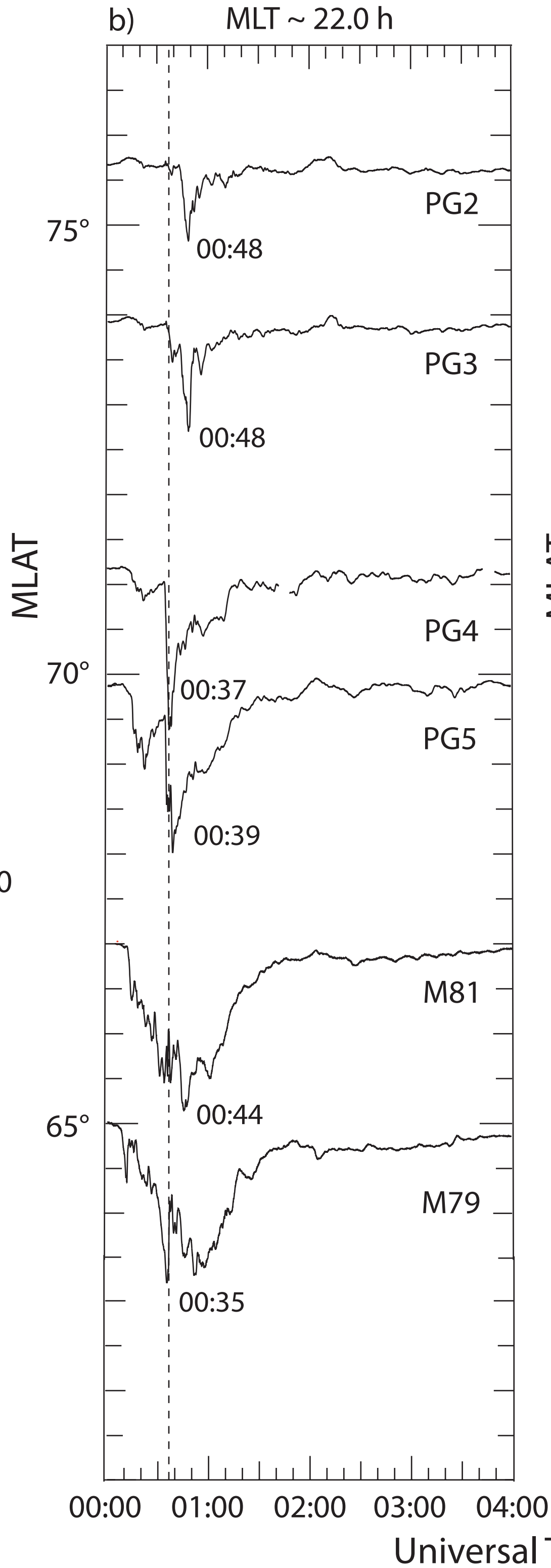


Figure 7.

Canada / Antarctica



Antarctica



Greenland

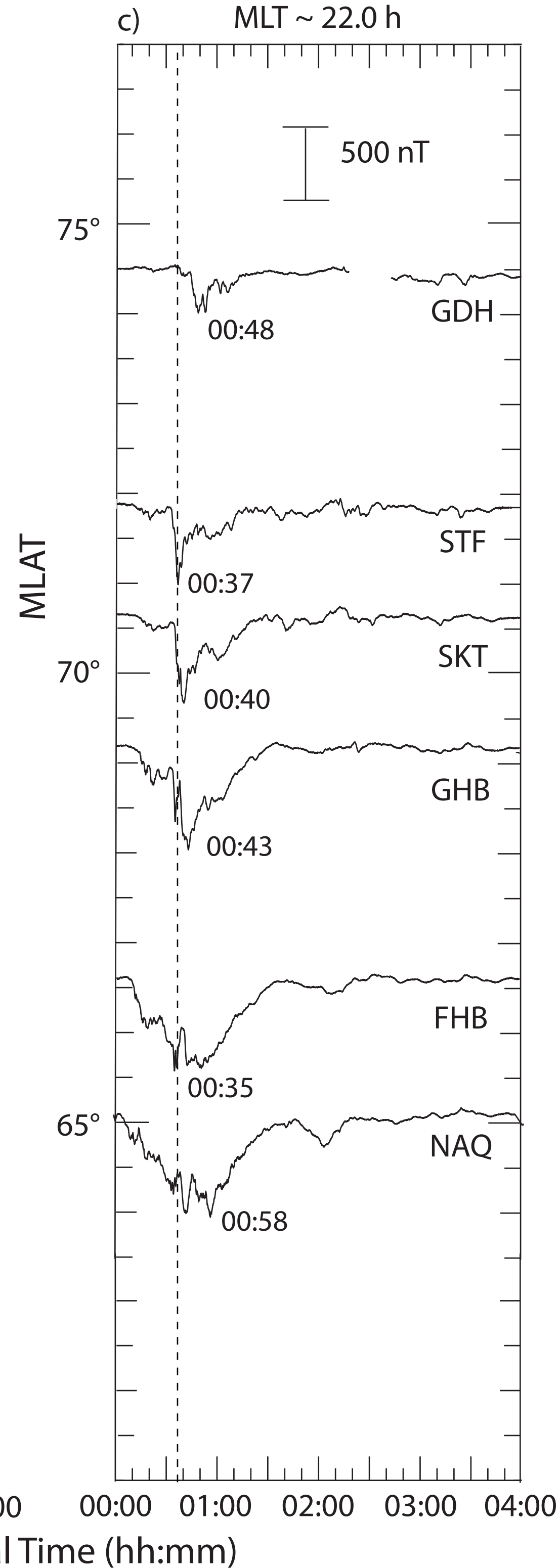


Figure 8.

March 16, 2016 16076 00:38 and 00:48 UT

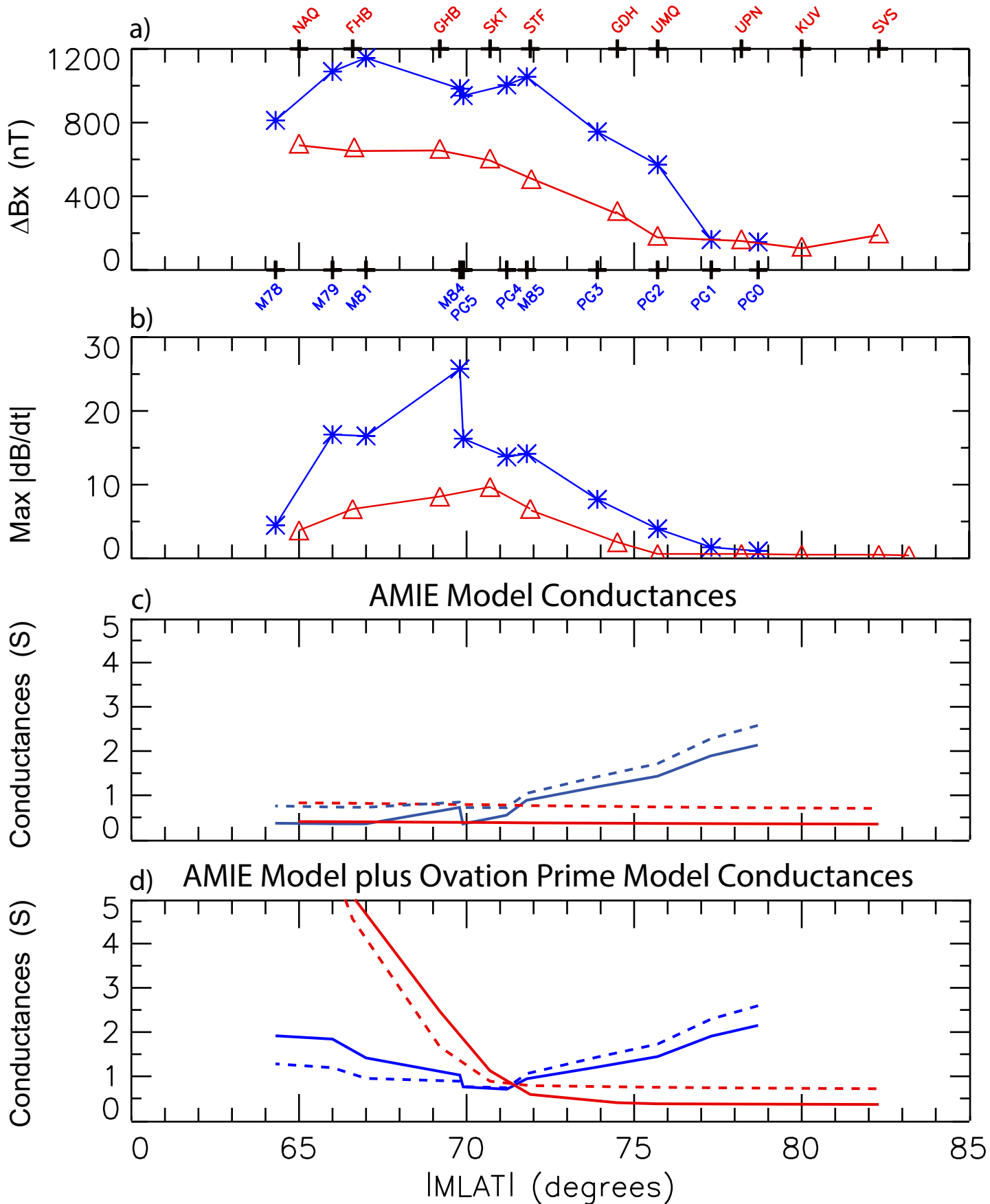
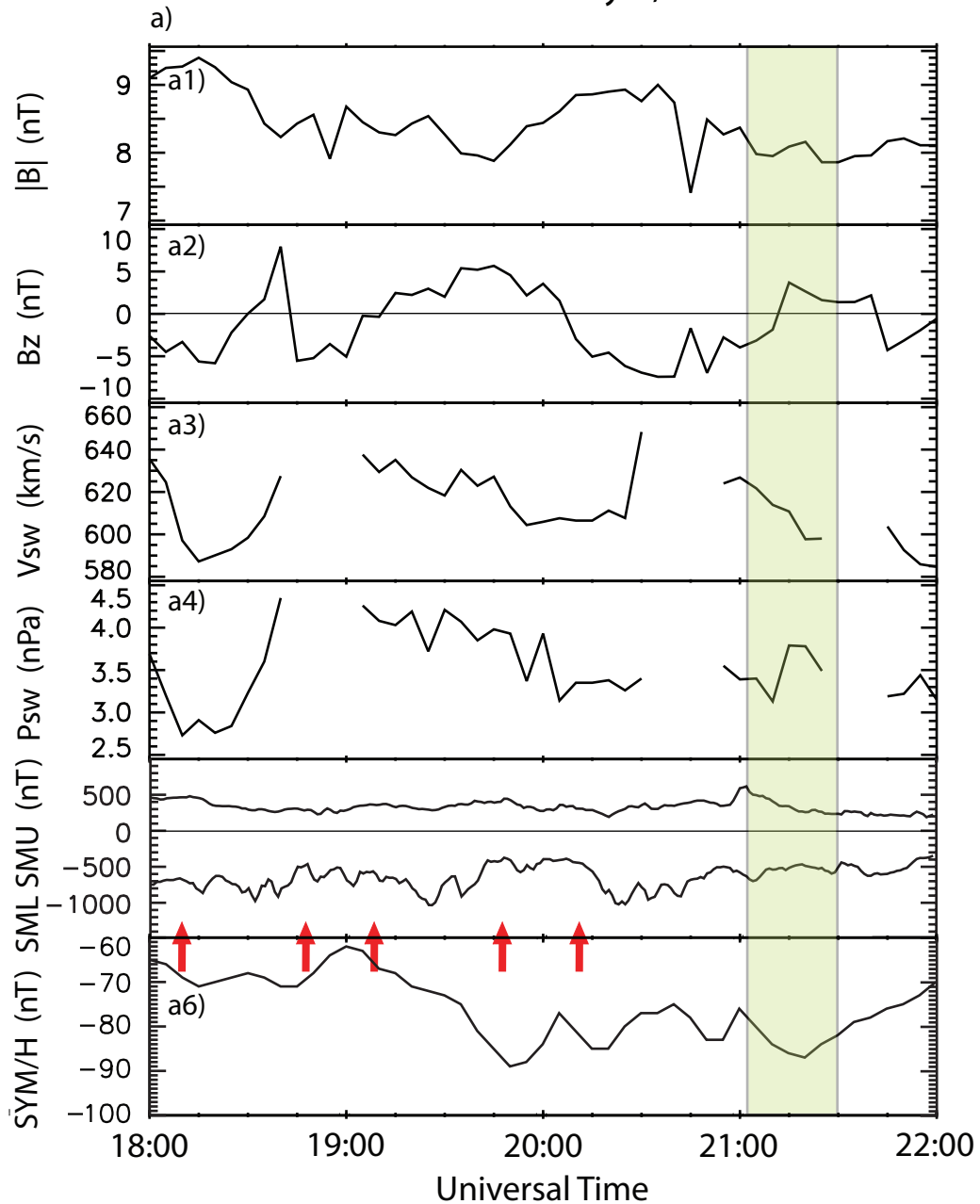


Figure 9.

OMNI data May 8, 2016



May 8, 2016

Yearday = 16129

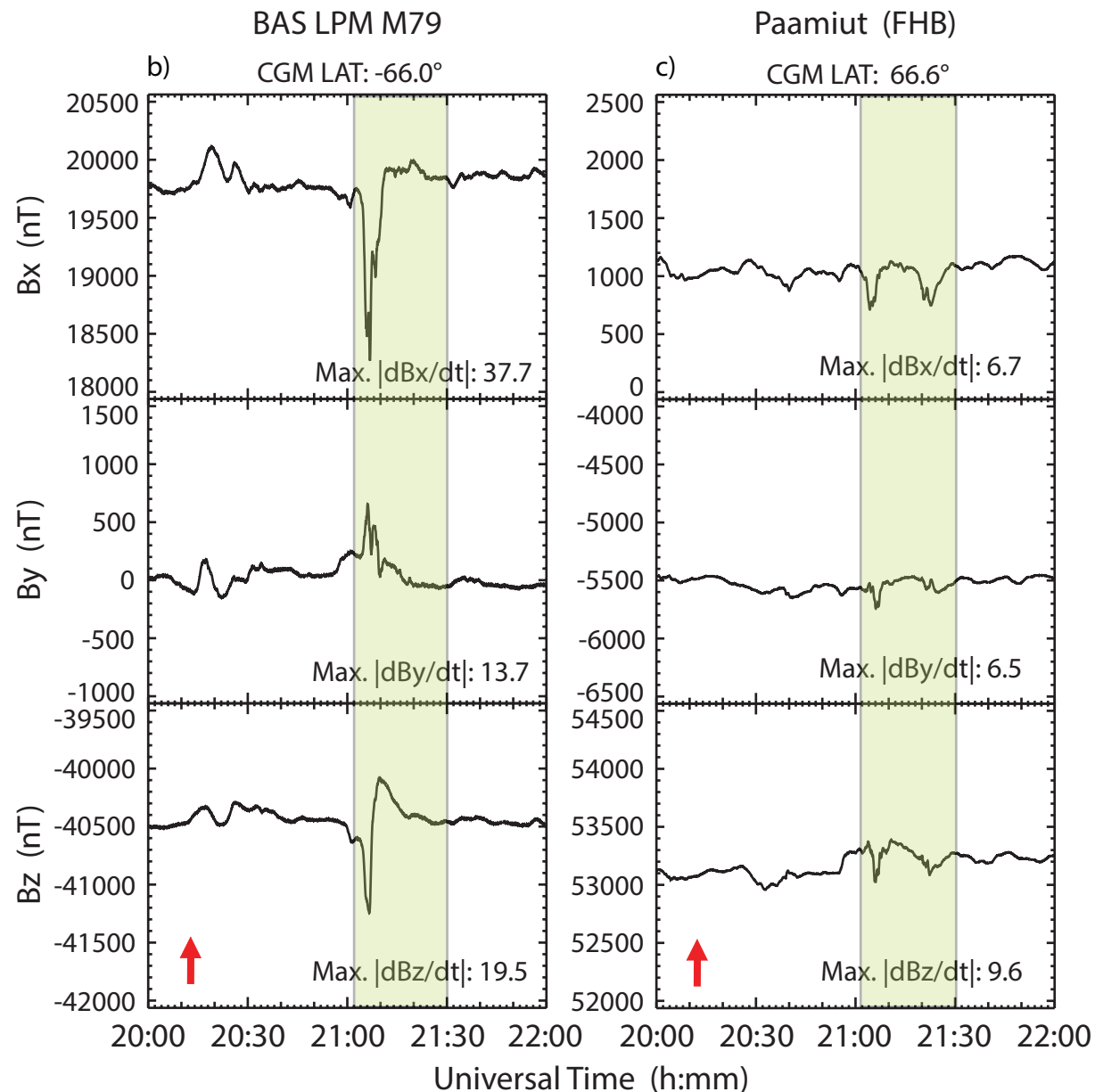
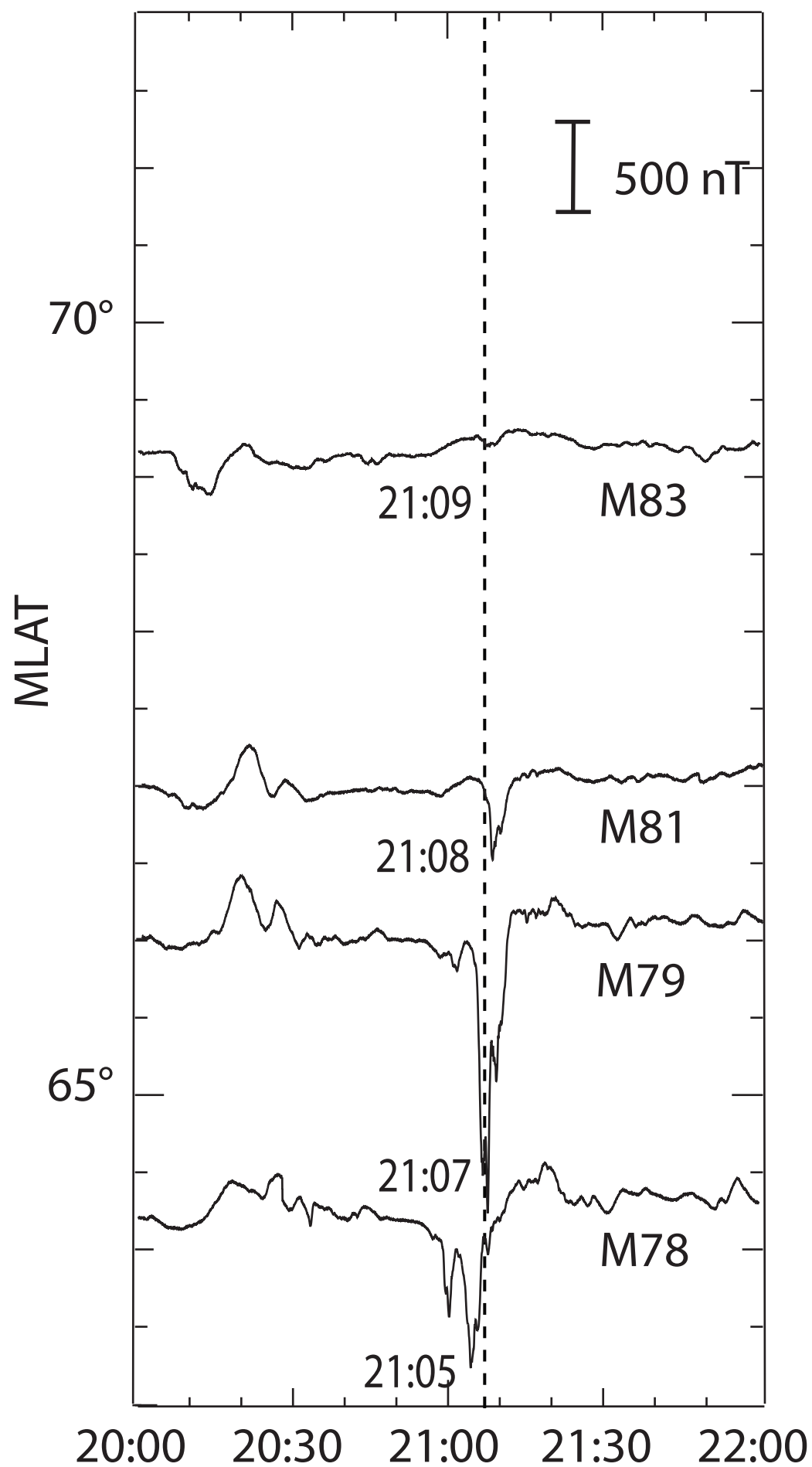


Figure 10.

Antarctica

MLT ~ 19.1 h

a)



Greenland

MLT ~ 19.1 h

b)

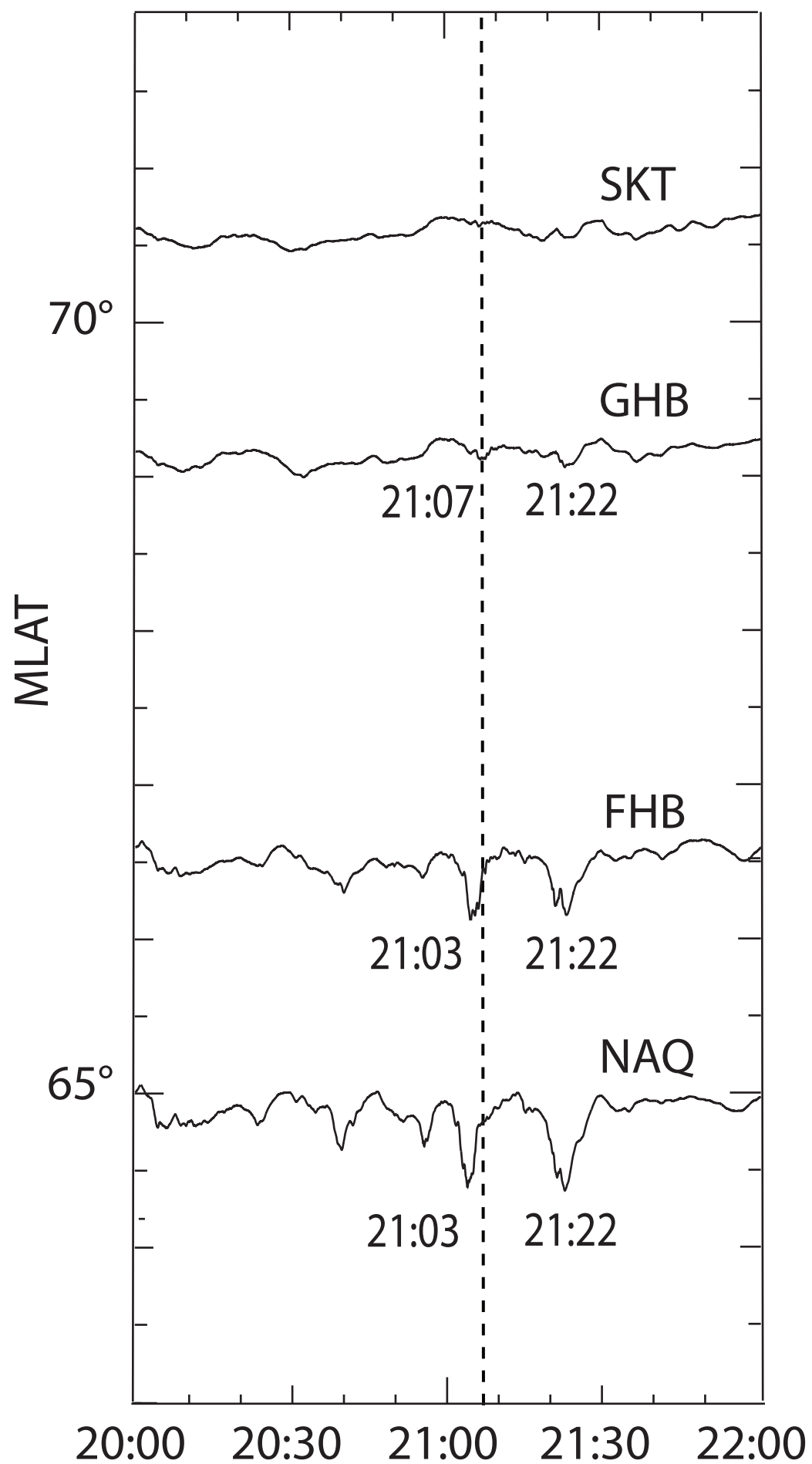


Figure 11.

May 8, 2016 16129 ~21:08 UT

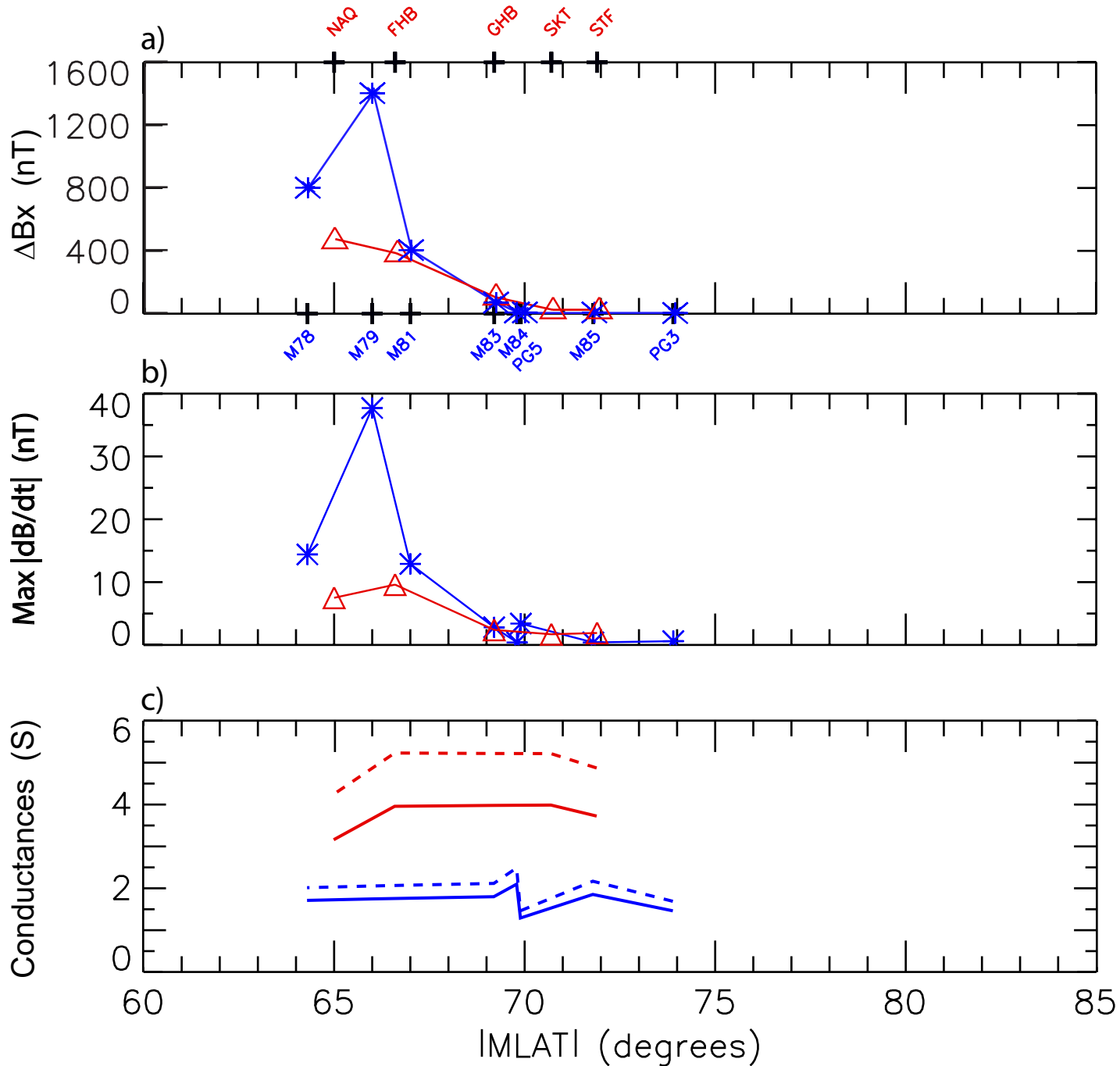


Figure 12.

OMNI data May 13, 2015

May 13, 2015 Yearday = 15133

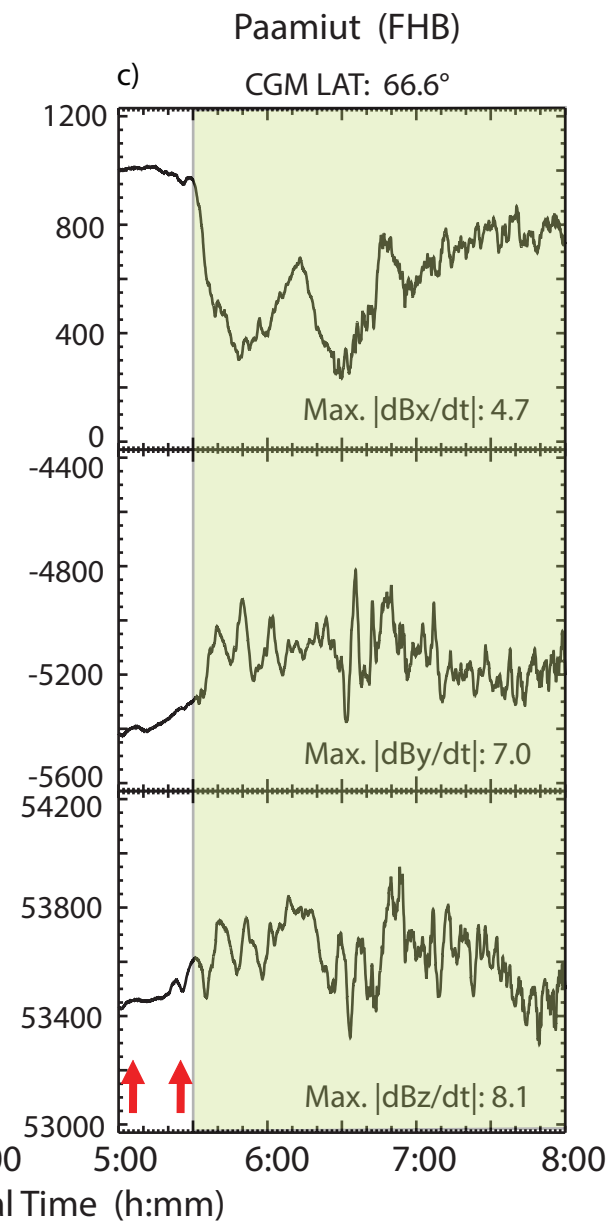
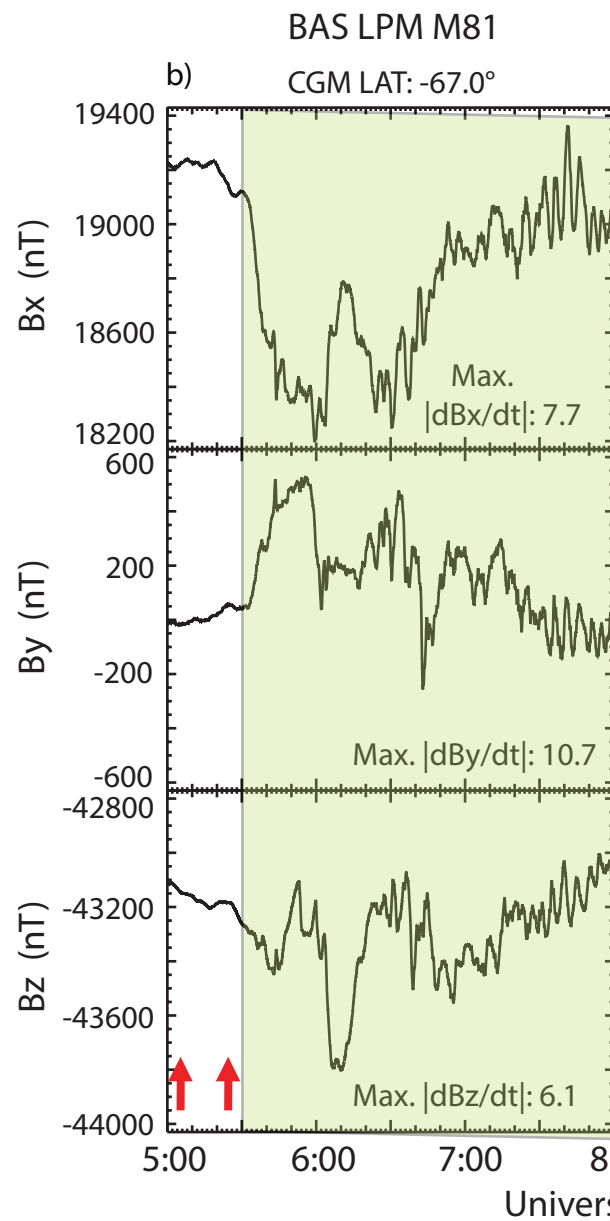
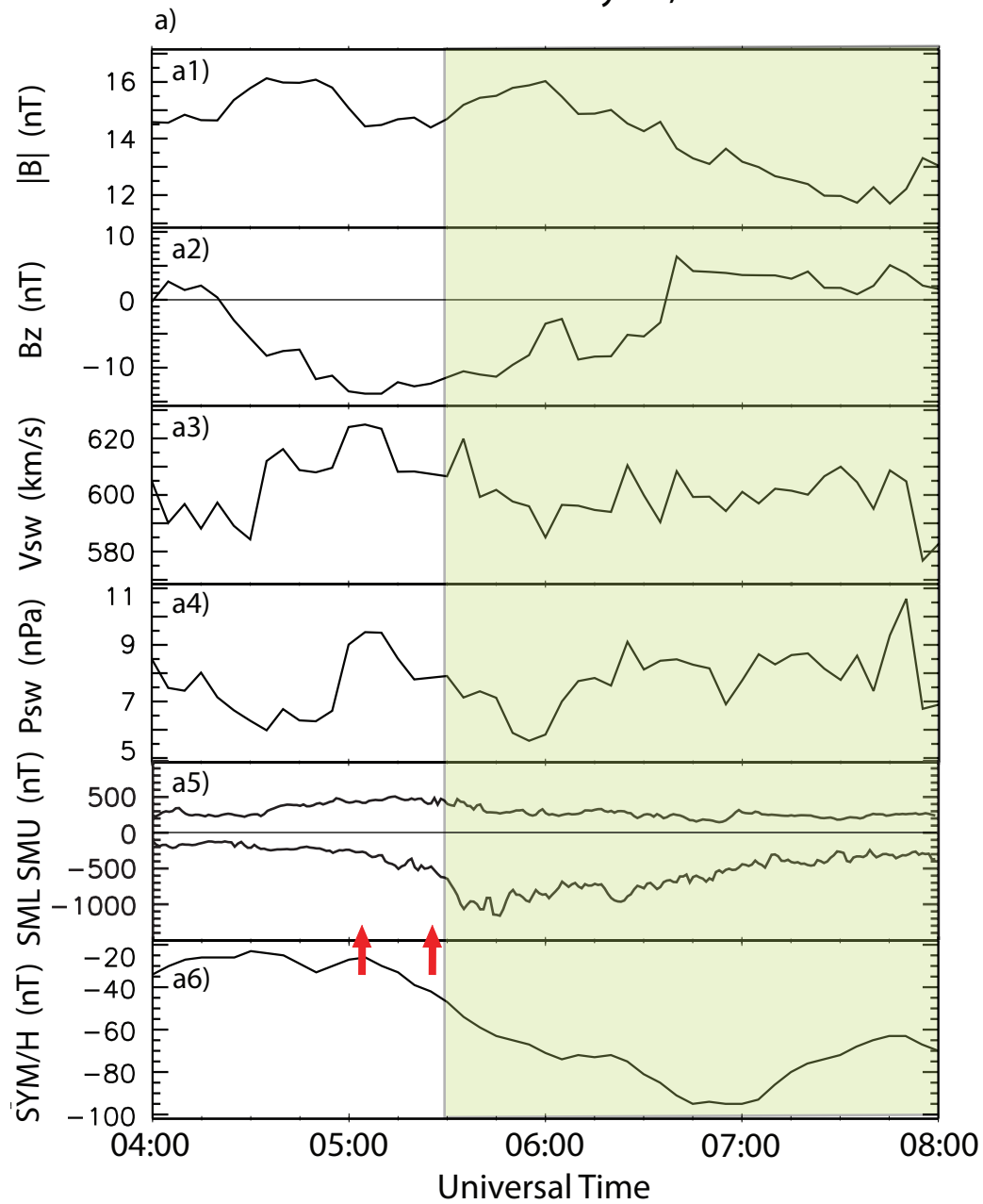
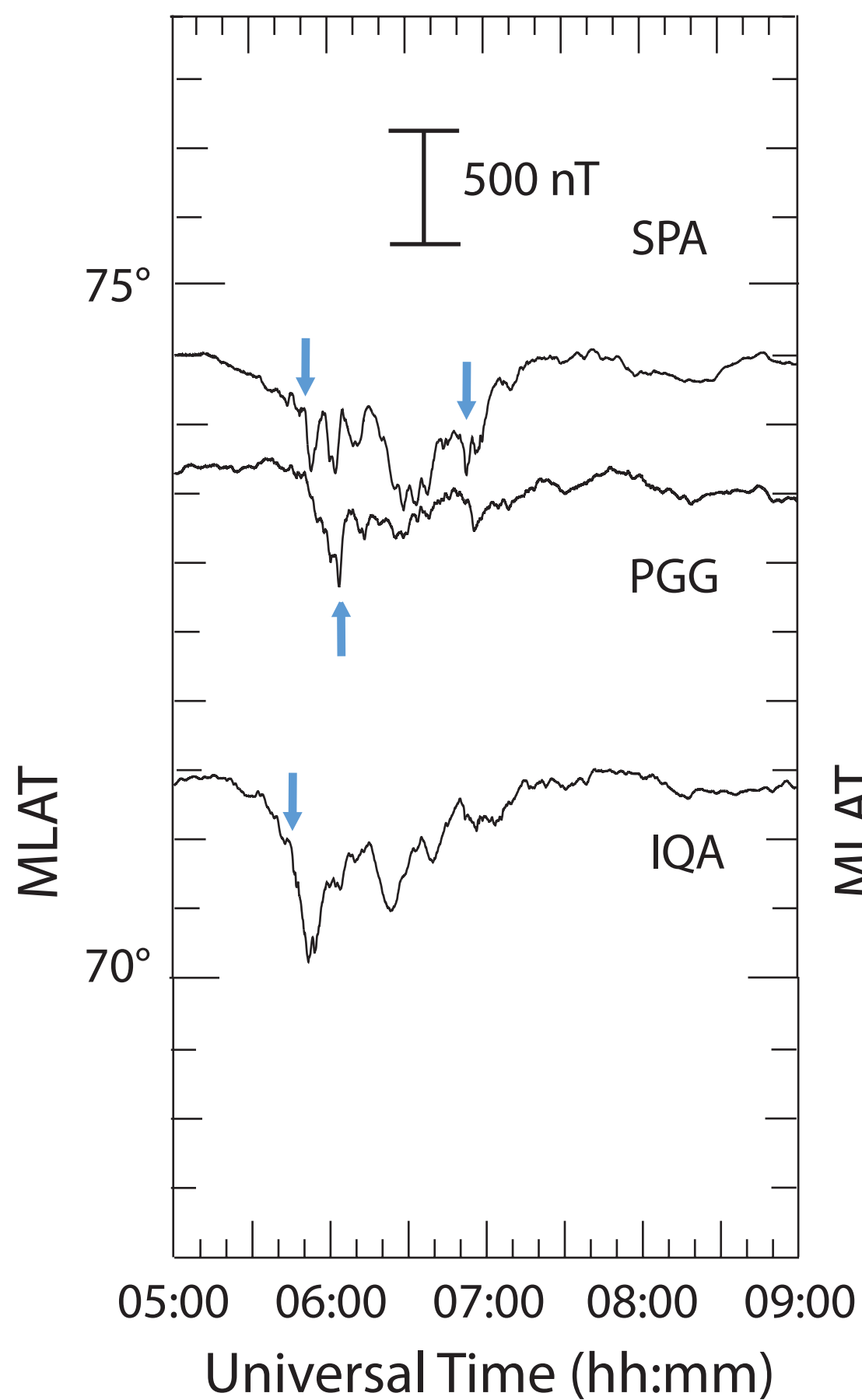


Figure 13.

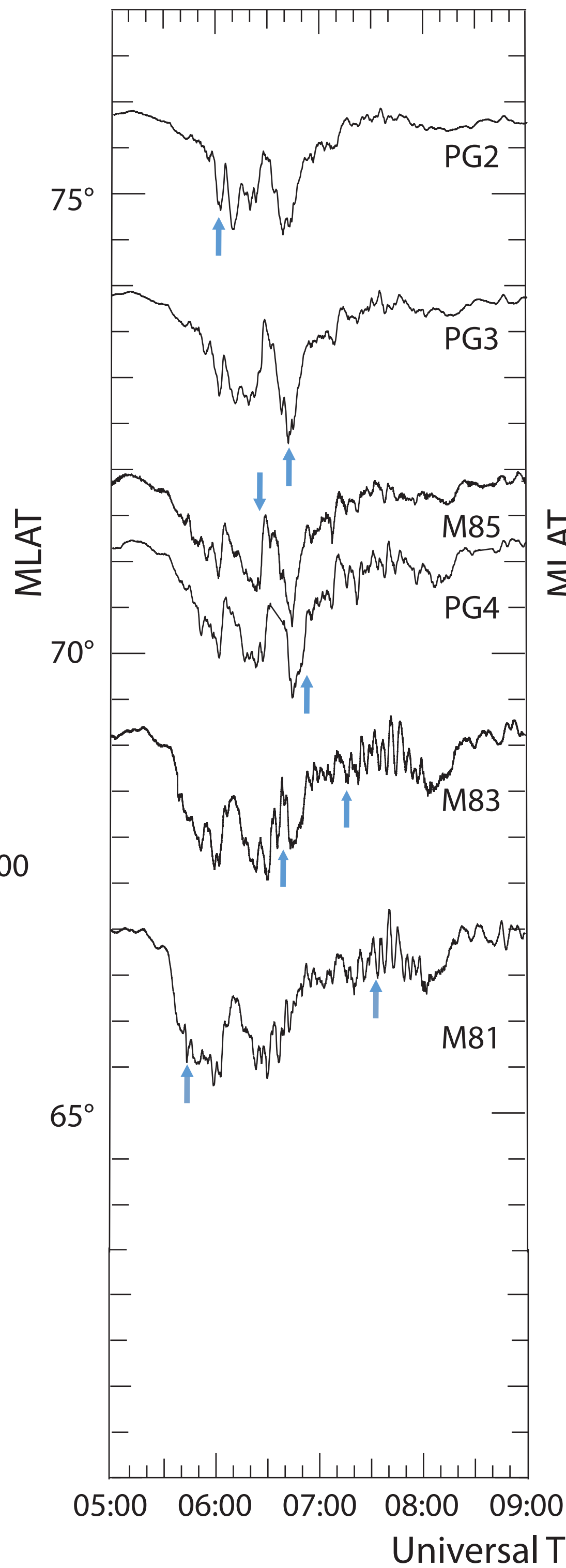
Canada / Antarctica

a) MLT ~ 3 h



Antarctica

b) MLT ~ 4.2 h



Greenland

c) MLT ~ 4.2 h

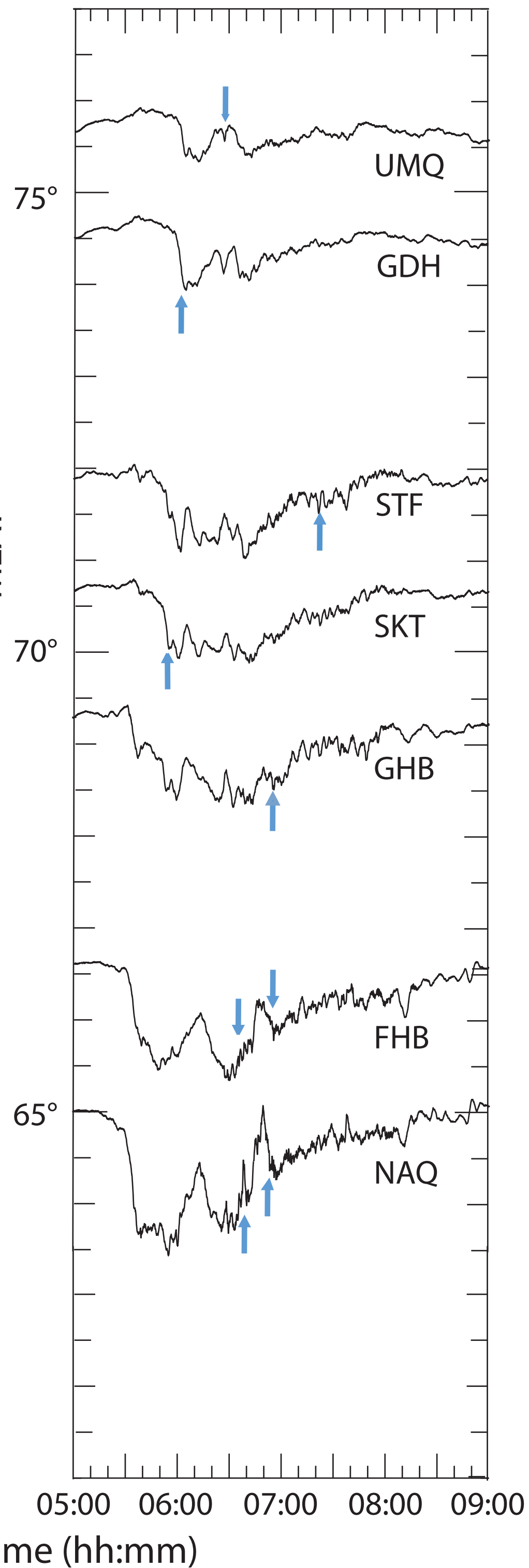


Figure 14.

May 13, 2015 15133 05:30 - 08:00 UT

